The Rational Design of Heterogeneous Photocatalysts for the Tandem Photocatalytic Hydrogen Evolution and Reduction of Organic Compounds in Water

by

Begümhan KARAPINAR KOÇ

A Dissertation Submitted to the

Graduate School of Sciences and Engineering

in Partial Fulfillment of the Requirements for

the Degree of

Doctor of Philosophy

in

Chemistry

KOÇ ÜNİVERSİTESİ

July 9, 2024

The Rational Design of Heterogeneous Photocatalysts for the Tandem Photocatalytic Hydrogen Evolution and Reduction of Organic Compounds in Water

Koç University

Graduate School of Sciences and Engineering

This is to certify that I have examined this copy of my doctoral dissertation by

Begümhan KARAPINAR KOÇ

and have found that it is complete and satisfactory in all respects,

and that any and all revisions required by the final

examining committee have been made.

Committee Members:

_____

Assoc. Prof. Önder METİN (Advisor)

_____

Assoc. Prof. Safacan KÖLEMEN

_____

Prof. Dr. Can ERKEY

_____

Prof. Dr. İmren HATAY PATIR

_____

Prof. Dr. Sermet KOYUNCU

Date: 09/07/2024

This thesis is dedicated to my family, who stood by me during my most challenging times. Mom, you have been my greatest source of inspiration.

Lumos Maxima

ABSTRACT

The Rational Design of Heterogeneous Photocatalysts for the Tandem Photocatalytic Hydrogen Evolution and Reduction of Organic Compounds in Water

Begümhan KARAPINAR KOÇ

Doctor of Philosophy in Chemistry, July 9, 2024

The rapid increase in the global population has spurred a concurrent rise in industrial activities and technological advancements, intensifying the demand for reliable energy resources. Currently, most of the global energy needs are met by fossil fuels. However, the extensive use of fossil fuels over the past century has significantly contributed to global warming, posing severe environmental and sustainability challenges. These challenges underscore the urgent need to transition toward renewable energy sources. Among the alternatives for meeting energy needs from renewable sources, the use of hydrogen as an energy carrier stands out because of its high energy density and environmentally benign nature, which emits zero greenhouse gases. One promising method for sustainable hydrogen production is photocatalytic water splitting, which harnesses the inexhaustible and free energy of the sun. This method has recently garnered considerable attention as a potential solution to the global energy crisis. In photocatalytic water splitting, semiconductor materials with an appropriate band gap facilitate the hydrogen evolution reactions (HER) under solar light irradiation. The efficiency of this process depends on the development of advanced semiconductor materials capable of optimizing the HER under solar illumination.

One of the advanced strategies to enhance the photocatalytic activity of semiconductor materials is the construction of their heterojunctions with other semiconductors or metals. Literature indicates that heterojunctions composed of semiconductor materials and noble metal nanoparticles (NPs) such as platinum (Pt), and palladium (Pd)achieve high efficiency in HER due to their unique electronic properties and the heterojunction (Schottky junction) formed between the semiconductor and conductor. To form efficient Schottky junctions, support material should be cost-effective, non-toxic, have a large surface area and proper band gap that can be activated by the large portion of solar light. Among the various candidates, red phosphorus (RP) and black phosphorus (BP), two stable allotropes of elemental phosphorus, have attracted significant attention due to their exceptional properties. These semiconductor materials have been increasingly used in photocatalytic HER applications. However, the photocatalytic activity of a single semiconductor is often limited by the accumulation behavior of charge carriers and inefficient solar light absorption. To address this limitation, the formation of heterostructures with these semiconductor materials has been shown to significantly enhance photocatalytic activity, providing a more efficient pathway for charge separation and transfer, thereby improving overall HER performance.

On the other hand, hydrogenation is an important chemical reaction in which unsaturated molecules are converted into saturated counterparts by addition of hydrogen (H_2) in the presence of a metal catalyst. This process plays a critical role in synthesizing

valuable compounds in organic chemistry, producing pharmaceuticals in the pharmaceutical industry, and refining processes in the petrochemical industry. Commonly referred to as conventional catalytic hydrogenation, hydrogenation reactions are predominantly conducted under severe conditions requiring the presence of external H_2 gas and elevated reaction temperatures. As a mild and safer alternative to this method, the transfer hydrogenation technique facilitates hydrogenation reactions without needing external H_2 gas. Instead, it employs hydrogen carriers such as isopropanol, formic acid, ammonia borane and sodium borohydride to provide the necessary hydrogen. The photocatalytic hydrogenation method allows hydrogenation reactions to be carried out under milder conditions and offers a more sustainable and environmentally friendly approach. Advancing a strategy by integrating photocatalytic HER with transfer hydrogenation methods can be achieved by selecting greener, non-toxic, and cost-effective hydrogen sources. In this context, the utilization of hydrogen generated photocatalytically from water in hydrogenation reactions presents a highly influential approach, potentially yielding impactful outcomes in the field of organic chemistry.

In this thesis, the initial section details the synthesis of RP-BP/Pt-PtP_2 heterojunctions using a wet-chemical synthesis method from red phosphorus (RP) with an appropriate solvent and a platinum precursor. This unique protocol simultaneously generates BP nanosheets from RP under mild conditions and in-situ produces Pt and PtP_2 NPs for the first time. The RP-BP/Pt-PtP_2 heterojunctions were first tested as photocatalysts for the hydrogen evolution reaction (HER) using triethanolamine (TEOA) as a hole scavenger and Eosin Y as a photosensitizer under visible light irradiation, achieving a high HER activity of 47.46 mmol $H_2.g^{-1}$ catalyst in 8 hours, which is 40 and 16 times higher than pristine RP and BP, respectively. Encouraged by these results, a tandem photocatalytic HER and hydrogenation of nitroarenes were designed using RP-BP/Pt-PtP_2 heterojunctions as photocatalysts, with water as the hydrogen donor under visible light irradiation. This one-pot RP-BP/Pt-PtP_2 catalyzed process exhibited high selectivity in reducing nitrobenzene derivatives to their corresponding azoxy compounds, with conversion reaching up to 99%. Deuterium labeling experiments confirmed that water served as the hydrogen generator.

In the subsequent section, Pt NPs were synthesized in situ on RP via the chemical reduction method, resulting in an easy and effective method to obtain the RP/Pt heterojunction photocatalysts. Delightfully, RP/Pt catalysts outperformed the RP/BP-Pt-PtP_2 , demonstrating a photocatalytic HER activity of 70.57 mmol $H_2.g^{-1}$ in 8 hours. The activity of the RP/Pt in the tandem photocatalytic HER and transfer hydrogenation of nitroarene compounds was also investigated. Additionally, Pd metal is known for its hydrogenation efficiency, were synthesized in situ on RP. The performance of RP/Pt and RP/Pd catalysts in photocatalytic HER and the reduction of nitroarene compounds were compared. Due to the varying electronic properties of the metals, notable results were obtained that emphasize their distinct impacts on the reaction outcomes. While RP/Pt was identified as the catalyst with the highest photocatalytic HER activity, the RP/Pd catalyst exhibited superior activity in photocatalytic hydrogenation of nitrobenzene compounds. The conversion and selectivity of products formed were determined by using GC-MS and NMR. The structural, chemical, and optical properties of as-synthesized materials were elucidated using various advanced characterization techniques, including TEM, HR-TEM, XPS, XRD, UV-Vis, PL, TRPL, and EIS.

ÖZETÇE

Suda Tandem Fotokatalitik Hidrojen Üretimi ve Organik Bileşiklerin İndirgenmesi için Heterojen Fotokatalizörlerin Rasyonel Tasarımı

Begümhan KARAPINAR KOÇ

Kimya, Doktora

9 Temmuz 2024

Küresel nüfustaki hızlı artış, endüstriyel faaliyetlerde ve teknolojik ilerlemelerde eşzamanlı bir artışa yol açarak güvenilir enerji kaynaklarına olan talebi yoğunlaştırmıştır. Günümüzde küresel enerji ihtiyacının büyük bir kısmı fosil yakıtlar tarafından karşılanmaktadır. Bununla birlikte, fosil yakıtların geçtiğimiz yüzyıl boyunca yoğun kullanımı, küresel ısınmaya önemli ölçüde katkıda bulunarak ciddi çevresel ve sürdürülebilirlik sorunları yaratmaktadır. Bu sorunlar, yenilenebilir enerji kaynaklarına geçişin aciliyetini vurgulamaktadır. Enerji ihtiyacının yenilenebilir kaynaklardan karşılanmasına yönelik alternatifler arasında, bir enerji taşıyıcısı olarak hidrojen, yüksek enerji yoğunluğu ve sıfır sera gazı yayan çevreye zararsız yapısı nedeniyle öne çıkmaktadır. Sürdürülebilir hidrojen üretimi için umut vaat eden yöntemlerden biri, güneşin tükenmez ve ücretsiz olarak elde edilebilen enerjisinden yararlanan fotokatalitik su ayrışması yöntemidir. Bu yöntem, son zamanlarda küresel enerji krizine potansiyel bir çözüm olarak önemli ölçüde ilgi görmektedir. Fotokatalitik su ayrışmasında, uygun bant aralığına sahip yarı iletken malzemeler hidrojen üretim reaksiyonlarını (HER) kolaylaştırır. Bu sürecin verimliliği, güneş ışığı altında HER'yi optimize edebilen gelişmiş yarı iletken malzemelerin geliştirilmesine bağlıdır.

Yarı iletken malzemelerin fotokatalitik aktivitesini artırmak için ileri stratejilerden biri heteroeklem yapılı fotokatalizörlerin geliştirilmesidir. Literatür, platin (Pt) ve paladyum (Pd) gibi asil metaller tarafından desteklenen yarı iletken malzemelerden oluşan heteroyapıların, bu metal nanoparçacıkların benzersiz elektronik özellikleri nedeniyle HER'de yüksek verimlilik elde ettiğini göstermektedir. İdeal bir destek malzemesi uygun maliyetli olmalı, toksik olmamalı, geniş bir yüzey alanına sahip olmalı ve geniş ışık emme özellikleri sergilemelidir. Çeşitli adaylar arasında, her ikisi de elementel fosforun allotropları olan kırmızı fosfor ve siyah fosfor, olağanüstü özellikleri nedeniyle büyük ilgi görmüştür. Bu yarı iletken malzemeler fotokatalitik HER uygulamalarında giderek daha fazla kullanılmaktadır. Bununla birlikte, tek bir yarı iletkenin fotokatalitik aktivitesi genellikle yük taşıyıcılarının birikme davranışı nedeniyle sınırlıdır. Bu sınırlamayı aşmak için, bu yarı iletken malzemelerle heteroeklem yapıların oluşturulması, fotokatalitik aktiviteyi önemli ölçüde artırarak, yük ayrılması ve transferi için daha verimli bir yol sağlayarak genel HER performansını iyileştirmektedir.

Öte yandan hidrojenasyon, doymamış moleküllerin bir metal katalizör varlığında hidrojen (H_2) eklenerek doymuş moleküllere dönüştürüldüğü önemli bir kimyasal reaksiyondur. Bu süreç, organik kimyada değerli bileşiklerin sentezlenmesinde, ilaç endüstrisinde farmasötiklerin üretilmesinde ve petrokimya endüstrisinde arıtma işlemlerinde kritik bir rol oynar. Genellikle geleneksel katalitik hidrojenasyon olarak

adlandırılan hidrojenasyon reaksiyonları, ağırlıklı olarak harici H_2 gazının ve yüksek reaksiyon sıcaklıklarının varlığını gerektiren zorlu koşullar altında gerçekleştirilir. Bu yönteme daha yumuşak ve güvenli bir alternatif olarak transfer hidrojenasyon tekniği, harici H_2 gazına ihtiyaç duymadan hidrojenasyon reaksiyonlarını kolaylaştırır. Bunun yerine, gerekli hidrojeni sağlamak için izopropanol, formik asit, amonyak boran ve sodyum borohidrit gibi hidrojen taşıyıcıları kullanır. Fotokatalitik hidrojenasyon yöntemi, hidrojenasyon reaksiyonlarının daha ılıman koşullar altında gerçekleştirilmesini sağlar ve daha sürdürülebilir ve çevre dostu bir yaklaşım sunar. Fotokatalitik HER ile transfer hidrojenasyon yöntemlerini bir araya getirerek bütünleşik bir strateji geliştirmek, daha çevreci, zehirli olmayan ve uygun maliyetli hidrojen kaynaklarının seçimi ile gerçekleştirilebilir. Bu bağlamda, hidrojenasyon reaksiyonlarında fotokatalitik olarak sudan elde edilen hidrojenin kullanımı, organik kimya alanında etkileyici sonuçlar doğurma potansiyeline sahip son derece etkili bir yaklaşım sunmaktadır.

Bu tezin ilk bölümünde, uygun bir çözücü ve platin kaynağı ile kırmızı fosfor (RP) kullanılarak ıslak-kimyasal sentez yöntemi ile RP-BP/Pt-PtP_2 heteroyapılarının sentezi ayrıntılı olarak açıklanmaktadır. Bu özgün protokol ile aynı anda hafif koşullar altında hem RP'den BP nanoyaprakları üretilirken, hem de Pt ve PtP2 nanopartiküllerin yerinde üretimi gerçekleştirildi. RP-BP/Pt-PtP_2 heteroeklem yapılı fotokatalizörler ilk olarak görünür ışık aydınlatması altında HER için bir fotokatalizör olarak test edildi ve kurban ajan olarak trietanolamin (TEOA) ve ışığa duyarlılaştırıcı olarak Eosin Y kullanılarak 8 saatte 47,46 mmol $H_2.g^{-1}$ olarak yüksek bir HER aktivitesi elde edildi, bu değer saf RP ve BP'ye göre sırasıyla 40 ve 16 kat daha yüksektir. Bu olumlu sonuçlardan cesaret alarak, görünür ışık ışınlaması altında hidrojen kaynağı olarak su ile fotokatalizör olarak RP-BP/Pt-PtP2 heteroyapısı kullanılarak tandem fotokatalitik HER ve nitrobenzen bileşiklerinin hidrojenasyonu tasarlandı. Bu tek kapta RP-BP/Pt-PtP_2 katalizörlü süreç, nitrobenzen türevlerinin karşılık gelen azoksi bileşiklerine yüksek seçicilikle indirgenmesini sağladı ve dönüşüm oranı %99'a kadar ulaştı. Öte yandan gerçekleştirilen döteryum etiketleme deneyleri, hidrojen kaynağının su olduğunu doğruladı. Bu tek-kap RP-BP/Pt-PtP_2 katalizli proses, nitrobenzen türevlerini karşılık gelen azoksi bileşiklerine indirgemede yüksek seçicilik sergiledi ve dönüşüm %99'a kadar ulaştı.

Sonraki bölümde, Pt nanopartikülleri RP üzerinde yerinde sentezlenerek RP/Pt katalizörü elde etmek için kolay ve etkili bir yöntem elde edildi. Memnuniyet verici şekilde, RP/Pt katalizörü 8 saat içinde 70.57 mmol $H_2.g^{-1}$ fotokatalitik HER aktivitesi göstererek RP/BP-Pt-PtP_2'yi geride bıraktı. RP/Pt'nin tandem fotokatalitik HER ve nitroaren bileşiklerinin transfer hidrojenasyonundaki aktivitesi de araştırıldı. Ek olarak, hidrojenasyon reaksiyonlarındaki üstün performansları ile bilinen metal olan Pd RP üzerinde yerinde sentezlendi. RP/Pt ve RP/Pd ve katalizörlerinin fotokatalitik HER ve nitroaren bileşiklerinin indirgenmesindeki performansları karşılaştırıldı. Metallerin değişen elektronik özellikleri nedeniyle, reaksiyon sonuçları üzerindeki farklı etkilerini vurgulayan dikkate değer sonuçlar elde edildi. RP/Pt en yüksek fotokatalitik HER aktivitesine sahip katalizör olarak belirlenirken, RP/Pd katalizörü nitrobenzen bileşiklerinin fotokatalitik hidrojenasyonunda en yüksek aktiviteyi sergiledi. Oluşan anilin ürünlerinin dönüşüm ve seçicilik verileri GC-MS ve NMR kullanılarak elde edildi. Sentezlenen fotokatalizörlerin yapısal, kimyasal ve optik özellikleri TEM, HR-TEM, XPS, XRD, UV-Vis, PL, TRPL ve EIS gibi çeşitli ileri karakterizasyon teknikleri kullanılarak aydınlatıldı.

ACKNOWLEDGEMENTS

I would like to express my deepest gratitude to my advisor Assoc. Prof. Önder Metin for his unwavering support and motivation throughout my doctoral studies. He was always accessible whenever I encountered a problem or needed assistance, and I am incredibly thankful for his patience in tirelessly reviewing and correcting everything multiple times. During my low morale and motivation moments, his long and encouraging conversations always lifted my spirits. I am profoundly grateful to him for believing in me, continuously motivating me, and pushing me to aim higher. His confidence in me showed me what I can achieve when I trust myself.

I would like to thank my thesis committee members, Prof. Dr. Can ERKEY, Assoc. Prof. Safacan KÖLEMEN, Prof. Dr. İmren HATAY PATIR, and Prof. Dr. Sermet KOYUNCU, for their valuable time, insights, and knowledge, which greatly contributed to the completion of this doctoral thesis.

I would like to thank Assoc. Prof. Safacan KÖLEMEN for our scientific discussions regarding the organic studies. I also thank Prof. Dr. İmren HATAY PATIR for her support and knowledge for completing this thesis and our ongoing research projects.

I would like to thank Dr. Gizem YILDIZ from Konya Selçuk University for her contributions and support related to HER studies. I also extend my gratitude to Vladimir Efremov for his support during the theoretical studies, Ecem Ezgi ÖZKAHRAMAN for her assistance with electrochemical measurements, and Buse SÜNDÜ for her help with TEM measurements.

Since 2019, I have had the opportunity to meet many people as a member of the Metin Research Group (MRG). I would like to extend my thanks to both past and present members of MRG. We laughed and had fun together at group events. We all learned something from each other and shared many experiences. My sincere thanks goes to Dr. Sibel EKEN KORKUT, who provided me with the greatest moral support during this time. Your endless motivational talks were invaluable to me. I truly do not know what mental state I would be in without your support. Thank you very much for everything. I would like to thank Dr. Natarajan PALANİ for dedicating his time to scientific discussions related to my thesis. I extend my gratitude to Dr. Mücahit ÖZDEMİR from

Marmara University, for his patience and constant support.

I would like to thank Scientific and Technological Research Council of Turkey (TUBITAK) for providing me scholarship in the context of the 2211-A Domestic General Ph.D. Scholarship Program.

Finally, I would like to thank my spouse. We were apart during my doctoral studies, and I am grateful for his sacrifices, constant support, and being there for me through everything. To my family; your contribution in completing this process is immense. I might not have found the strength to finish without your support. Thank you for always being by my side in every circumstance.

TABLE OF CONTENTS

LIST OF TABLES

LIST OF FIGURES

ABBREVIATIONS

VB	:	Valence Band
CB	:	Conduction Band
HER	:	Hydrogen Evolution Reaction
OER	:	Oxygen Evolution Reaction
RHE	:	Reversible Hydrogen Electrode
V	:	Voltage
eV	:	Electron volt
ΔG	:	Gibbs free energy
EY	:	Eosin Y
HOMO	:	Highest Occupied Molecular Orbital
LUMO	:	Lowest Unoccupied Molecular Orbital
TEOA	:	Triethanolamine
2D	:	Two-dimentional
NPs	:	Nanoparticles
Pt NPs	:	Platinum Nanoparticles
Pd NPs	:	Palladium Nanoparticles
ΔG_H	:	Hydrogen Adsorption Energy
BP	:	Black Phosphorus
RP	:	Red Phosphorus
φ_s	:	Work Function of XPS
AB	:	Ammonia Borane
$NaBH_4$	:	Sodium Borohydride
EDA	:	Ethylenediamine
H_{ads}	:	Adsorbed Hydrogen Species

AOB	:	Azoxybenzene
AZB	:	Azobenzene
HAB	:	Hydrazobenzene
NSB	:	Nitrosobenzene
PHA	:	Phenylhydroxylamine
NB	:	Nitrobenzene
TEMPO	:	(2,2,6,6-Tetramethylpiperidin-1-yl)oxyl
BQ	:	1,4-benzoquinone
D_2O	:	Deuterium Oxide
NHE	:	Normal Hydrogen Electrode
NMR	:	Nuclear Magnetic Resonance
GC-MS	:	Gas-Chromatography-Mass Spectroscopy
XRD	:	X-ray Diffraction
PL	:	Photoluminescence
TRPL	:	Time-resolved Photoluminescence Spectroscopy
UV-Vis-DRS	:	Ultraviolet-Visible-Diffuse Reflectance Spectroscopy
TEM	:	Transmission Electron Microscope
SEM	:	Scanning Electron Microscopy
HR-TEM	:	High-resolution Transmission Electron Microscopy
XPS	:	X-ray Photoelectron Spectroscopy
BE	:	Binding Energy
$h\nu$	:	Photon Energy
α	:	Absorption Coefficient
E_g	:	Bandgap
ICP-MS	:	Inductively Coupled Plasma Mass Spectroscopy

E_{fb}	:	Flat Band Potential
PtP_2	:	Platinum Phosphide
IFFT	:	Inverse-Fast-Fourier-Transform
HAADF	:	High-Angle Annular Dark Field
HR-XPS	:	High Resolution X-Ray Photoelectron Spectroscopy
E_{fl}	:	Fermi level
Fcc	:	Face-centered cubic

Chapter 1:

INTRODUCTION

Yes my friends, I believe that water will one day be employed as fuel, that hydrogen and oxygen which constitute it, used singly or together, will furnish an inexhaustible source of heat and light, of an intensity of which coal is not capable…. When the deposits of coal are exhausted, we shall heat and warm ourselves with water. Water will be the coal of the future.

Jules Verne, The Mysterious Island (1874-5)

1.1. Motivation : Unlocking The Potential of Renewable Energy for Sustainable Growth

The most significant advancements in human history have been recorded in the past two centuries, coinciding with a rapidly increasing world population. This period has witnessed growing economies, remarkable advances in the industrial sector, an insatiable curiosity to explore both space and the depths of the oceans, progress in medicine, groundbreaking technological developments, and many more. All these strides have relied on one essential element: energy. Coal was used as an energy source to power the engines of machines, driving to the Industrial Revolution, which brought about tremendous progress in various fields such as agriculture, livestock farming, and transportation. During this period, the world population continued to grow rapidly. The increasing energy demand of the expanding population has accelerated the transition from coal to liquid fossil fuels.

Today, fossil fuels still meet a significant portion of the energy demand. However, concerns about the sustainability and safety of this energy source have arisen not only because of the limited lifespan of fossil fuel resources but also because of the extensive environmental damage they inflict. Petroleum constitutes one-third of the world's energy demand, and 95% of the transportation sector relies on petroleum for energy needs.[1] Shafiee et al. have indicated in their studies that petroleum resources are expected to

deplete sooner than natural gas and coal.[2] The environmental damage caused by fossil fuels is also considerable. The combustion of fossil fuels results in the emission of several greenhouse gases, primarily carbon dioxide (CO_2), methane (CH_4) and nitrous oxide (N_2O), and a variety of fluorinated gases such as hydrofluorocarbons and chlorofluorocarbons. These greenhouse gases accumulate in the atmosphere, trapping heat and significantly contributing to global warming. Since the Industrial Revolution, the concentration of CO_2 in the atmosphere has increased from 280 ppm to 450 ppm, and the Earth's surface has warmed by 0.76 °C, particularly in the last 30 years [3]. The increased concentration of greenhouse gases disrupts the natural balance of the Earth's climate system, resulting in adverse environmental effects such as the endangerment of ecosystems and habitats, melting polar ice, rising sea levels, and more frequent and severe weather events. On the other hand, oil extraction and transportation cause oil spills that persist in ecosystems for several years and have a negative impact on biodiversity. A striking example of this is the Deepwater Horizon oil spill that occurred off the coast of the Gulf of Mexico in 2010, which is widely considered one of the most significant environmental disasters in history [4]. As awareness of the environmental impact of current energy sources increased, the transition to renewable energy sources took place. With this increasing awareness, some have turned to nuclear power. Nuclear plants, because of their low carbon emissions, have become attractive to those concerned with increasing CO_2 levels. However, the use of uranium in reactors causes reactor accidents and generates radioactive residues [5]. These residues persist in water and soil for centuries, posing long-term ecological and health problems. The Chernobyl and Fukushima nuclear disasters are the most prominent examples of these disasters, which have affected millions of lives. These disasters not only cause immediate consequences but also have lasting effects. The consequences of these disasters underscore the importance of sustainable and safe energy sources.

In view of these challenges, the transition to cleaner, safer and more resilient renewable energy sources is an important step toward a future without devastating temperature increases or toxic environmental crises. Today, a substantial portion of the

energy demand is satisfied by renewable sources, which makes a significant contribution to sustainable economies. Among these, wind, geothermal, and solar energy are particularly noteworthy due to their potential to provide clean and virtually inexhaustible energy. Wind energy harnesses the power of wind currents, geothermal energy exploits the heat from the Earth's interior, and solar energy captures sunlight. These sources are celebrated for their ability to reduce greenhouse gas emissions. Nevertheless, these methods face limitations due to geographical, technological or intermittent availability constraints, which prevent their full exploitation. This seasonal dependency can limit its effectiveness in regions with less sunlight during certain seasons. Similarly, wind energy faces constraints due to variability in wind patterns, which can be unpredictable and intermittent. These limitations highlight the need for advancements in energy storage and distribution technology to ensure a consistent and reliable supply of renewable energy.

1.2. Hydrogen Energy as a Solution

Considering all these promising features and limiting factors of traditional renewable energy sources, transitioning to renewable hydrogen energy emerges as a significant step for extending the sustainability of existing energy systems. Hydrogen, as the simplest and most abundant element in nature, boasts an energy density of 140 MJ/kg—approximately three times that of oil and 4.5 times that of coal [6]. When burned, hydrogen produces H_2O, not emit any harmful greenhouse gases. In view of increasing concerns about energy sustainability, the zero carbon emission characteristics of hydrogen make it a reliable and prominent energy source for the future. Hydrogen has found diverse applications across various sectors, serving as a versatile resource. Some notable applications of hydrogen : include industrial and residential heating, transportation fuel, chemical synthesis through hydrogenation reactions, energy storage, ammonia production. NASA has been using liquid hydrogen as rocket fuel in spacecraft since the 1950s, owing to its high energy content per unit mass [7]. In the transportation sector, various automotive companies have developed new technologies for using hydrogen fuel, offering an environmentally friendly solution with zero CO_2 emission compared to traditional petroleum. In 2014, Toyota introduced the Mirai hydrogen fuel cell vehicle. These vehicles generate

electricity through hydrogen, oxygen, and a catalyst in their batteries, producing only water vapor as waste [8].

Hydrogen production methods include various approaches, whether sourced from fossil fuels or renewable energy sources. Today, hydrogen is predominantly derived from fossil fuel-based methods. Currently, large-scale production of hydrogen gas is achieved through the Steam Methane Reforming (SMR) method (**Eq 1.1**). In this process, methane undergoes a reaction with steam at high temperatures, which is facilitated by a catalyst, generating hydrogen gas and carbon monoxide gas. Subsequently, the Water Gas Shift (WGS) reaction (**Eq 1.2**) involves the reaction of carbon monoxide and steam in the presence of a catalyst, producing hydrogen gas and carbon dioxide (CO_2)[9] Fossil fuel-based techniques are generally more cost-effective than renewable energy sources. Nevertheless, a drawback of these methods is the generation of greenhouse gases during hydrogen production, which contradicts the principles of "green hydrogen" emphasized thus far.

Steam-methane reforming reaction:

$$CH_4 + H_2O \rightarrow CO + 3H_2 \quad (1.1)$$

Water-gas shift reaction :

$$CO + H_2O \rightarrow CO_2 + H_2 \quad (1.2)$$

One method for producing hydrogen from renewable energy sources is hydrogen production from biomass processes. This technique uses organic materials such as plant and animal wastes for. The biomass process to produce renewable hydrogen has been limited in efficiency due to various factors. The continued demand for raw materials, potential greenhouse gas emissions in specific processes using fossil fuels and fluctuating raw material prices are among the parameters that limit its effectiveness. Another method used for hydrogen production from renewable energy sources is water splitting. Water splitting can be performed in two steps: electrocatalytic and photocatalytic water splitting processes. Electrocatalytic water splitting involves splitting water into hydrogen and

oxygen using an electric current. When the electric current required for this process is obtained from renewable energy sources such as wind, hydroelectric, or solar energy, it becomes a sustainable and clean energy source. Although electrocatalytic water splitting represents an important step in hydrogen production from renewable energy sources, harnessing solar energy as an electricity source can further increase the sustainability and efficiency of hydrogen production. In this regard, employing solar power as an infinite energy source to produce hydrogen from water containing the most fundamental, clean, and carbon-free hydrogen content will provide an innovative, reliable, and promising solution to future energy needs.

1.3. Photocatalytic Hydrogen Evolution Reaction (HER)

The use of renewable solar energy for hydrogen generation from water (HER) presents a captivating approach, highlighting its appeal as a method that relies on an endless energy source and offers a clean and sustainable hydrogen production and storage solution. This method not only symbolizes the transition to sustainable energy but also represents an innovative approach that uses sunlight to reveal hydrogen potential in water. The photocatalytic HER can be realized in the presence of homogeneous metal complexes and/or heterogeneous semiconductor materials with suitable HOMO/LUMO and/or band gaps, respectively. Due to the drawbacks of utilizing homogeneous metal complexes as photocatalysts in the photocatalytic HER, the use of heterogeneous semiconducting materials has attracted considerable attention. The mechanism for the photocatalytic HER over heterogeneous semiconductors involves three main steps (**Figure 1.1**). Firstly, the semiconductor material is excited by a light source emitting photon with an energy equal or greater than the semiconductor's band gap. As a result of the excitation, electrons from the valence band (VB) of the semiconductor are transferred to the conduction band (CB) and created holes in the valence band (VB). Subsequently, the generated electrons and holes migrate to the semiconductor surface, and electrons sequentially reduce H^+ species to H_2 in the conduction band, leading to HER, while holes in the valence band oxidize water to produce oxygen in the oxygen evolution reaction (OER), which the mentioned reactions were given in **Eq 1.3-1.5**.

Water Oxidation (Oxygen Evolution Reaction (OER):

$$2H_2O \rightarrow O_2 + 4H^+ + 4e^- \; E_0 = 1.23\; eV \tag{1.3}$$

Water Reduction (Hydrogen Evolution Reaction (HER)):

$$2H^+ + 2e^- \rightarrow H_2 \; E_0 \; = 0\; eV \tag{1.4}$$

Overall:

$$2H_2O \rightarrow O_2 + 2H_2 \; E_0 = 1.23\; eV \text{ [10]} \tag{1.5}$$

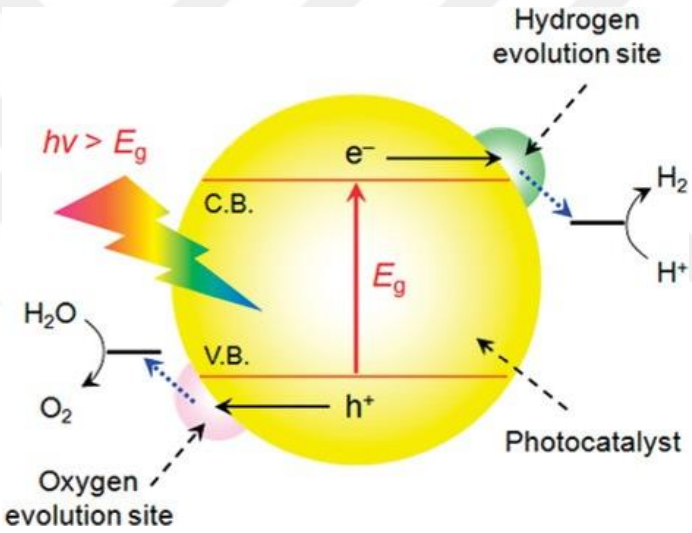

Figure 1.1. Photocatalytic water splitting scheme. [11]

Thermodynamically, for a semiconductor material to perform photocatalytic water splitting, the CB level should be equal to or lower than the proton reduction potential of O V vs. RHE, and the VB potential should be greater than the oxidation potential of water, which is 1.23 V vs. RHE. A semiconductor material must have a minimum band gap of 1.23 eV to enable water-splitting. It is noteworthy that a significant portion of sunlight (~45%) comprises visible light. For a semiconductor material to effectively absorb visible light, its band gap should ideally be below 3.0 eV. Therefore, materials with a band gap of less than 1.23 eV or greater than 3.0 eV are theoretically unsuitable candidates for the overall water-splitting process. It is essential to emphasize

that even if a semiconductor material possesses the theoretically required minimum potential, it may not be practically achievable for a semiconductor to efficiently undergo water splitting. Various challenges in the reaction, such as bubble formation, gas release, and restricted electron transport, may impact its efficiency [12].

Diverse parameters that influence photocatalytic hydrogen generation activity are discussed below.

1.3.1. Sacrificial agent

Overall water splitting with a Gibbs free energy (ΔG) of 237 kJ/mol is a challenging and uphill reaction [13]. Multiple electron processes involved in half-reactions can diminish the efficiency of water splitting. To increase the activity of the hydrogen evolution reaction, sacrificial agents are used in the reaction environment, which act as hole scavengers and electron donors. In the reaction environment, the hole is captured by the sacrificial agent and prevents the unwanted recombination of electrons and holes. With the effective capture of holes, the OER process is effectively suppressed. Consequently, water splitting half reaction predominantly involves HER, where sacrificial agents such as various alcohols (methanol, ethanol), amines (triethylamine, triethanolamine), acids (formic acid, etc.), and diverse organic molecules play a vital role. These sacrificial agents facilitate HER by providing electrons for proton reduction, thereby augmenting the efficiency of the overall process.

1.3.2. Photosensitizer

Dye sensitizers enable wider light absorption by the semiconductor within the visible spectrum. Various types of organic dyes; including transition metal complexes, inorganic sensitizers, and specific organic dyes like Eosin Y, Erythrosin B, Rose Bengal are utilized as dye sensitizers [14]. The widespread adoption of these organic dyes in photocatalytic applications is attributed to their cost-effectiveness and low toxicity. Dye sensitizers expand the light absorption capacity of the semiconductor, enabling it to absorb more photons and form more electron-hole pairs, thereby increasing the photocatalytic activity

of the semiconductor. The dye sensitization mechanism initiates with the absorption of light by the dye molecule. Upon light excitation, electron transfer occurs from the highest occupied molecular orbital (HOMO) of the dye to its lowest unoccupied molecular orbital (LUMO). Subsequently, photo-induced electrons generated in the LUMO level of the dye are transferred to the semiconductor's CB. These electrons in the CB migrate to the active sites where various metals act as co-catalysts, facilitating water reduction and ultimately leading to H_2 evolution (**Figure 1.2**) [15].

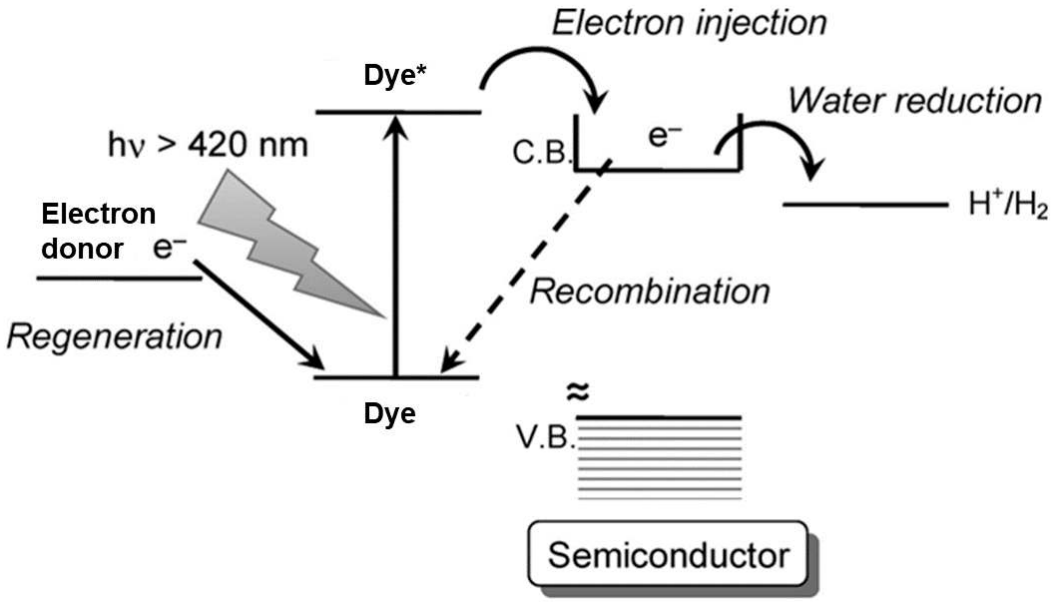

Figure 1.2. Dye-sensitized visible-light induced photocatalytic H_2 evolution mechanism. [16]

Eosin Y (EY) dye is a cheap and nontoxic organic dye molecule with a light absorption capability in the visible region. Considering its extended excited-state lifetime, appropriate redox potential, and significant quantum yield in the triplet state, it is an appealing organic photosensitizer for photocatalytic applications [17]. EY/Triethanolamine(TEOA) pairs are often used in photocatalytic hydrogen generation applications as dye-electron donor pairs [18]. It absorbs the green light in the spectral region at around 500 nm. EY plays a role in energy transfer or electron transfer processes in photoredox applications. The oxidation and reduction potentials of EY in its ground

and excited states have been reported and illustrated in **Figure 1.3.** For Eosin Y (EY) to be used as a dye sensitizer in semiconductor photocatalysis, its redox potentials must be compatible with the conduction band (CB) and valence band (VB) levels of the semiconductor. This compatibility ensures efficient electron transfer from the excited dye to the semiconductor, thereby improving its photocatalytic activity.

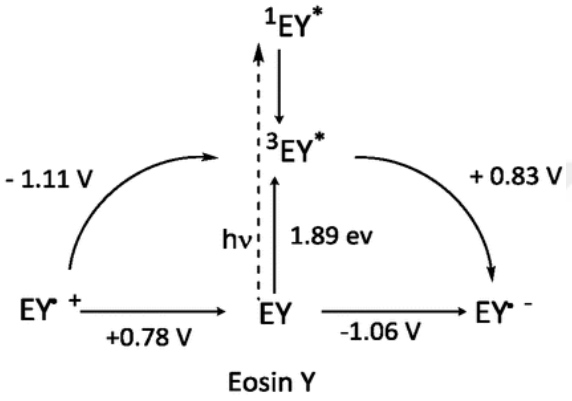

Figure 1. 3. Redox potentials of Eosin Y in ground and excited states in CH_3CN-H_2O (1 : 1) system. [19]

1.3.3. Co-catalyst

The effect of incorporating appropriate co-catalysts into semiconductor materials increases surface chemical reactions proton reduction to the H_2. The electric field created between the semiconductor and the co-catalyst contributes to the accumulation of electrons and holes in opposite directions, reducing the recombination of charge carriers and enhancing photocatalytic activity [20]. In addition, these co-catalysts act as active sites for surface oxidation and reduction reactions. The HER and OER reactions are both made possible by the presence of suitable co-catalysts on the semiconductor. Depending on the co-catalyst surface, either proton reduction or water oxidation occurs, and the adsorption behavior of different reactant molecules changes based on the properties of the co-catalyst [21]. As a result, the desired reactions, such as HER or hydrogenation reactions, take place. These co-catalysts will be examined in the subsequent literature survey section.

1.4.Hydrogen evolution reaction (HER): A Literature Survey

Many catalysts have been developed for HER research, each with its own advantages and disadvantages. Metal oxides such as TiO_x, WO_x, NiO_x,and CoO_x are tested in the photocatalytic HER [22-24]. However, some shortcomings limited the activity of these catalysts, such as surface passivation and low stability, leading to degradation of the structure over time [25]. In recent years, two-dimensional (2D) semiconducting materials have become the focus of research due to their unique properties owing to the absence of third dimension. These properties include interesting optical and electronic properties, mechanical properties, the easy modification of chemical and physical properties, and atomic thickness that gives a wider surface area. Among the semiconducting 2D materials, transition metal dichalcogenides (TMD),(MoS_2, $MoSe_2$, and WS_2 etc.) are used as alternatives to precious metal catalysts in photocatalytic HER applications owing to their exceptional properties such as structural tunability and modifiability in crystal structure [26-28]. They are typically used as co-catalysts with other semiconductors, facilitating the transfer of generated electrons and holes and serving as a bridge.[29] The TMD have provided promising results in photocatalytic HER, but research in this area still lacked the efficiency of metal catalysts and all developed materials were still significantly behind.

Semiconductor supported transition metal catalysts; including first-row transition metals (such as Ni, Cu, Co, Fe, and their alloys), noble metals((Pt, Pd, Au, Ag, Ru and their alloys), metal phosphides (e.g., PtP_2, Ni_2P), metal nitrides are effective for HER.[30-34] Although the first-row transition metals show relatively lower catalytic activity compared to noble metals in HER, their abundance in nature and cost-effectiveness make them favorable for large-scale applications. In comparison to noble metals, these non-noble metals have considerably lower stability, and their surfaces are more prone to corrosion and degradation [35].

Noble metals (Pt, Pd, Ru,Au, Rh) are commonly used to promote HER activity of semiconductors because their surface are distinguished by their unique catalyst characteristics [36-38]. They possess high work function, enabling effective electron

transfer to active sites on the metal surface, where they capture electrons [39]. By preventing charge recombination, they enhance photocatalytic activity of semiconductors. Noble metals are renowned for their robust resistance to corrosion and oxidation, enduring extreme conditions for prolonged periods while retaining superior catalytic properties. Considering their outstanding performance and durability, it may be reasonable to justify the higher prices of noble metals. Ongoing research aims to optimize the usage of noble metals in HER applications by incorporating them into various semiconductor materials as alloys, nanoparticles, or supported forms. This approach seeks to minimize the use of these metals while enhancing their performance, making them more economically viable and suitable for large-scale production.

Among noble metals, Pt distinguishes itself by its high work function and exceptional resistance to corrosion and oxidation, akin to its counterparts, and by possessing unique catalytic properties that elevate its status above other noble metals. These catalytic features render it the most active catalyst for photocatalytic HER. It has an appropriate Fermi level and a low overpotential, coupled with a suitable hydrogen adsorption energy [40; 41]. The hydrogen adsorption energy(ΔG_H) is a critical parameter determining H_2 performance. Strong hydrogen adsorption to the catalyst surface impedes the release of hydrogen, and Pt's ΔG_H value, which is nearly zero, establishes it as the optimal catalyst for H_2 evolution. [41; 42] **Figure 1.4**. shows the volcano-type plot of exchange current density(j_0) vs. ΔG_H over different metals [43].

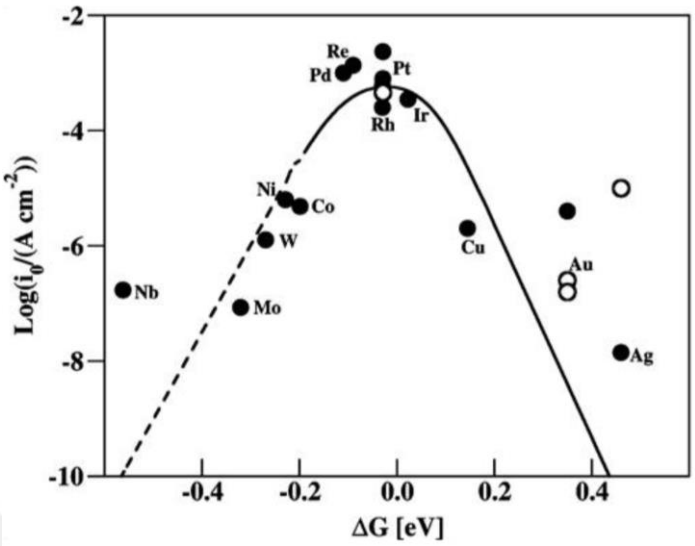

Figure 1.4. The exchange current density vs. calculated hydrogen adsorption energy (ΔG_H) over metals.

Metal nanoparticles possess numerous active sites suitable for diverse reactions; yet, their notably small sizes result in elevated surface energy, rendering them thermodynamically unstable [44]. Metal nanoparticles tend to aggregate, thereby their size enlarged resulting in a lower surface area and catalytic activity. Additionally, achieving a uniform distribution of metal nanoparticles poses challenges, resulting in inhomogeneous catalytic activity. In order to address these limitations, metal nanoparticles are incorporated into various support materials. These support materials facilitate the uniform distribution of metal nanoparticles within the structure, enhancing their interaction with reactants. Moreover, these support materials prevent nanoparticle aggregation. Metal nanoparticles that interact with support materials can be readily separated from the reaction mixture and reused for subsequent experiments. Integrating Pt nanoparticles into various support materials has resulted in heightened catalytic activities. The synergistic effects interplay between Pt nanoparticles and support materials improve the uniform distribution and stability of the metal nanoparticles and enhances the overall efficiency in photocatalytic hydrogen production processes. In photocatalytic HER applications, Pt NPs have been supported on a variety of support

materials, such as covalent organic frameworks (COF)[45], metal-organic frameworks (MOF)[46], covalent triazine-based frameworks (CTF)[47] titanium dioxide (TiO_2)[48],graphitic carbon nitride (g-CN)[37],and black phosphorus (BP)[6; 49; 50] These support materials represent the most thoroughly investigated categories, with further detailed outcomes provided in **Table 1.1.** Effective photocatalytic activity requires identifying an appropriate support material for integrating metal nanoparticles. This support should possess critical characteristics such as a wide surface area, broad light absorption, affordability, ease of synthesis, and non-toxicity. Satisfying these criteria, red phosphorus (RP) and black phosphorus (BP), as two stable phosphorus allotropes, have been chosen as support materials within the scope of this thesis. These phosphorus allotropes will be discussed in more detail in subsequent sections, highlighting their specific features. Metal nanoparticles have been supported on these materials to design diverse heterostructures for studies involving photocatalytic hydrogen production and the hydrogenation of different nitrobenzene compounds.

Table 1.1.Catalytic activity of Platinum based catalysts for HER

Metal catalyst	**Amount of evolved H_2 ($\mu mol\ g^{-1}\ h^{-1}$)**	**Ref**
Pt_1@TpPa-1-COF	719	[42]
PtSA-MNS	11 320	[43]
Pt-CTF	614.6	[45]
TiO_2-HMSs@xPt	11700	[48]
Pt/CN-BH-H	2316	[37]
BPNss/Pt	90	[50]

SA-Pt/g-C_3N_4	22650	[51]
Pt_5/CdS	13000	[52]
Pt–Ti^{3+}/TiO_2	151 (μmol m^{-2} h^{-1})	[53]
CZTS–PtCo	1850	[54]
Ni–Pt/TiO_2	1270	[55]
Au@CeO_2–Pt	8.7	[56]
Pt@PtSAs/PCNS-1	15750	[57]
CdS/Pt/N-$NaNbO_3$	29297	[58]
BP NS/Pt/TMC	1.9	[59]
Pt-BP/CdS	24170	[60]

TpPa-1-COF = Two-dimensional β-ketoenamine-linked covalent organic frameworks, PtSA-MNS=Pt single-atom-coordinated ultrathin MOF nanosheets, CTF-BP-Pt=Covalent triazine based framework-Black phosphorus(BP)-Pt, HMSs= hierarchical microspheres CN-BH-H= graphitic carbon nitride (g-CN), BPNss=Black phosphorus nanosheets, CZTS=Cu_2ZnSnS_4, GO–CdS–Pt= Graphene oxide–Cadmium sulfide–Pt, PtSAs/PCNS= Pt single atom polymeric carbon nitride,$NaNbO_3$=Sodium niobate, BP NS/Pt/TMC =black phosphorus nanosheets/TiO_2 mesocrystals/Pt

1.4. Fundamentals of Photocatalysis

In the previous chapters, mechanisms of photocatalytic processes have been discussed. This section will address semiconductor properties that have yet to be previously covered. Photocatalysis is a process wherein a catalyst absorbs incident

photon, whether ultraviolet, visible, or near-infrared radiation and induces chemical transformations by increasing the reaction rate [61]. In photocatalysis, semiconductors are commonly used to absorb photons. The role of these semiconductors is to absorb visible light, leading to the excitation of electrons and the formation of electron-hole pairs. In the term "semiconductor," "conductor" denotes electrical conductivity. Semiconductors possess an electrical conductivity that lies between that of a conductor and an insulator (**Figure 1.5**). The rationale behind semiconductor's use in photocatalytic applications is inherently linked to their band gap characteristics. Typically, semiconductors exhibit a band gap ranging from 1 to 3 eV, giving them a broad light absorption capability. In contrast, conductors either have a negligible band gap or lack one entirely. Conversely, insulators are characterized by a considerable separation between the valence band and conduction band, a feature that results in a significant band gap. This wide band gap hinders the excitation of electrons [62].

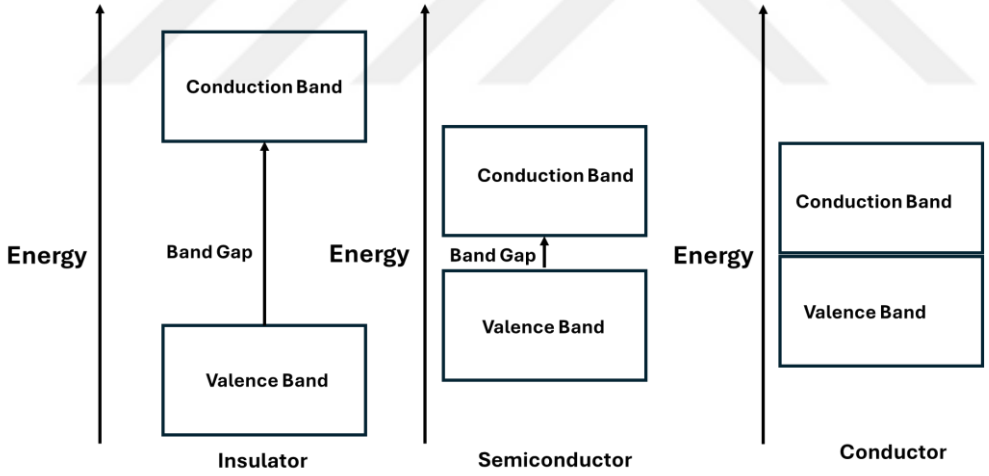

Figure 1.5. The schematic energy band diagrams of insulator, semiconductor and conductor.

Semiconductors are divided into two categories: intrinsic semiconductors and extrinsic semiconductors. Intrinsic semiconductors consist of pure, undoped materials, such as crystalline Si while extrinsic semiconductors incorporate impurities and are doped with other elements. Extrinsic semiconductor materials are classified as p-type if they

contain free holes and n-type if they contain free electrons on doped narrow-band donor material (**Figure 1.6**). Therefore, if electron donors are introduced into the crystal lattice through a dopant, they are n-type semiconductors. Conversely, if an electron acceptor creates voids within the semiconductor by accepting electrons from the crystal, it is classified as a p-type semiconductor [63].

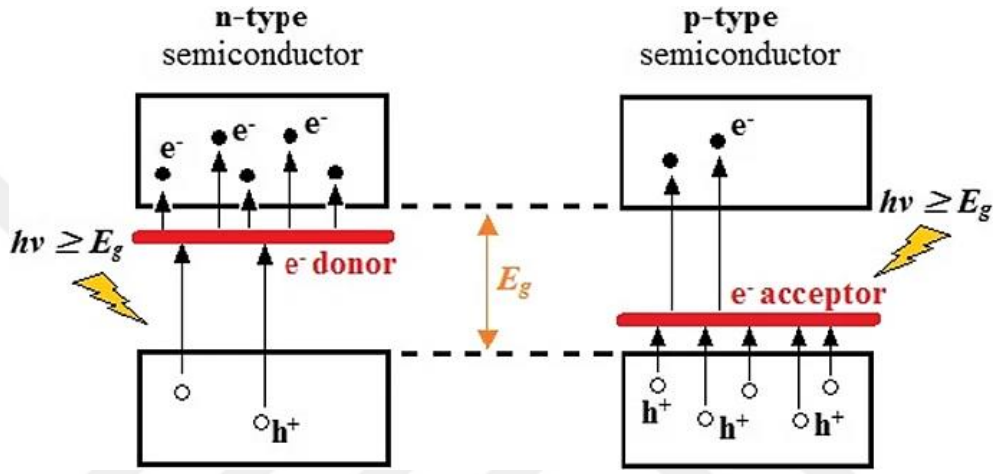

Figure 1.6. Schematic illustration of n-type and p-type semiconductor. [63]

Adding electron donors or acceptors into a semiconductor's lattice alters its electrical, optical and thermal properties. This ability to modify the semiconductor type through doping allows for the engineering of materials for specific applications. However, the presence of inevitable impurities and the inhibition of hole injection due to the high Schottky barrier, which results from the Fermi level pinning at the metal and the semiconductor interface, hinders the formation of p-type semiconductors.[64] Consequently, most semiconductors tend to exhibit n-type behavior. Constructing p-type or n-type semiconductor structures aims to enhance or manipulate semiconductor materials' optical and electrical properties, thereby enhancing their photocatalytic performance. By adopting this strategy, the creation of heterostructures will enable the efficient seperation of electrons and holes, thus enhancing the efficacy of photocatalytic processes.

1.5.Heterojunction Photocatalysts and 2D semiconductor materials

In photocatalysis, the performance offered by a single semiconductor material can be limited. For example, it has been reported in numerous studies that when 2D materials such as graphitic carbon nitride, black phosphorus, or red phosphorus are used solely in photocatalytic processes, their photocatalytic performance is diminished due to the rapid recombination of electrons and holes. Constructing heterostructures with these semiconductor materials helps prevent charge recombination, enhances light absorption, and increase catalytic activity [65]. The prefix "hetero" in heterojunction signifies "different" or "other," indicating the connection formed by combining materials with distinct structures. As a result, heterostructures enable broader light absorption across a wider spectrum, facilitating the adjustment of band levels and redox potentials necessary for desired reactions. This allows heterostructures to harness a more comprehensive light spectrum range, thus enhancing their photocatalytic performance. Adjustments of redox potentials and band levels enables the reactions to occur.

Heterostructures can be formed through interactions between semiconductor-semiconductor, semiconductor-carbon, or semiconductor-metal [66]. In the interaction between two semiconductors, the difference in their Fermi levels causes electrons to flow from the semiconductor with a higher Fermi level to the one with a lower Fermi level. When the system reaches equilibrium, the bands of the contacting semiconductors bend in response to the movement of the Fermi levels. This electron flow leads to the formation of different band structures, classified as type-I, type-II, type-III, and S-scheme (**Figure 1.7**) [67].

Type-I heterostructure is formed when holes and electrons in the VB and CB of excited semiconductors flow from a semiconductor with a higher band gap to one with a lower band gap (**Figure 1.7a**). In a type-I heterostructure, charges accumulate in a single semiconductor, resulting in less effective separation of electrons and holes. Consequently, this type of heterostructure is considered less efficient than other types. In a type-II heterostructure, the CB and VB levels of one semiconductor are higher than those of the other (**Figure 1.7b**). Upon excitation by light, electrons flow from the semiconductor with

the higher CB level to the one with the lower CB level. In comparison, holes flow from the semiconductor with the lower VB level to the one with the higher VB level. This band structure, where electrons and holes are collected in different regions, effectively reduces electron-hole recombination. In the type-III heterostructure, also known as a broken band heterostructure, the band levels of the two semiconductors do not overlap (**Figure 1.7c**). This lack of overlap necessitates a high driving force to promote charge flow [68]. To address this challenge, researchers have developed an enhanced version of the type-III structure, type-B. In this configuration, metal nanoparticles are inserted between the two semiconductors, serving as a bridge to facilitate charge flow.[69] The metal nanoparticles effectively promote charge transfer between the semiconductors, overcoming the limitations of the conventional type-III heterostructure. The band structure of an S-scheme heterostructure resembles that of a type-II heterostructure but differs in the pathways for charge accumulation. An S-scheme heterostructure combines a reduction-type semiconductor with an oxidation-type semiconductor (**Figure 1.7d**). The interaction between these semiconductors generates an internal electric field, which drives electron flow from the oxidation-type semiconductor's CB to the VB of the reduction-type semiconductor. As a result, holes are depleted in this process, causing band bending [67]. This configuration allows for charge recombination at lower energy levels while preventing recombination at higher energy levels, thus enhancing the separation of charges and improving overall efficiency.

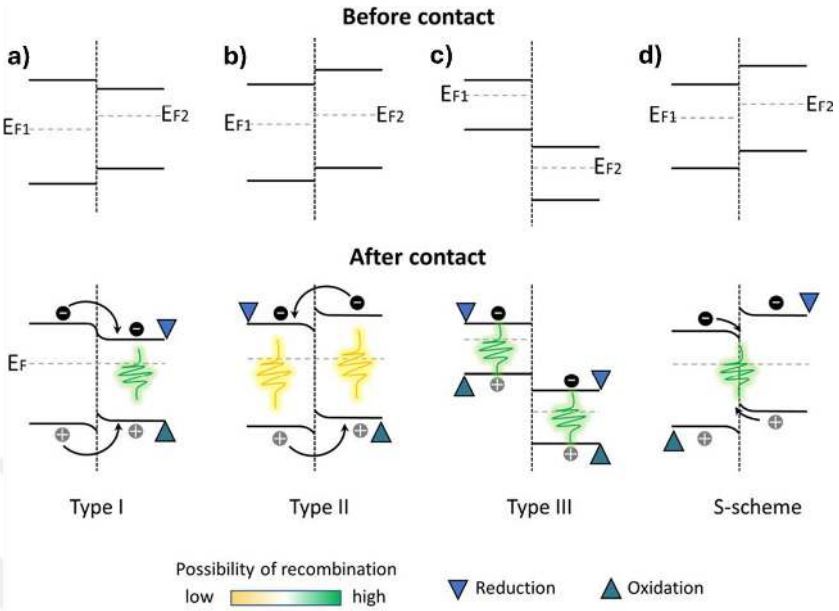

Figure 1.7. Schematic illustration of the band structures of semiconductor-semiconductor heterojunctions. [67]

The interaction between the semiconductor and metal, particularly the formation of a Mott-Schottky junction between noble metals and semiconductors, enhances the photocatalytic performance of the semiconductor. Noble metals typically have a higher work function(φ) than semiconductor materials. Two types of Schottky junctions can be formed, depending on whether the semiconductor is n-type or p-type. When a metal and an n-type semiconductor come into contact, electrons flow from the semiconductor, which has a higher Fermi level in the case of n-type, to the metal with a lower Fermi level until their fermi levels reached to equilibrium (**Figure 1.8**). This results in the semiconductor becoming electron-deficient (forming a depletion region) and the metal becoming electron-rich. This interaction creates an electron-depleted area at the semiconductor-metal interface. Because of this electron depletion in the semiconductor, an upward bending occurs in the semiconductor, forming a Schottky barrier. This barrier inhibits the backflow of electrons from the metal to the semiconductor, promoting more effective charge carrier (electron-hole) separation. When p-type semiconductors come into contact with metal, electrons flow from the metal with a lower work function to the semiconductor with a higher work function. Consequently, the metal region becomes

electron-deficient, whereas the semiconductor region becomes electron-rich. This process results in the downward bending of the semiconductor' bands. The height of the Schottky barrier is related to the metal's work function and the semiconductor's electron affinity. The magnitude of the Schottky barrier height determines the effectivity of the seperation of electrons and holes [70]. This mechanism is particularly beneficial in devices like Schottky diodes and photocatalytic applications, where performance is dependent on efficient charge seperation. The performance of a Schottky junction system can be enhanced by shifting the Fermi level, which is related to the work function. The maximum separation of charge carriers is associated with the high work function of the metal. Among noble metals, platinum (Pt) has a high work function, making it an effective electron trap that facilitates electron-hole separation [71].

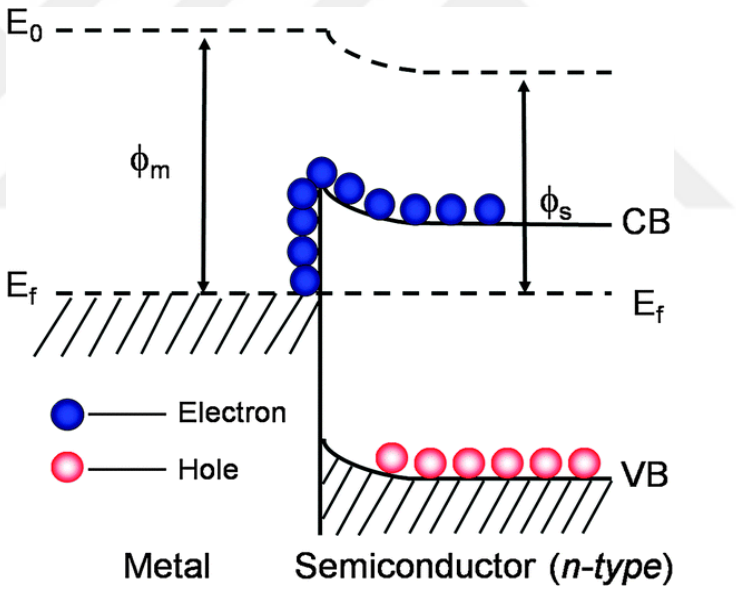

Figure 1.8. Schematic illustration of the Schottky junction formation. [66]

1.5.1. Phosphorus based photocatalysts: Red Phosphorus and Black Phosphorus

In recent years, the scientific community has recognized the role of metal-free 2D semiconductor materials such as graphitic carbon nitride (g-CN), transition metal dichalcogenides (TMDCs), phosphorene in energy applications due to their simple elemental compositions yet numerous excellent properties. This interest is owing to their

simple elemental compositions and numerous excellent properties. The elements constituting these semiconductors are abundant in nature, easy to synthesize, cost-effective, and environmentally friendly. Moreover, their structures are highly adaptable for modification, facilitating the incorporation of numerous active sites. Their stable structures have made them the focus of multiple studies and research efforts in various energy-related fields, including photocatalysis. Phosphorus-based photocatalysts are considered suitable semiconductor materials for photocatalytic H_2 production [72]. Phosphorus(P) exists in nature in stable forms, including elemental phosphorus (P^0), phosphate (P^{5+}), and phosphide (P^{-3}). Elemental phosphorus can combine with metals and non-metals to form compounds such as metal phosphide, metal phosphate, or numerous inorganic complexes [73]. Elemental phosphorus has three allotropes: white P, black P, and red P. Among these, white P is highly reactive and quite unstable. Given the availability for more stables allotropes, white P is not suitable for photocatalysis applications. In recent years, Black Phosphorus (BP) has emerged as an attractive 2D material for photocatalytic applications, representing the most stable allotrope of phosphorus thermodynamically. BP features a bandgap that can be adjusted from 0.3 eV in bulk form to 2 eV in monolayer form, allowing for a broad spectrum of light absorption. While bulk BP can absorb light across a wide range from ultraviolet to infrared, its CB value is insufficient for photocatalytic H_2 production. Layering BP creates a negative shifting effect on the CB value [74]. Therefore, in its monolayer (phosphorene) and few-layer forms, BP can be a suitable semiconductor material capable of photocatalytic H_2 production. **Figure 1.9** illustrates the orthorhombic crystal structure of BP, where phosphorus atoms arrange themselves in a honeycomb lattice. In monolayer BP, sp^3 hybridized P atoms form covalent bonds within layers. Adjacent layers are weakly connected through van der Waals interactions along the z-axis. This layered arrangement allows for obtaining single-layer or few-layer BP from bulk crystals through a process known as exfoliation. Due to the presence of a lone pair of electrons on each phosphorus atom, it is susceptible to oxidation in air. Phosphorene, the single-layer form of BP, consists of hexagonal rings of six P atoms through sp^3 hybridization. Orthorhombic BP is synthesized using relatively challenging, time-consuming, and intricate methods,

including bulk crystal growth, mechanical exfoliation, direct thin film growth, and liquid exfoliation techniques [75]. BP was first prepared in 1914 by Bridgman from white P at a pressure of 1.2 GPA and a temperature of 200 ^{o}C with the Bridgman method [76]. It was recently reported by Lange et al. that BP can also be synthesized under reduced pressure. This technique, known as the chemical vapor transport method, allows the synthesis of high-quality BP crystals at 600°C in silica ampoules, using red P as the phosphorus allotrope and Au, Sn, and SnI4 as mineralizers [77]. In recent years, BP crystals have been successfully synthesized in a convenient method using suitable solvent and in an ambient pressure under solvothermal conditions, also referred to as the wet-chemical synthesis method. This approach typically involves the growth of BP crystals in the presence of a suitable stabilizer. This advancement will be elaborated upon in the literature review section.

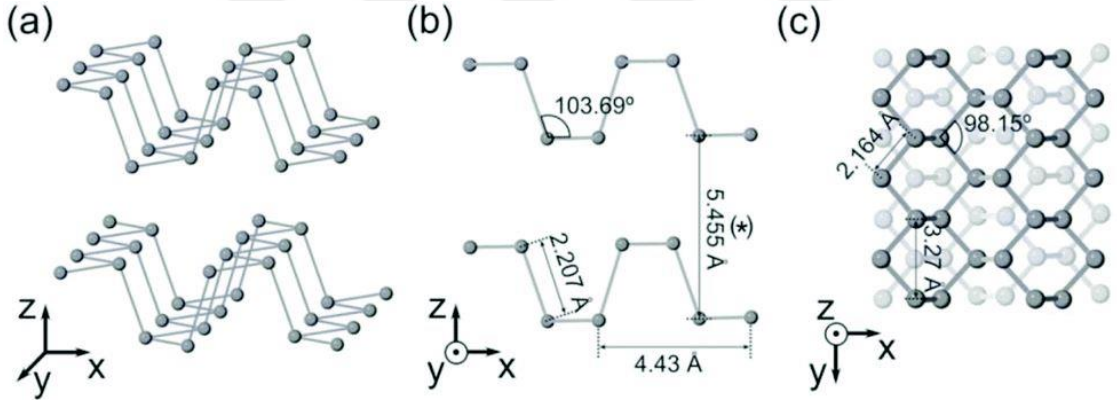

Figure 1.9.Crystal structure of few layer BP. [69]

Red phosphorus (RP) is a stable allotrope of phosphorus that has garnered significant attention in photocatalysis due to its high abundance, low production cost, and easy accessibility. After Wang et al. first utilized RP for photocatalytic H_2 production in 2012, scientific research on the application of RP as a photocatalyst gained momentum [78].

Metal-free RP has emerged as a versatile photocatalyst across diverse fields in recent years. Its applications range from energy storage solutions to flame retardancy and

smoke detection systems. Additionally, RP has gained recognition as an innovative anode material in sodium (Na) and lithium (Li)-ion batteries, and it is celebrated for its exceptional capacity and performance. [79] RP is distinguished into five specific types: types I through V. Among these, type I red phosphorus (RP) exhibits an amorphous structure, while the other forms—hexagonal (type II), metastable (type III), fibrous phase (type IV), and the Hittorf phase (type V)—are crystalline (**Figure 1.10**). These allotropes exhibit versatile optical properties, enabling the absorption of light across a broad spectrum of wavelengths, from the visible to the near-infrared (NIR) region. However, the characteristics and potential applications of hexagonal (type II) and metastable (type III) RP still need to be fully explored, highlighting a gap in the current understanding and application of RP types [80]. On the other hand, amorphous red phosphorus (type I) has gained considerable interest due to its commercial availability and the ease with which it can be accessed without requiring specialized processing techniques, making it a practical and cost-effective option for various industrial and research applications.

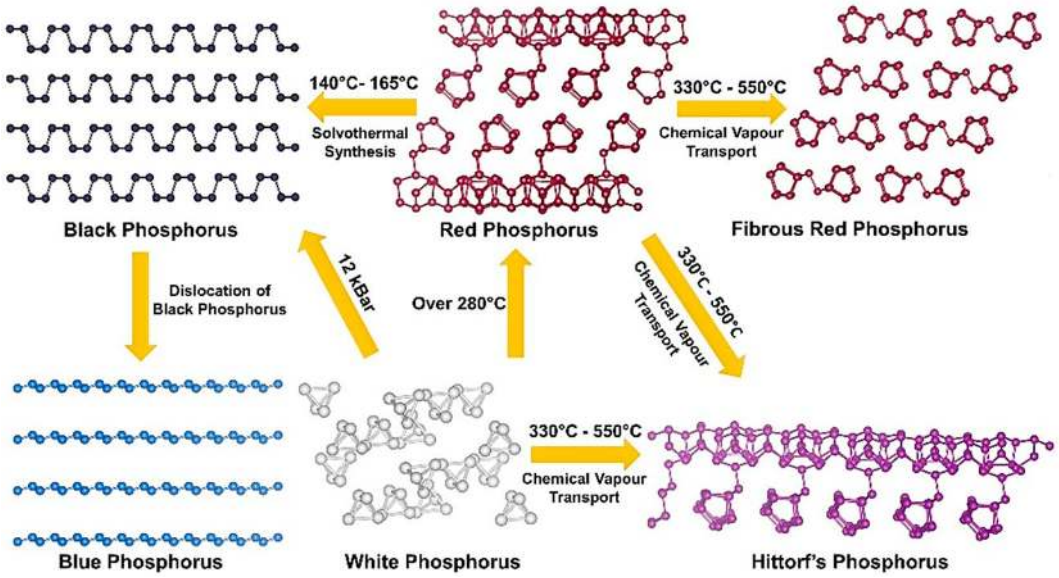

Figure 1.10.Different Phosphorus allotropes and synthesis methods. [70]

Density functional theory (DFT) studies have shown that RP has a layered structure similar to BP. [81] With this layered structure, RP features a band gap range from 1.4 to 2 eV from bulk to monolayer or few-layer forms. A band gap below 2 eV

enables extensive light absorption across a broad spectrum, and the optimal CB and VB values position RP as a promising photocatalyst for photocatalytic HER. The theoretical band gap of red phosphorus (RP) indicates that it can absorb light across a broad spectrum; however, its photocatalytic performance is limited due to restricted charge carrier dynamics. Jing et al. conducted an analysis using ultrafast time-resolved absorption spectroscopy (TAS) to investigate the charge carrier dynamics of RP. [82] They observed that due to trap states (TS) in the forbidden band of RP, electrons are captured in the TS region, making deep trapping difficult (**Figure 1.11**). As a result, charge recombination accelerates, leading to a reduction in its photocatalytic activity. To overcome the factor limiting the performance of RP, using metals acting as trap sites to capture electrons effectively would be a practical approach.

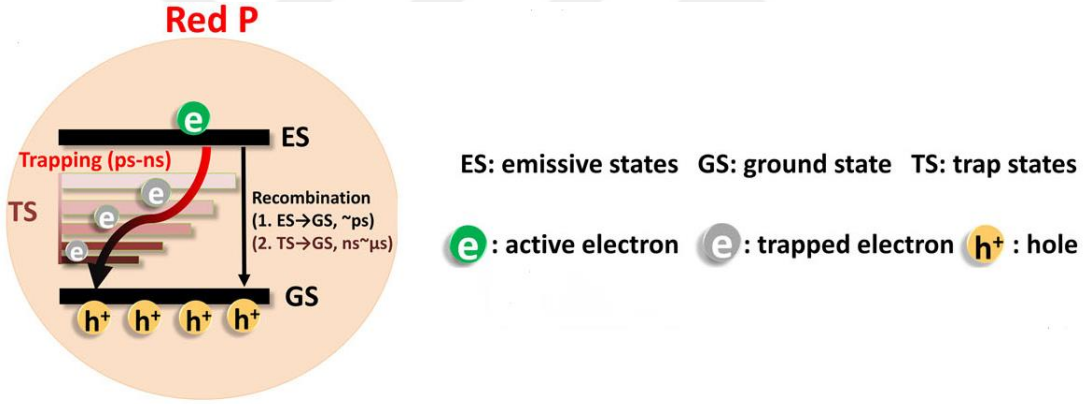

Figure 1.11. Charge dynamics in RP. [82]

1.6. A Literature survey on the Red Phosphorus and/or Black Phosphorus-based Heterojunctions

As discussed in the section outlining the general properties of RP and BP, these photocatalysts, despite their numerous advantages, also possess specific limiting characteristics. Therefore, in the literature, various heterojunctions have been formed alongside their standalone usage to enhance the activity of these semiconductor materials. These heterojunctions have demonstrated activity in multiple fields ranging from photocatalytic hydrogen production, degradation of organic pollutans, to battery

applications and beyond.

Liu et al. designed an RP/Ni_2P by using an in situ hydrothermal. They utilized TEOA as a hole scavenger and reported the heterostructure's photocatalytic hydrogen production activity as 2183.32 μmol g^{-1} h^{-1} [83]. Ni_2P species have been noted to provide the active sites necessary for the photocatalytic HER and facilitate the effective separation of charges, thereby enhancing photocatalytic activity. Ziu et al. designed the Bi_2O_3 hydrothermal-treated Red Phosphorus (HRP) structure using a hydrothermal method and investigated the photoreduction of Cr(IV) contaminant with the synthesized heterostructure. They reported that the newly formed heterostructure increased the charge concentration and enhanced the catalytic performance of the photocatalytic Cr(IV) reduction [84]. Yan et al. synthesized a 3D crystalline RP/RGO structure by first positioning nanoseeds followed by secondary growth. The synthesized composite was utilized for the first time as anode in sodium-ion batteries, achieving highly competitive results with 93.5% of the theoretical capacity and a Coulombic efficiency of 82%. The promising results of the composite were attributed to the strong interaction between RP and RGO and the porous structure of the electrode [85]. Yuan et al. designed a type I RP/g-CN heterostructure and investigated its activities in photocatalytic HER and photocatalytic CO_2 conversion to valuable hydrocarbon fuel, CH_4. The RP/g-CN heterostructure achieved an activity of 1000 μmol h^{-1} g^{-1} in HER and a CH_4 production yield of 295 μmol h^{-1} g^{-1}. In the established heterostructure, while H^+ or CO_2 is reduced on RP with the electrons, the holes on g-CN facilitate the oxidation of sacrificial agents [86]. Huang et al. constructed an RP/TiO_2 heterojunction using the chemical vapor deposition method. They investigated the activity of this catalyst in photocatalytic hydrogen production and reported a hydrogen production rate of 215.5 μmol/(g h). In this study, they observed that RP acts as a light absorber, enhancing the heterojunction's ability to absorb light [87]. Dou et al. constructed an Ag/RP structure using the photo-deposition method. They observed the activity of this catalyst in the photocatalytic degradation of a methyl orange (MO) dye solution. It was determined that Ag ions act as an electron trap site and reacts with O_2 to produce reactive O_2^- species that facilitate the

MO degradation [88]. Qi et al. obtained three-dimensional RP (3D-RP) from commercial RP using the hydrothermal method. They observed the photocatalytic HER of RP/Au and RP/Cu, which was designed with in-situ added Au and Cu ions. They achieved hydrogen production rates of 195.27 and 238.26 μmol g^{-1} h^{-1} for RP/Au and RP/Cu, respectively. These rates are 2.32 and 2.77 times greater than RP alone (81 μmol g^{-1} h^{-1}). It was determined that the energy of the electrons was increased due to the surface plasmon resonance (SPR) effect of Au and Cu, which facilitated the reduction of H^+ to H_2 [89]. Our group constructed a complex type II RP/g-CN-Pt heterojunctions by using an ultrasound-assisted two-step protocol and examined the catalyst's activity in the photo-assisted hydrolysis of ammonia borane (AB). The construction of a Schottky junction with Pt nanoparticles enhanced the heterojunction's optical properties compared to its pristine derivatives, achieving hydrogen gas production of 142 mol H_2·mol Pt^{-1}·min^{-1}. [90]

Following RP and RP-based heterostructures, as mentioned earlier, the intriguing allotrope of phosphorus, BP, has been also studied. BP has demonstrated activity as a standalone photocatalyst and in various heterostructures formed with BP, showing catalytic activity in diverse applications. Our group employed BP for the first time as a photocatalyst in the C-H arylation of heteroarenes with diazonium salts [91]. They achieved favorable yields in the arylation of furans and thiophenes with various diazonium salts containing electron-donating and withdrawing groups. In this study, BP crystals were synthesized using a method known as the SnI_4-assisted low-pressure synthesis method, and BP nanosheets were obtained by sonication-assisted liquid-exfoliation method [92]. This method, while seemingly straightforward for obtaining BP nanosheets, involves a 2-step process that requires a considerable amount of time. In this regard, Tian and colleagues have developed a method for obtaining BP nanosheets using a one-pot wet chemical synthesis approach. They successfully synthesized BP nanosheets at low temperatures by employing white phosphorus as the P source and ethylenediamine (EDA) as the solvent. Characterization results have shown that BP can be effectively obtained through this facile solvothermal synthesis method [93]. Sun et al. have

synthesized BP crystals for lithium-ion battery applications using liquid-phase low-temperature method at temperatures ranging from 120 to 200°C, with RP as the P source and EDA as the solvent. The researchers investigated the role of EDA; they found that EDA acts as an electron donor, while BP's P_4 unit acts as an electron acceptor. They observed that electrons are transferred from the HOMO of EDA to the LUMO of the P_4 molecule. The activated P_4 molecules combine to form P_8 units and serve as templates for further growth [94]. Sun et al. synthesized BP, which they referred to as "quasi-monolayer BP," using a wet chemical synthesis method with RP and EDA. This form of BP is in bulk but possesses a monolayer's direct band gap characteristics. Due to the quantum confinement effect, they reported that EDA-intercalated quasi-monolayer BP has a wider band gap and more robust redox capability than non-intercalated BP. Furthermore, the charge interactions between EDA and BP lead to stronger charge separation and increase the rate of H_2 evolution [95]. Liu et al. designed a BP/RP heterojunction using a one-step wet chemistry method with RP and EDA as the solvent to observe its photocatalytic water-splitting activity; this heterostructure has shown increased H_2 evolution activity compared to both BP and RP. Characterization studies revealed that the charge transfer between RP and BP is by a Z-scheme mechanism [96]. Zhu et al. employed a one-step solvothermal synthesis approach to synthesize BP nanosheets using RP and EDA within an autoclave at temperatures ranging from 140 to 170°C. They evaluated the efficiency of BP naosheets as photocatalysts in HER. The findings revealed that the BP nanosheets demonstrated an activity level 40.6 times greater than that of pristine RP [97]. Ozawa et al. have synthesized BP using a one-pot solvothermal synthesis method with RP and EDA as the solvent. Subsequently, using the photo deposition method, they deposited Pt and Co onto BP to observe the photocatalysts' HER activity. The Co-loaded BP demonstrated higher activity than Pt-loaded BP, attributed to the formation of cobalt phosphide species on the Co-loaded BP. EDA in solvothermal synthesis methods for BP plays a multifaceted role, serving as a solvent, electron donor, and chelating agent. This versatility makes EDA particularly valuable in the preparation of BP nanosheets [98]. Wang et al. prepared BP nanosheets using ultrasonic probe followed by bath sonication in an appropriate solvent. After washing and drying procedures, they obtained the catalyst by adding Pt NPs

solution to yield BP-activated Pt catalyst. They achieved 6.1 times higher HER compared to the state-of-the-art commercial Pt/C [99]. Bai et al. utilized the same method as the previous study to obtain BP nanosheets. Then, they prepared BP/Pt heterostructures by adding Pt precursor and other chemicals onto the BP nanosheets. These heterostructures were used for photocatalytic hydrogenation of styrene and benzaldehyde and photocatalytic oxidation of benzyl alcohol reactions [6]. Prior research motivated us to explore the potential for in-situ generation of transition metal NPs during the solvothermal conversion of RP to BP. Following an extensive literature review, we found no previous instances of employing the solvothermal method for the direct, single-step synthesis of platinumNPs supported on BP using stable and non-toxic RP as precursor.

1.7. Hydrogenation Reactions

Hydrogenation is a chemical reaction that involves the reduction of unsaturated molecules, such as alkenes and alkynes, by adding hydrogen atoms to them, thereby converting these molecules into saturated molecules. Hydrogenation is one of the most critical methods in various industries, such as ammonia synthesis, oil refining, pharmaceutical industry. Raw materials across multiple sectors, ranging from additives in the food industry to pharmaceutical intermediates and hydrocarbons to laboratory chemicals, are obtained through the hydrogenation process. French chemists Paul Sabatier and Jean-Baptiste Senderens synthesized methane and water from carbon dioxide in the presence of a nickel catalyst and hydrogen gas, laying the groundwork for the hydrogenation reaction. After being awarded the Nobel Prize in 1912, they continued their research on numerous hydrogenation reactions, gaining enormous attention in the petrochemical industry and scientific community. Through their efforts, the importance of hydrogenation reactions has become increasingly recognized [100]. A recent example also highlights the significance of hydrogenation is the work of Knowles and Noyori, which earned them the Nobel Prize in Chemistry in 2001 for their contributions to asymmetric hydrogenation. Their research aimed to reduce the side effects of drugs by producing only one of the chiral molecules, a technique that now holds a valuable position in the pharmaceutical industry [101]. Hydrogenation is a reduction reaction that involves

the gain of electrons or a decrease in the oxidation state of a molecule or atom. The term "reduction" is frequently favored in organic chemistry for the synthesis of various compounds, involving alcohols from aldehydes and ketones. This preference stems from the substantial alteration in the oxidation state that occurs rather than solely from the addition of hydrogen. An important example for the reduction reaction is the transformation of nitrobenzene into aniline. Nitrobenzene can be reduced to aniline in the presence of hydrogen gas and a metal catalyst such as palladium or platinum. Hydrogen atoms are added to the nitro group of nitrobenzene, resulting in the conversion of nitrobenzene to aniline. During this process, nitrobenzene gains hydrogen, and a significant change in oxidation state is observed. Since the process involves electron transfer, indicating not only hydrogenation but also the involvement of other processes in the reaction, it shows that nitrobenzene is being "reduced" to aniline.

Hydrogenation reactions can be carried out through various methods, including conventional catalytic hydrogenation, where molecular H_2 gas is used as the hydrogen source, or transfer hydrogenation, which utilizes hydrogen storage materials as the hydrogen source. The conventional catalytic hydrogenation method involves the reduction of unsaturated molecules via supplying molecular H_2 gas to the unsaturated bonds, such as double or triple bonds, in the presence of a metal catalyst. This process appears effective regarding catalytic activity and product selectivity but requires high reaction temperatures and continuous feeding of H_2 gas into the system. Transporting and storing compressed hydrogen gas necessitates special safety precautions, and keeping hydrogen tanks in laboratory environments can pose security risks. The transfer hydrogenation method involves using hydrogen carriers such as isopropanol, formic acid, ammonia borane (AB), and sodium borohydride ($NaBH_4$), among others, instead of molecular H_2 gas as the hydrogen source [102-105]. Unlike the conventional hydrogenation method, which requires complex reaction setups or a continuous flow of H_2 gas into the system, transfer hydrogenation offers a reliable alternative for hydrogenation reactions. This method has gained popularity as hydrogen carriers are readily available and economical, making transfer hydrogenation a practical and efficient

approach for various hydrogenation reactions [106]. Metin et al. conducted a study on the transfer hydrogenation of nitroarenes to anilines using FePd nanoparticles supported on reduced graphene oxide (rGO). They demonstrated that various nitrobenzene compounds could be efficiently reduced to corresponding anilines with good yields through a reaction carried out in the presence of AB at room temperature and within a short reaction time [107]. Metin et al. synthesized Ag/Pd core/shell nanoparticles (NPs) supported on reduced graphene oxide (rGO) and attained high product yields in reducing nitroarenes to anilines within a short reaction times (5-15 minutes). This reaction was conducted with AB as the hydrogen donor [108]. Göksu et al. synthesized a G-NiPd catalyst by supporting NiPd alloy nanoparticles on graphene (G). They investigated its catalytic efficiency in the hydrogenation of nitrobenzene derivatives to aniline compounds, using ammonia borane (AB) as the hydrogen source. They achieved high yields of aniline compounds within a short reaction time of 5-30 minutes [109]. Can et al. investigated the reduction of nitrobenzene to aniline using the rGO/Co-Ru catalyst they synthesized. They used morpholine borane (MB) as a hydrogen source under optimized reaction conditions of 100°C and 60 minutes [110]. Dağalan et al. investigated the transfer hydrogenation reaction of quinoline derivatives using AB as a hydrogen source with the m-CN/CoPd catalyst. They achieved significantly high product yields with reactions conducted in the 60-80°C temperature range for 6-8 hours [111]. Ganjehyan et al. developed an experimental procedure that facilitates the transfer hydrogenation of various groups using the rGO-supported CuPt nanoparticles synthesized as the rGO-CuPt catalyst. They investigated the transfer hydrogenation of olefins, aldehydes/ketones, and nitroarenes in the presence of ammonia borane (AB) as the hydrogen donor, achieving up to 99% high product yields [112]. Nişancı et al. advanced the concept further by developing a three-component sequential reaction process. In their method, the process entails 1) the reduction of Pd(II) ions to Pd(0) NPs, 2) the dehydrogenation of AB catalyzed by in situ formed mpg-CN/Pd, and 3) the transfer hydrogenation of various nitrobenzene derivatives with the H_2 gas produced from the AB dehydrogenation, resulting in the formation of aniline compounds [113]. In conclusion, the studies mentioned have demonstrated the potential of transfer hydrogenation methods using various catalysts and

hydrogen sources. Through the exploration of diverse experimental procedures and reaction conditions, all of these studies collectively indicate that reduction reactions can be effectively carried out using the transfer hydrogenation method.

Photocatalytic hydrogenation offers advantages over conventional catalytic hydrogenation methods. Firstly, using a photocatalyst activated by light allows for initiating hydrogenation reactions at lower temperatures and milder reaction conditions. This not only reduces energy requirements but also increases the overall efficiency of the process. Furthermore, photocatalytic hydrogenation offers a more sustainable and environmentally friendly approach to hydrogenation. This is because using a photocatalytic system inspired by sunlight, a renewable energy source, reduces dependence on fossil fuels and minimizes carbon emissions. It is evident from the research conducted by Liu et al. that light plays a significant role in the reduction of nitrobenzene. The observed decrease in activation energy from 104.4 kJ/mol in the dark system to 20.4 kJ/mol in the visible-light irradiated system highlights the substantial impact of light-irradiation on the reaction conditions [114] (**Figure 1.12**). This finding underscores the potential of light-induced systems in enhancing the efficiency of photocatalytic reduction reactions.

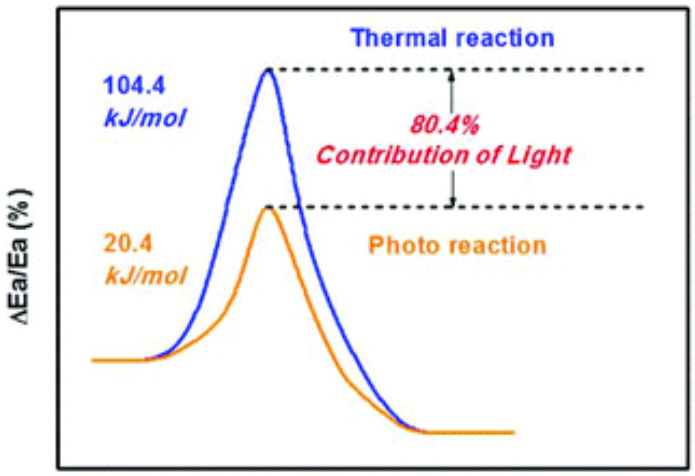

Figure 1.12.Apparent activation energies of nitrobenzene reduction: Photoreaction vs. thermal reaction in the dark. [114]

Semiconductor-based photocatalytic hydrogenation is a process that drives chemical reaction through the absorption of light. This process involves the generation of electrons and holes in the semiconductor when it absorbs light. The electrons migrate to the semiconductor's CB, while the holes remain in the VB. For a semiconductor to facilitate the photocatalytic transformation of an organic group, its CB level needs to be more negative than the reduction potential of the organic molecule. This alignment ensures that the excited electrons in the CB have sufficient potential to be transferred to the organic molecule, reducing it in the process [115]. Metal atoms supported on the semiconductor act as trap for the electrons transferring from semiconductor, capturing them. If atomic hydrogen acts as the reducing agent for the hydrogenation reaction, these trapped electrons then participate in the reduction of hydrogen protons adsorbed on the metal surface, forming atomic hydrogen species. These atomic hydrogen species then react with substrates adsorbed on the metal surface, leading to the reduction of the substrate and the formation of the target molecule. With a similar approach, Tsutsumi et al. investigated the photocatalytic reduction of nitroarene derivatives using a Pd-loaded Si photocatalyst. Upon illumination, the semiconductor silicon (Si) generated electrons in the CB and holes in the VB. The electrons were transferred from Si to Pd, where they encountered protons on the metal surface, leading to the formation of atomic hydrogen. Subsequently, this atomic hydrogen effectively reduced nitrobenzene adsorbed on the metal surface to produce aniline [116]. The crucial point here is that, prior to the HER step, hydrogenation reactions occur when electrons reduce protons to form atomic hydrogen and come together with the substrate. However, protons can also combine with electrons to form H_2. In this case, HER and hydrogenation reactions compete with each other [117]. The reduction process can be facilitated by combining electrons and protons. In this case, both species act as the reducing agent. Dai et al. investigated the reduction of nitrobenzene to azoxy and azobenzene molecules in the presence of graphitic carbon nitride (g-CN) as the photocatalysts. Mechanistic studies revealed that protons cleaved from isopropanol (IPA), used as the hydrogen source, combined with photogenerated electrons to form adsorbed hydrogen species (H_{ads}). Subsequently, the combination of H_{ads} with photogenerated electrons led to the formation of azoxy and azoaromatic

compounds [118].

Many complex processes and parameters influence the performance of hydrogenation reactions. Among these, one of the most fundamental is the relationship between the metal catalyst and the substrate, as per the Sabatier principle. This principle ensures efficient catalytic activity by balancing adsorption strength between the metal catalyst and the substrate molecule or atom. This optimal binding affinity is essential for several reasons. Firstly, if the metal catalyst binds too strongly to the substrate, it can hinder the activation of the molecule. Secondly, if the binding is sufficiently strong, the substrate will remain attached to the catalyst long enough for the reaction to occur [119]. D-band theory was proposed by Norskov in 1995 to elucidate the catalytic activity of metals [120]. According to the d-band theory, the catalytic activity of the metal is closely related to it's electronic properties, precisely the characteristics of their d orbital. The d orbitals interact with the s or p orbitals of the substrate, forming a hybridized state that determines the strength of the metal-substrate interaction. This theory suggests that the metal's d-band center position relative to the Fermi level is a critical factor in determining its catalytic activity. A higher d-band center, indicated by an upward shift relative to the fermi level, signifies a stronger interaction with the adsorbate, leading to a decreasing filling of the antibonding state of the adsorbate and promoting catalytic activity. Conversely, a shifting downwards away from the Fermi level, an increased filling of the antibonding states, suggests a weaker interaction between the metal and the substrate [121; 122]. In light of this information, the distance of metals' d-band centers from the Fermi level and parameters such as the filling status of bonding and antibonding levels in hybridization with different substrates will vary for each metal. Therefore, metals are expected to exhibit different activities or selectivities in catalytic reactions.

1.7.1.Nitrobenzene reduction reactions

The reduction reactions of nitrobenzene compounds hold considerable importance in organic chemistry as they transform into valuable products such as azoxybenzene, azobenzene, and aniline. These compounds have a wide range of applications in various industrial fields. For example, azoxybenzene, azobenzene with attractive orange color are

commonly used dye production. These colorful compounds find application in the textile industry, as well as in the plastic and rubber industries. One particular application of the reduction reactions of nitrobenzene compounds is in the pharmaceutical industry, where aniline, a product of the reduction of nitrobenzene, serves as a key intermediate in the synthesis of numerous pharmaceuticals. Aniline and its derivatives produce paracetamol, various antibiotics, and anticancer agents [123]. The versatility of these compounds makes them indispensable in developing new pharmaceutical products. An example of the use of anilines in the pharmaceutical industry is exemplified by the synthesis of sütezolid, an antibiotic used to treat tuberculosis. Sutezolid is synthesized from the relevant nitro compound which undergoes to hydrogenation in the presence of a catalyst to yield the aniline compound [124]. Furthermore, the reduction reactions of nitrobenzene compounds have also found applications in the agrochemical industry, where they are utilized in synthesizing pesticides and herbicides. By converting nitrobenzene compounds into various intermediates, chemists can create molecules that specifically target pests and unwanted plants, thereby contributing to developing effective agricultural products [123]. To conclude, the reduction reactions of nitrobenzenes continue to be a focal point of interest for researchers due to their role in synthesizing compounds used in diverse and important industrial applications.

The hydrogenation of nitrobenzene compounds is generally more straightforward than other organic groups' hydrogenation [125]. However, a complete understanding of the hydrogenation mechanism has yet to be fully achieved. Numerous studies in the literature explain the hydrogenation mechanism of nitrobenzene(NB). Among these, the primary one proposed by Haber et al. in 1898, as illustrated in the **Figure 1.13**, known as the Haber mechanism, is widely accepted in subsequent mechanistic studies or subject to debate due to its shortcomings. The Haber mechanism explains the presence of several intermediate products that could form during the reduction of NB to aniline [126]. The hydrogenation mechanism of nitrobenzene involves several intermediate steps. These intermediates include Nitrosobenzene(NSB) and Phenylhydroxylamine(PHA), which form during the reduction of nitrobenzene to aniline. The reduction of NB to aniline can

occur via direct and indirect pathways. In the direct path, NB is first reduced to NSB which then undergoes further reduction to form PHA. From PHA aniline is formed through a subsequent reduction step. The indirect pathway involves the formation of Azoxybenzene(AOB), Azobenzene(AZB), and Hydrazobenzene(HAB) as intermediates through the condensation of NSB and PHA before eventually converting into aniline. The Jackson mechanism, as studied by Gelder et al., proposes a novel hypothesis regarding the reduction of NB to aniline. According to their findings, Gelder et al.suggest that NSB (nitrosobenzene) is not an intermediate in the reduction of NB, as previously believed. The proposed pathway indicates that the rate of aniline formation through this mechanism is significantly low, further supporting the idea that NSB is not an intermediate in the reduction of NB. They propose that the initial product of NB reduction is PHA, which then reacts with adsorbed hydrogen to form phenylamine, and finally aniline. However, this mechanism also needs more evidence to explain the addition of four hydrogen atoms to nitrobenzene in a single step [127].

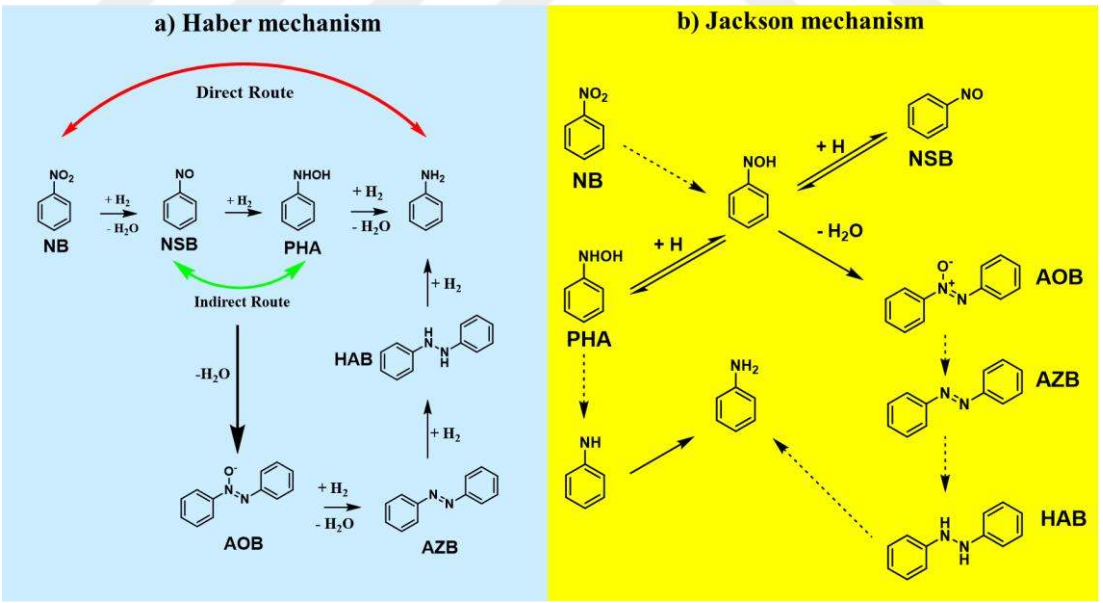

Figure 1.13.a) Haber mechanism, b) Jackson mechanism for nitrobenzene hydrogenation

Wisniak et al. studied the liquid-phase hydrogenation of nitrobenzene in the presence of a Raney nickel catalyst. To understand the mechanism, they performed a

series of experiments and concluded that the simple mechanism proposed in the Haber mechanism is invalid. They suggested that the actual mechanism is much more complex and that the events occurring on the catalyst surface directly influence it [128]. Höller et al. investigated the hydrogenation reaction of NB using Pt and Pd-supported catalysts. This study shows nitrobenzene was directly reduced to aniline without other products when using the Pd-supported catalyst. However, when using the Pt-supported catalyst, they observed the formation of NSB, PHA, AOB, and AZB but did not detect the presence of aniline. They indicated that the proposed mechanism for this reaction is consistent with the Haber mechanism. They conducted kinetic studies to validate their proposed mechanism by measuring reaction rates. They attempted to explain the reaction of nitrobenzene with hydrogen gas according to the Eley-Riedal mechanism [129]. Makaryan et al. achieved a highly intriguing result in the hydrogenation of nitrobenzene using carbon-supported Ir, Pd, and Pt catalystsThey explained the catalytic conversion of nitrobenzene to aniline and the conversion of PHA to aniline through experiments involving hydrogen and inert gas, thereby proposing an alternative mechanism. They concluded that it differed from the Haber mechanism, suggesting that the conversion of PHA to aniline is not due to hydrogenation but rather to disproportionation in PHA [130]. The literature continuously expands with new studies aiming to elucidate the hydrogenation of nitrobenzene to aniline, with each study attempting to address the shortcomings or inaccuracies of previously proposed mechanisms and striving to enhance understanding. All these endeavors collectively highlight the complexity introduced by the multitude of intermediate products formed during the reduction of nitrobenzene to aniline. The mechanism by which hydrogenation occurs remains a subject of debate amidst scientific community.

In recent years, the importance of selectivity in catalytic processes has gained recognition. By achieving high selectivity, catalysts can efficiently produce the desired product while minimizing the formation of unwanted by-products. This is crucial for reducing energy loss, saving time, and minimizing economic losses. Selective production of target products in the nitrobenzene reduction reactions can be challenging. The

presence of multiple intermediate compounds along the pathway from nitrobenzene to aniline can hinder the selective production of the desired product since halting the hydrogenation of nitrobenzene at an intermediate stage can be difficult. For example, catalysts supported by noble metals with high hydrogenation capabilities, such as Pt or Pd, may not stop at the intermediate stage and undergo over-hydrogenation, which leads to decreased selectivity. Therefore, developing catalysts that selectively produce the desired products is paramount. Reaction conditions play a crucial role in determining the selectivity of products in chemical reactions. For example, the parameters like pH, solvent selection, catalyst amount, catalyst loading, and light source can impact product selectivity. Wang et al. demonstrated chemoselective nitrobenzene hydrogenation using CQDs/$ZnIn_2S_4$ photocatalyst under visible-light irradiation by altering reaction conditions For instance, alkaline conditions promoted AZB selectivity, while changing the hydrogen source from ammonium formate to formic acid increased the selectivity towards aniline [131]. Nafiu et al. developed colloidal gold nanospheres (GNS) and gold nanoworms (GNW) heterogeneous catalysts and conducted a comparative hydrogenation of nitrobenzene compounds using sodium borohydride ($NaBH_4$) as the hydrogen source at 50°C. In this study, they achieved different conversion and selectivity results due to the shape differences of the two catalysts. They obtained higher aniline selectivity using the nanowire gold catalyst than its spherical counterpart. They attributed this effect to the increased surface area in GNW, promoting gold-hydride species, which facilitated the reduction of nitrobenzene [132]. In their study, Doherty et al. observed the impact of varying temperatures and solvent usage on product variation. They used the gold nanoparticle-supported phosphine-decorated polymer immobilized ionic liquids as a catalyst with $NaBH_4$ as the hydrogen source and observed varying product selectivity among PHA, AOB, and AZB. When ethanol was used as the solvent, they obtained AOB, while in experiments conducted at room temperature (RT) and in water, they obtained PHA. In experiments conducted in water at 60°C, they obtained Aniline [133].

Noble metals, such as Pt, Pd, Ru, and Rh, exhibit high activity in hydrogenation reactions. However, high activity does not guarantee the selectivity in the reduction

reactions of nitrobenzene. In most cases, increasing activity results in decreased selectivity. Therefore, achieving high activity while maintaining selectivity is crucial for obtaining valuable results in these reactions. The chemoselectivity of different metals may vary due to the different electronic properties of the metals. Each metal may exhibit different behaviors towards various functional groups, and this phenomenon, arising from differences in the intrinsic activity of the metal, is referred to as "intrinsic selectivity," which is unique to each metal [134]. The differences and the modifications of the geometric and electronic properties of active sites within metal nanoparticles determine the adsorption strength of the nitrobenzene molecule on the metal surface. This, in turn, influences the adsorption of the substrate onto the metal surface, elevating the chemoselectivity. To increase selectivity, the metal should incorporated into an appropriate support surface, and an appropriate interaction should be established between them following the Sabatier principle. Corma et al. investigated the activity of metals such as Au, Pt, Ru, and Ni in the reduction reaction of nitrobenzene. They observed the different activities of heterostructures formed by supporting different metals on TiO_2 using the reduction method with H_2. Additionally, they observed that the interaction between the metal and support also influenced the catalytic activity and selectivity [135].

1.7.2. The literature survey on nitrobenzene reduction reactions

Various methods are available for the hydrogenation of nitroaromatics, offering different advantages and limitations. Some commonly employed methods include thermal, electrocatalytic, and photocatalytic approaches. These methods differ in reaction conditions, catalyst types, and energy sources, providing researchers with a range of options based on their specific needs and objectives [127]. Applying photocatalytic processes in organic transformations has gained significant attention in recent years. This is mainly due to its numerous benefits, such as milder reaction conditions and selectively producing desired products. By utilizing photocatalysts, the reduction of nitrobenzene can occur under milder conditions compared to traditional methods. This not only improves the efficiency of the reaction but also reduces the environmental impact. Furthermore, by modifying the electronic band structure of the photocatalyst, it becomes possible to

maintain the chemoselectivity. This represents a notable advancement in green chemistry, enabling organic transformations to be conducted using sustainable and environmentally friendly methods. Overall, using photocatalysis in the hydrogenation of nitrobenzene offers a promising approach for organic transformation reactions. These reactions can be carried out with different types of photocatalysts; it can be a semiconductor that absorbs light or a dye-sensitized system that utilizes organic dyes to initiate the reaction.

The first study on the reduction of nitrobenzene compounds in the presence of a semiconductor was conducted by Mahdavi et al. They used a TiO_2 photocatalyst and irradiated with UV-light and ethanol was employed as the hydrogen source. In this study, they achieved 79% yield in converting 6-nitrocoumarin to 6-aminocoumarin [136]. Zhou et al. formed a Schottky junction structure by combining TiO_2 with Pd, Pt, Ru, and Rh metal nanoparticles to enhance the charge separation ability of TiO_2. In the photocatalytic reduction reaction experiment, glycerol was utilized as the hydrogen source along with UV-light as the light source. Among the catalysts obtained, Pd/TiO_2 demonstrated higher activity than structures formed with other metals, resulting in a 95% aniline selectivity at room temperature after an 18-hour reaction period. In the photocatalytic system, it was indicated that upon illumination, the electrons generated on TiO_2 are transferred to the Pd nanoparticles, which facilitate the reduction of nitrobenzene to aniline. The holes generated were used to oxidize glycerol to produce hydrogen, which was then employed in the hydrogenation of nitrobenzene compounds [137]. Xu et al. synthesized the Ce_2S_3/TiO_2 S-Scheme heterostructure via the solvothermal method and observed the activity in the photocatalytic hydrogenation of nitrobenzene under UV-light irradiation. The work functions of TiO_2 and Ce_2S_3 were calculated through DFT calculations and in-situ characterization techniques; it was stated that the difference in Fermi levels facilitated the transfer of electrons from Ce_2S_3 to TiO_2, leading to effective charge separation. TEOA was employed as a hole scavenger, and H_2O served as the hydrogen source in the photocatalytic hydrogenation of nitrobenzene experiment. The authors stated that there is competition between the experiments on H_2 evolution and hydrogenation. Then, in the presence of the catalyst, H_2 evolution did not occur. They attributed this to the rapid

utilization of reduced protons for hydrogenation before H_2 evolution took place. This study's significance lies in using water, the most neutral and green solvent, as a hydrogen source. Using water as a hydrogen source has significantly improved the conditions of hydrogenation reactions [138]. However, the wide band gap of TiO_2 necessitates working under UV light to initiate the reaction. By replacing TiO_2 with semiconductor materials with narrower band gaps and capable of absorbing visible light, the photocatalytic hydrogenation of nitrobenzene has shown promising results in subsequent studies.

Dai et al. investigated the photocatalytic reduction of nitroaromatics under visible light using g-CN as the photocatalystIn experiments where KOH as base and IPA was utilized as hydrogen source, the selectivity of the products formed can be influenced by variables such as light intensity and reaction duration. They also expanded their study by noting the reducibility of different nitrobenzene compounds under these reaction conditions. The obtained results showed the formation of aniline at low or even negligible levels, with variable main products being AOB and AZB. The metal-free nature of g-CN mainly prevents the formation of aniline, while it is noteworthy that the formation of AOB and AZB occurs when a strong base like KOH is used in the reaction medium [118]. Xu et. al synthesized CoP in situ on CdS nanowires They investigated the visible-light-induced reduction of nitroaromatics using the obtained CoP@CdS heterostructure and observed the high conversion of the substrate into aniline and AZB. In the experiments where ammonium formate (AF) was used as a hydrogen source, a decrease in H_2 production activity was observed in the presence of the substrate. The formation of AZB and aniline as a reaction outcome suggested that the mechanism proceeds via the condensation route. Moreover, they noted that conversion was not observed in the presence of TEMPO as an atomic hydrogen trapping agent, which indicated that nitrobenzene was reduced via atomic hydrogen rather than the evolved H_2 [139]. Bhar et al. synthesized a Ru-dye sensitized ZnO hybrid in the presence of a Pt cocatalyst, aiming to enhance the visible-light-induced photocatalytic reduction of 4-nitrophenol. The rationale behind using a Ru-dye-sensitized ZnO hybrid in this study is that the dye-sensitizer can effectively absorb visible light, which can then initiate the photocatalytic

reaction on the ZnO semiconductor surface. This hybrid system allows for efficient solar energy utilization and promotes the photocatalytic reduction of 4-nitrophenol [140].

Fu et al. modified CdS nanorods with (Au, Pt, Pd, Ru) noble metals using a one-pot solvothermal method. They observed the activity of these heterostructures in the photocatalytic reduction of nitrobenzene They investigated the effect of different reaction conditions on the target product in organic experiments where AF was used as the hydrogen source and ethanol as the solvent. The highest yield of aniline was obtained with Pd-modified co-catalyst on CdS, while aniline production with Au and Ru was nearly the same. However, the lowest yield of aniline was observed with the catalyst containing Pt. It is noted that in CdS/Pt, unlike the others, H_2 evolution occurred, indicating that the active H species derived from AF were not effectively utilized to reduce nitrobenzene [141]. Yin et al. constructed a SiO_2-Cu_2O@SiO_2 heterostructure by embedding transition metal oxide Cu_2O into hierarchically hollow SiO_2 spheres, and they observed the activity of the synthesized photocatalyst in the photocatalytic reduction of nitrobenzene where formic acid was used as the hydrogen sourceReasonable yields were obtained for several nitrobenzene derivatives in experiments. The researchers attributed the higher selectivity towards aniline to the confinement effect of the SiO_2-Cu_2O@SiO_2 heterostructure. The researchers noted that in the SiO_2-Cu_2O heterostructure, some atomic hydrogen is transferred to nitrobenzene while some form H_2 and leave the system. On the other hand, in the SiO_2-Cu_2O@SiO_2 heterostructure, due to the absence of H_2 evolution, the effectively utilized atomic hydrogen ensures chemoselectivity towards aniline [142]. Kumar et. al fabricated Ni nanoparticle-decorated phosphorus-doped graphitic carbon nitride (Ni@-PC_3N_4) heterostructure, known as Ni@-PC_3N_4, was investigated for its ability to catalyze the hydrogenation of various nitrobenzenes under visible-light irradiation in the presence of hydrazine monohydrate as the proton sourceThe researchers noted that the visible-light absorption of Ni@-PC_3N_4 was enhanced due to the introduction of phosphorus doping, and they identified Ni nanoparticles as electron traps in the heterostructure. They reported favorable yields for several substrates under the current reaction conditions [143].

All these studies demonstrate the reduction of nitrobenzenes under milder reaction conditions via photocatalytic routes, setting aside classical hydrogenation methods. It is observed that various hydrogen sources are employed to facilitate these reactions. Adding another advantage to the photocatalytic hydrogenation processes entails substituting these hydrogen sources with much greener, non-toxic, and cost-effective alternatives, such as water. At this point, only a few valuable studies are available on using water as the greenest hydrogen source in the photocatalytic hydrogenation of nitrobenzenes.

Han et al. investigated the photocatalytic hydrogenation of nitrobenzene and other organic groups by combining platinum (Pt) cocatalyst with carbon nitride (CN), determining its significant activity in hydrogenation reactions alongside its crucial role in water splitting (**Figure 1.14**). This study combined the photochemical hydrogen evolution with the transfer hydrogenation technique using the Pt/CN catalyst, which they named photocatalytic water-donating transfer hydrogenation (PWDTH), to emphasize using water as the hydrogen source. They stated that electrons generated in CN are transferred to Pt nanoparticles upon excitation by light, where holes are captured by TEOA.At the same time, H_2O is reduced to H on Pt NPs, facilitating the in-situ reduction of nitrobenzene and other unsaturated organic groups. They also confirmed water's role as a hydrogen source using isotope labeling experiment [144].

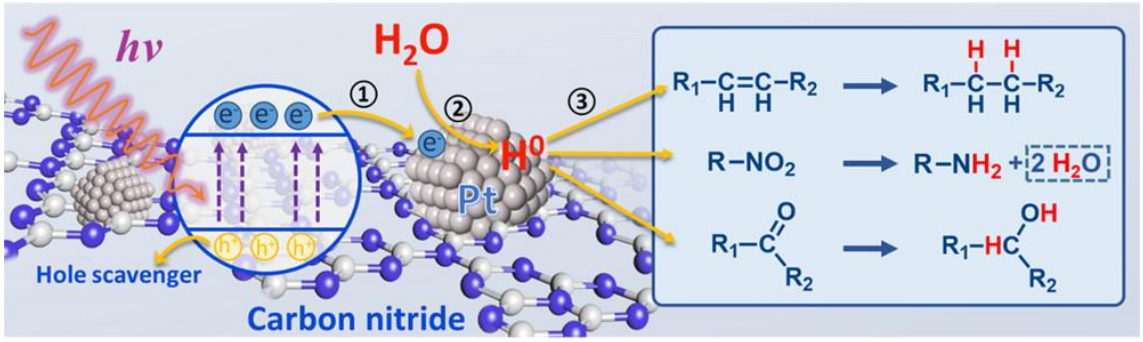

Figure 1.14. Proposed Process of PWDTH Using Pt/CN Photocatalyst. [144]

Zhang et al. synthesized surface hydroxylated graphitic carbon nitride (gCN-OH) and utilized it to perform a series of photocatalytic hydrogenative coupling reactions by

extracting hydrogen atoms from water. The authors proposed two potential mechanisms for the hydrogen atom transfer (HAT) reaction: it could proceed either through the utilization of molecular H_2 obtained from water splitting (**Fig. 1.15**, top), or via the partial dehydrogenation of water by breaking the O-H bond of water to produce H_2O_2 (**Fig. 1.15**, bottom), with the latter pathway being regarded as more feasible when employing gCN-OH. They observed the formation of H_2O_2 through UV-Vis spectroscopic analysis with $CuSO_4$-2,9-dimethyl-1,10-phenanthroline (DMP) solution. Subsequently, they demonstrated that these obtained H atoms reduced NB to NSB and PHA first, followed by further reduction to AOB in the presence of KOH [145].

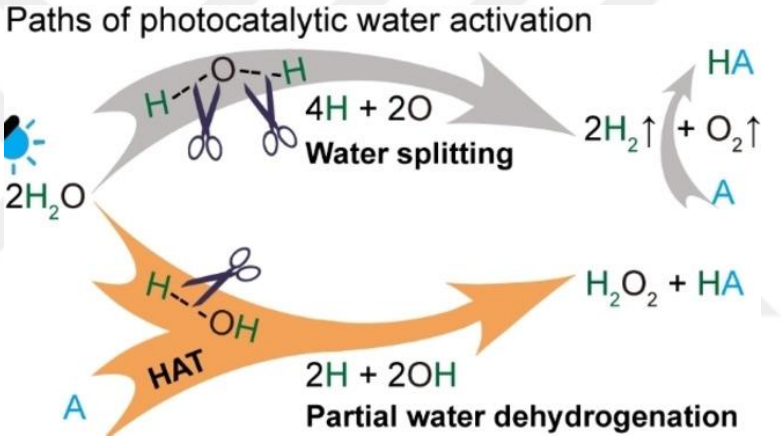

Figure 1.15. Proposed water activation pathways. [145]

Only these two significant studies highlight the considerable gap in the current literature on this subject. Research efforts focused on obtaining hydrogen from water and elucidating the intricate mechanisms involved in the process hold paramount importance in advancing transfer hydrogenation reactions in organic chemistry. Such endeavors have the potential to revolutionize the field by shedding light on challenging processes and facilitating the development of innovative methodologies in organic synthesis.

1.7.Objective and Summary of the thesis

This thesis focuses on utilizing photocatalytic processes to develop cheap, environmentally benign new photocatalytic systems, considering all the information presented in the context of sustainable clean energy. The developed semiconductor

materials will establish new hybrid structures capable of photocatalytic hydrogen evolution from water and utilizing hydrogen atoms obtained from water in photocatalytic transfer hydrogenation reactions. To achieve this goal, in the first section, starting from RP, RP/BP-Pt(PtP_2) structure was synthesized for the first time in the literature along with BP crystals in a single step in the presence of an appropriate solvent. Compared to RP and BP derivatives, the new heterostructure exhibited high activity in photocatalytic HER reactions. Subsequently, as a second application area, the same photocatalyst, RP/BP-Pt(PtP_2), aimed to reduce nitrobenzene compounds photocatalytically. The results showed that azoxybenzene compounds were obtained from various nitrobenzene compounds due to the absence of metallic Pt in this heterostructure. Deuterium labeling experiments confirmed that water used in the reaction environment acted as a hydrogen source. The idea that water can be used as a hydrogen source in transfer hydrogenation reactions is supported by only a few examples in the literature summary. Consequently, each step taken, every study conducted, and any new idea developed in this area will significantly advance our understanding of transfer hydrogenation processes.

In the subsequent section, Pt and Pd nanoparticles were synthesized in situ on RP. This novel method demonstrated that metal nanoparticles could be integrated into RP much more pratically and effectively than the previous approach. The photocatalytic HER activities of RP/Pt and RP/Pd were observed in the presence of TEOA and EY. Each exhibited higher activity than pristine RP, with RP/Pt showing the highest HER activity and RP/Pd exhibiting the lowest. Subsequently, the activity of these catalysts was observed in the photocatalytic water-donating transfer hydrogenation reactions (PWDTH) using nitrobenzene as the substrate. The conversion of various nitrobenzene derivatives to aniline derivatives and product selectivity values in PWDTH reactions were determined using GC-MS and NMR techniques. The highest activity was observed in the presence of the RP/Pd catalyst. Relationships between activities in HER and PWDTH reactions were discussed, and mechanisms were proposed. The structure of all obtained catalysts was elucidated using various characterization technique

Chapter 2:

MATERIALS AND METHODS

2.1. Chemicals

Red phosphorus (≥97%, AR grade, Sigma-Aldrich), ethylenediamine (≥99.9%, Sigma-Aldrich), dimethylformamide (≥99.9 Isolab), ethanol absolute (≥99.9%, IsoLab), methanol (≥99.7, Honeywell Riedel-de Haën), ethyl acetate (,≥99.5%, Isolab) hexachloroplatinic acid hexahydrate ($H_2PtCl_6.6H_2O$, ≥37.50% ,Ar grade, Sigma-Aldrich), potassium tetrachloropalladate(II) (K_2PdCl_4, ≥99.99% Sigma-Aldrich), triethanolamine (TEOA ≥99.0%, Sigma-Aldrich), Eosin Y (Sigma-Aldrich), sodium hydroxide (NaOH %99, Isolab), borane-ammonia complex (H_3NBH_3, ≥90%, Sigma-Aldrich), sodium borohydride ($NaBH_4$, Sigma-Aldrich), 2,2,6,6-Tetramethylpiperidine 1-oxyl (TEMPO) (98%, Sigma-Aldrich), 1,4-benzoquinone (BQ), potassium iodide (KI, ≥99), deionized water (DIW, 0.055 $\mu S.cm^{-1}$), deuterium oxide (D_2O, 99.8%, Sigma-Aldrich), hydrogen peroxide (H_2O_2, 30% in water, Sigma-Aldrich) nitrobenzene derivatives(Alfa Aesar and Sigma-Aldrich). All chemicals were utilized without undergoing additional purification.

2.2. RP/BP-Pt+PtP_2 synthesis

RP/BP-Pt+PtP_2 was prepared using a one-pot solvothermal synthesis technique (**Figure 2.1**). In a typical synthesis procedure, 100 mg of RP was dispersed in 40 ml of ethylenediamine (EDA) and 20 ml of dimethylformamide (DMF) using ultrasonication for 1 hour. Subsequently, a specified amount of $H_2PtCl_6.6H_2O$ solution, serving as the Pt precursor, was added to the mixture, followed by an additional hour of sonication. The resulting mixture was transferred to a Teflon-lined stainless steel-autoclave and heated at 180°C for 10 hours. After cooling to room temperature, the product was separated from the solution by centrifugation using ethanol at 12000 rpm and dried in a vacuum oven at 50°C.

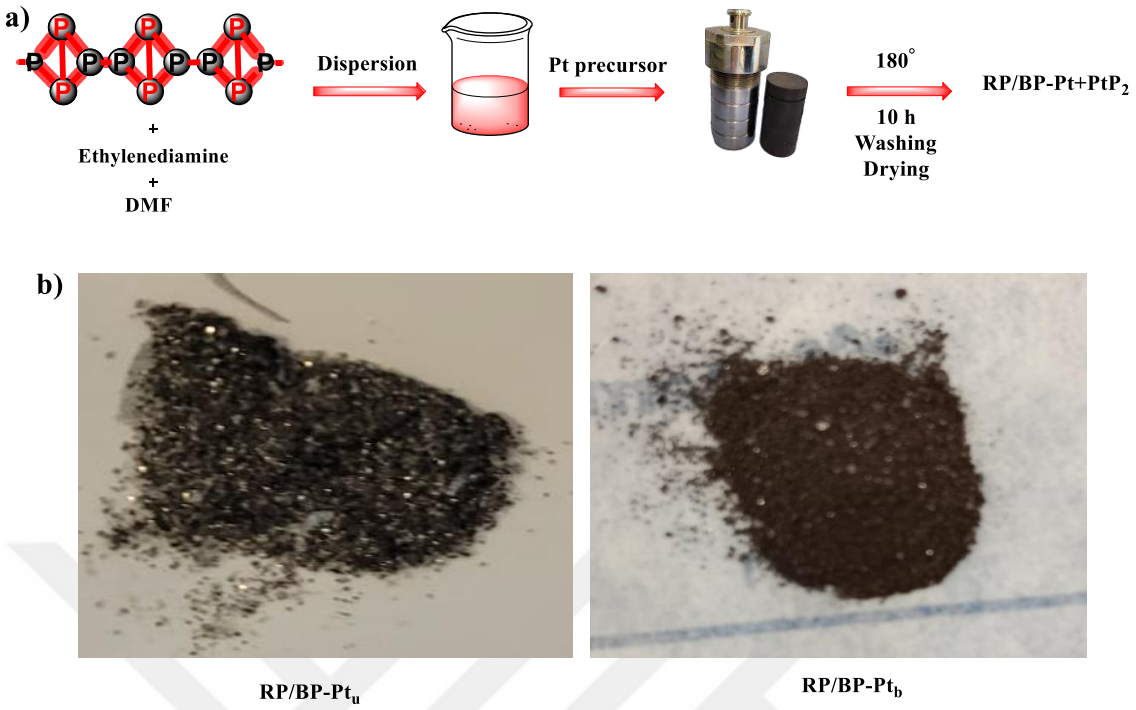

Figure 2.1. Schematic illustration of the RP/BP-Pt + PtP_2 synthesis synthesis procedure, a)Synthesis procedure, b)Synthesized materials.

2.3. RP/Pt synthesis

100 mg of RP was dispersed in 20 ml of ethanol using an ultrasonic bath for 4 hours. H_2PtCl_6 was weighed and dispersed in water to prepare a stock solution. A certain amount of Pt from the stock solution was added to the RP mixture. The mixture was subjected to another hour of sonication and then left for overnight stirring. In the end, two mmol of AB were dissolved in 2 ml of water and added to the RP mixture to reduce Pt(IV) ions (**Figure 2.2**). After centrifugation with ethanol for washing, the material was dried in a vacuum oven at 50°C.

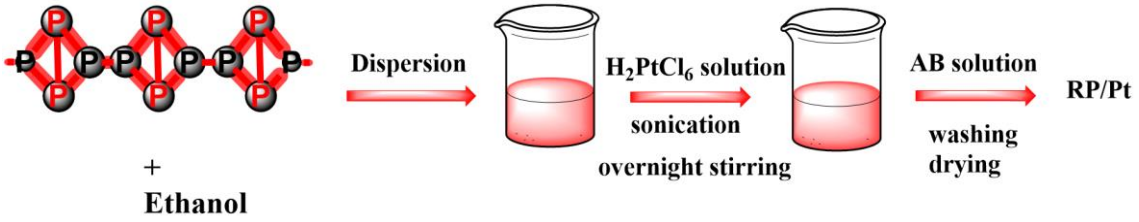

Figure 2.2. Schematic illustration of the RP/Pt synthesis procedure.

2.4. RP/Pd synthesis

100 mg of RP was dispersed in 20 ml of ethanol in the ultrasonic bath for 4 hours. K_2PdCl_4 was weighed dispersed in water to prepare a stock solution. A certain amount of Pd from the stock solution was added to the RP mixture. Following an additional hour of sonication, the mixture was left for overnight stirring. Finally, two mmol of NaBH4 were dissolved in 2 ml of water and added to the RP mixture to reduce Pd(II) ions (**Figure 2.3**). After centrifugation with ethanol for washing, the material was dried in a vacuum oven at 50°C.

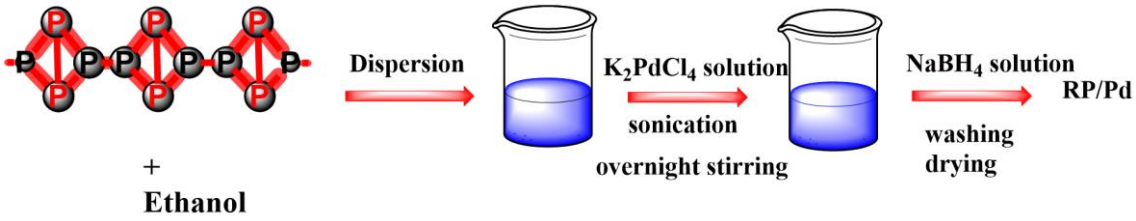

Figure 2.3. Schematic illustration of the RP/Pd synthesis procedure.

2.5. Photocatalytic Hydrogen Evolution Experiments

Photocatalytic HER experiments were conducted in a quartz reaction cell.(**Figure 2.4a**) The cell contained RP/BP-Pt catalyst powder and EY dye dissolved in a sacrificial agent (5% TEOA, pH = 9). All procedures were carried out in a N_2-filled glove box to maintain an inert atmosphere. Prior to the HER tests, the mixture was sonicated to ensure uniformity. Visible light illumination (λ>420 nm) was achieved using a 300 W Xe lamp with a cut-off filter. The mixture was stirred continuously during the photocatalytic reaction, and the amount of H_2 produced in the headspace of the vessel was measured using gas chromatography (Shimadzu GC-2014 with a thermal conductivity detector (TCD), with Ar serving as the carrier gas).

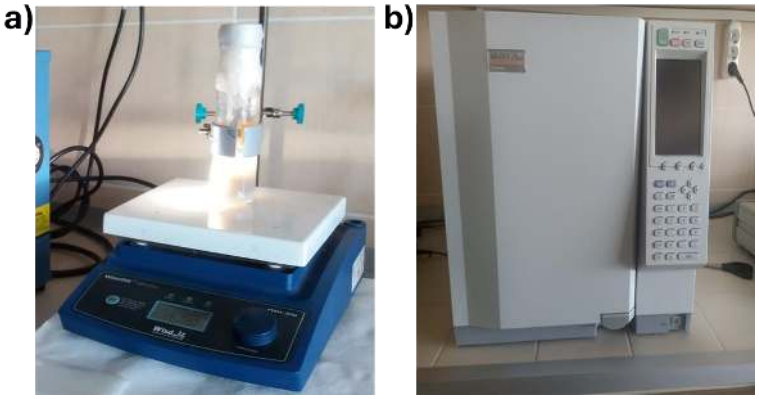

Figure 2.4. Photocatalytic HER set-up a) Reactor system under visible light irradiation, b) GC equipment.

2.6. Tandem Photocatalytic Hydrogen Evolution and Hydrogenation of Nitroarenes

2.6.1. Photocatalytic nitrobenzene reduction reactions in the presence of RP/BP-Pt+PtP$_2$ photocatalyst

In this process, all the necessary components for the reduction of nitrobenzene and the photocatalytic production of hydrogen are combined in a single reaction vessel, and the reaction proceeds accordingly. Following the dispersion of 10 mg of catalyst in water, the reactor was loaded with 0.25 mmol of nitrobenzene derivative dissolved in 3 ml of MeOH. Subsequently, NaOH (5 M), TEOA solution (5%), and EY dye solution (3.25×10^{-4} M) were introduced into the reactor. Utilizing a self-cooling white LED light source (24 W, **Fig 2.5a**), the reaction proceeded at ambient temperature for 8 hours. Upon completion of the reaction, the mixture underwent washing with ethyl acetate and water, followed by separation of the organic phase. The organic fraction was then prepared for GC-MS and NMR analysis.

2.6.2. Photocatalytic nitrobenzene reduction reactions in the presence of RP/Pt and RP/Pd photocatalysts

The catalyst (10 mg) was dispersed in water. Then, 0.25 mmol of a nitrobenzene derivative was added to the reactor and dissolved in methanol. Subsequently, TEOA, EY, and the catalyst were added to the reactor, and the reaction was initiated at room temperature under 150 W white light (**Fig.2.5b**) for 8 hours. After the reaction, the mixture was subjected to work-up with ethyl acetate and water, followed by organic phase

separation. The organic phase was then prepared for the further analysis to determine the conversion and selectivity data. The conversion values of nitrobenzene were calculated using GC-MS and NMR in the presence of an appropriate internal standard, 1,3-dinitrobenzene. At the end of the reaction, an internal standard was added equal to the initial substrate quantity, and the mixture was prepared for GC-MS or NMR analysis. The conversion percentages were determined by considering the areas under the peaks corresponding to equal amounts of substrate and internal standard. The selectivity value represents the selectivity for the target product aniline while indicating the presence of by-products formed during the conversion of nitrobenzene. The selectivity values were calculated using GC-MS.

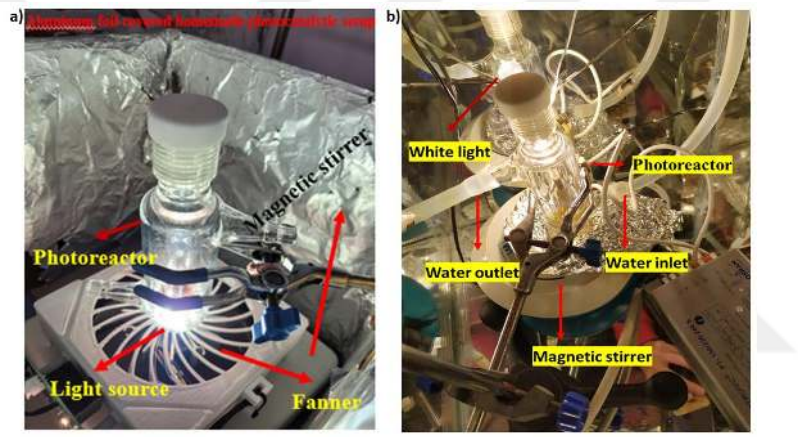

Figure 2.5. Homemade photocatalytic setup a)25 W white LED system. b) 150 W white light.

2.7. Reusability Experiments

Reusability tests of the catalysts were conducted in the presence of nitrobenzene experiments. For this purpose, experiments were performed using 40 mg of catalyst to prevent catalyst loss, differing from the standard reaction conditions. Other parameters remained the same as those in the standard conditions, with the catalyst carefully separated from the reaction medium after each experiment and prepared for the next experiment. Three reusability experiments were conducted, and at the experiment's end, the catalyst's structure was observed using XRD and XPS.

2.8. Hydrogen Peroxide Detection Experiment

The H_2O_2 formation reaction was carried out under white light irradiation in the photoreactor. After dispersing 20 mg of catalyst in 20 ml of DIW, the hole scavenger TEOA was added, and then the mixture was transferred into the reactor. After taking 3 ml of the initial solution before turning on the light, the solution was passed through a 0.22 µm syringe filter, and 0.1 ml of 0.4 M KI and 0.1 ml of 0.1 M HCl were added. After waiting for 4 minutes, triiodide (I_3-) with an absorption peak at approximately 350 nm was observed using UV-Vis spectrophotometry, indicating the existence of H_2O_2. The process continued for time intervals of (5-10-15-20) minutes, and at the end of each specified time interval, the process was repeated, and I_3^- was observed from the UV-Vis spectrophotometer absorbance graph.

$$H_2O_{2(aq)} + 3I^-_{(aq)} + 2H^+ \rightarrow I_3{}^-_{(aq)} + H_2O \quad (2.1)$$

2.9. Instrumentation

X-ray diffraction patterns(XRD) were obtained using a Bruker D8 Advance X-ray diffractometer equipped with Cu K alpha radiation (λ = 1.54 Å). ICP-MS analysis was performed using an Agilent 7700x Inductively Coupled Plasma-Mass Spectrometer. Photoluminescence spectroscopy (PL) data was collected using the Agilent Cary Eclipse PL instrument with excitation at 320 nm. Time-resolved photoluminescence spectroscopy (TRPL) data was acquired using the Edinburgh Instruments FLS1000 spectrometer with a 377 nm laser source. UV-Vis spectra were acquired using the Shimadzu UV-3600 UV-Vis-NIR spectrophotometer. The Kubelka-Munk equation with UV-Vis spectroscopy converted reflectance data to absorbance data. Transmission electron microscope (TEM), scanning TEM high-angle annular dark field (STEM-HAADF) images, and elemental mappings were captured using the Hitachi HT7800 TEM instrument in high-resolution mode at 120 kV. Additionally, high-resolution transmission electron microscope images(HR-TEM) were obtained with the Hitachi HF5000 TEM instrument in high-resolution mode at 200 kV. Scanning electron microscopy(SEM) images were acquired using the Zeiss Ultra Plus Field Emission Scanning Electron Microscope. The surface chemistry of the structure was analyzed using the Thermo Scientific Kα X-ray photoelectron spectrometer(XPS), equipped with an aluminum anode (Al Kα, 1468.3 eV).

Mott-Schottky analysis was performed using the CHI 660E electrochemical workstation, with an Ag/AgCl reference electrode, a Pt wire counter electrode, and a Na_2SO_4 solution (0.1 M, pH = 6.05) as the electrolyte. Fourier-transform infrared spectroscopy (FT-IR) analysis was performed using the Thermo Scientific iS10 FT-IR spectrophotometer. NMR analyses were conducted using a 500 MHz Ascend Neo spectrometer with $CdCl_3$ as the solvent and tetramethylsilane (TMS) as the internal standard. GC-MS spectroscopy was carried out using a Shimadzu GCMS-QP2010 SE instrument with a Shimadzu Rtx-t column (0.25 mm × 30 m, 0.25 µm).

2.10. Characterization techniques

X-ray Diffraction (XRD)

X-ray diffraction analysis is a powerful technique used to investigate the crystal structure of materials. This technique provides valuable information about the arrangement of atoms within a crystal. XRD analysis is specific to each substance as it produces unique diffraction lines. Moreover, XRD analysis is a non-destructive technique, meaning the sample is not altered after the analysis. XRD analysis is based on the principle of constructive interference of X-rays scattered at specific angles from crystal lattice planes within a sample. Once the X-rays interact with the crystal lattice, they undergo diffraction, resulting in a pattern of scattered beams. These scattered beams are then detected and analyzed to determine the crystal structure and composition of the material. The XRD technique utilizes a specialized instrument called a diffractometer, which directs a monochromatic X-ray beam onto the sample. The diffractometer collects the scattered X-rays and produces a diffraction pattern. The distinct peaks observed in the diffraction pattern serve as a distinctive identifier for each material, These peaks enable the identification of the crystal structure present in the sample. Bragg's equation plays a pivotal role in this determination. It allows for calculating the spacing between crystal lattice planes, d, and the angles at which the X-rays were scattered, θ. This information allows for determining the crystal structure, including parameters such as unit cell dimensions and atomic positions. Materials without a regular atomic arrangement, such as amorphous structures, liquids, and glasses, do not reflect X-ray beams [146].

$$n\lambda = 2dsin\theta \tag{2.2}$$

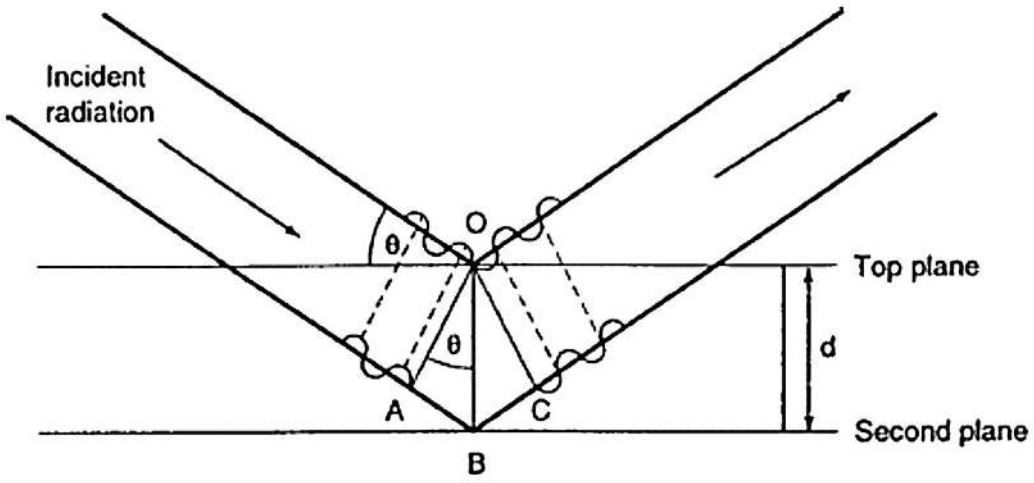

Figure 2.6. Representation of diffracted light from two crystal planes.[132]

Scanning Electron Microscopy(SEM)

SEM is a technique used to provide microscopic insights into the size, shape, crystallographic structure, and chemical or physical properties of a material's surface. It involves scanning the surface of a material with a focused electron beam generated from an electron source. When the electron beam interacts with the surface, it produces Auger electrons, secondary electrons, and backscattered electrons, along with X-rays. Secondary electrons have less energy than backscattered electrons. While secondary electrons typically provide information about surface features, backscattered electrons enable the visualization of structures with different phases in contrasting shades. These electron signals are collected, processed through various detectors, and usually recorded in computer memory using an Everhart-Thornley secondary electron detector (sensitive to both secondary and backscattered electrons) and displayed on a screen. The resulting images offer insights into the surface properties of the sample, including its morphology, texture, and roughness [147].

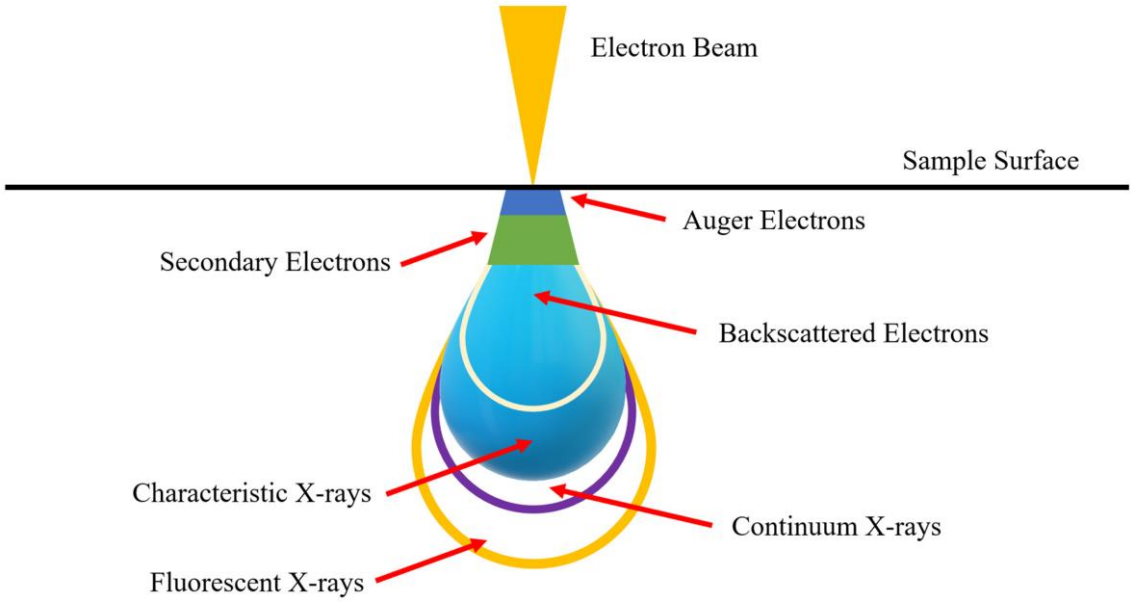

Figure 2.7. The interaction between the electron beam and the sample surface. [134]

Transmission Electron Microscopy(TEM)

TEM is an effective microscopic technique used for visualizing materials at the nanoscale, which cannot be achieved by light microscopy. TEM consists of several components, including an electron gun that generates an high-voltage electron beam, a condenser lens that directs the electron beam onto the sample, a series of lenses that magnify the transmitted electrons through the specimen and forms the image on the fluorescent screen [148]. The most necessary aspect of sample preparation for TEM analysis is ensuring the sample is thin. This is essential for allowing electrons to pass through the sample smoothly. Thick samples can cause electron scattering, leading to the formation of distorted images. Therefore, specimens should be prepared to a thickness of less than 100 nm for standard TEM analysis to ensure that electrons can pass through without significant scattering, allowing for clear imaging. TEM images consist of different views, namely bright field and dark field, providing information about the morphological structure and crystalline state of the material. In bright field images, heavy atoms appear dark, whereas in dark field images, heavy atoms appear light. In bright field images, regions where electrons are transmitted appear brighter, while regions where electrons are scattered or absorbed appear darker. In dark field images, regions where electrons are transmitted appear black, while scattered electron areas appear light.

Scanning Transmission Electron Microscopy (STEM) analysis provides information about the distribution of elements within a material. For HR-TEM analysis, where higher resolution images are desired, the specimen thickness should be even thinner, ideally below 50 nm [149]. TEMs typically operate within the 100-300 keV range, which allows for sufficient resolution and penetration depth. However, in cases where even higher resolution is needed, High-resolution Transmission Electron Microscopy(HR-TEM) can be employed. HR-TEM allows operation at higher voltages, typically between 200-400 kV. This provides better resolution and deeper penetration depth, making it ideal for studying complex structures.

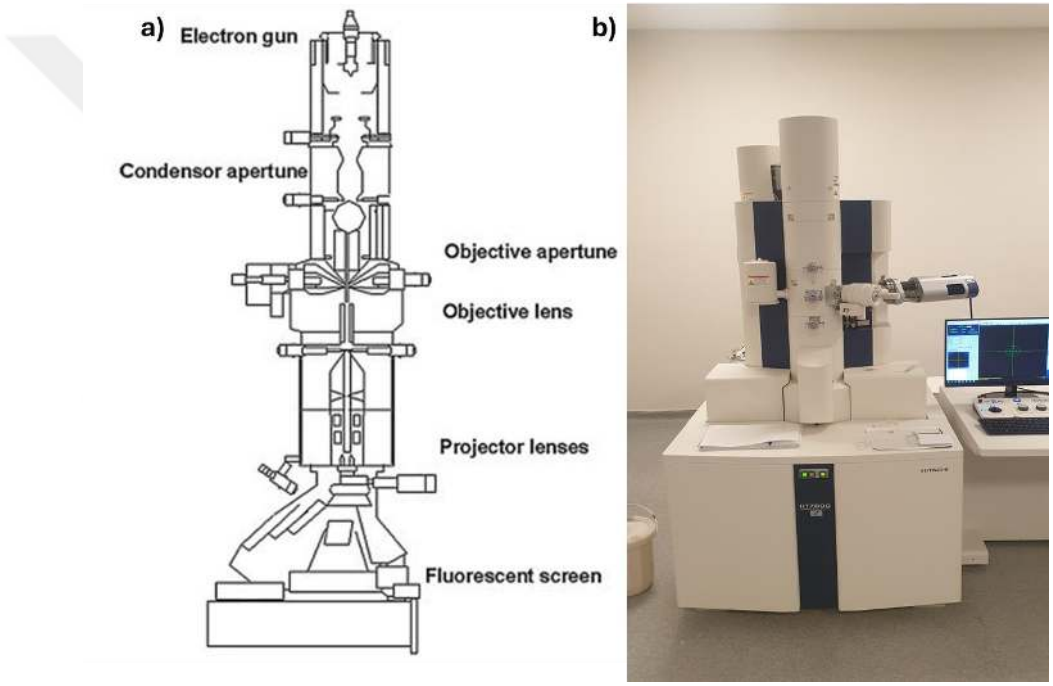

Figure 2.8. a)TEM components [135], b) TEM Column at Koç University Hospital.

X-Ray Photoelectron Spectroscopy (XPS)

X-ray Photoelectron Spectroscopy (XPS) is an essential technique for understanding the chemistry of a material's surface. It works by irradiating the material's surface with X-ray beams and then evaluating the energy of the emitted electrons. XPS generally consists of Al or Kα sources. When these X-rays hit the surface, they knock off electrons from the outermost layers of atoms in the material. Because the mean free path of electrons in solids is relatively small, the detected electrons come from only a few layers

close to the surface[150]. This makes XPS a surface-sensitive technique. The working principle of XPS, based on the Photoelectric Effect discovered by Heinrich Hertz in 1887 and further developed by Albert Einstein, who was awarded the Nobel Prize for his contributions, involves using X-ray radiation to eject electrons from the surface of a material. These ejected electrons' kinetic energy is then measured (**Eq. 1.8** where hν is the photon energy BE is the binding energy, φs is the work function of the spectrophotometer) providing information about the material's chemical characteristics. The kinetic energy of these ejected electrons is measured using **Eq 2.3**, where hν represents the photon energy, BE is the binding energy, and φ_S is the work function of the spectrophotometer, KE is the emitted electron's kinetic energy. Each element scanned with XPS reflects a unique Binding Energy (BE), except for hydrogen and helium. XPS can detect all elements except hydrogen and helium. Depth profiling in XPS involves using a sputtering source, often with argon (Ar) ions, to gradually remove material from the surface of the sample layer by layer.

$$E_{BE} = h\nu - E_{KE} - \varphi_s \tag{2.3}$$

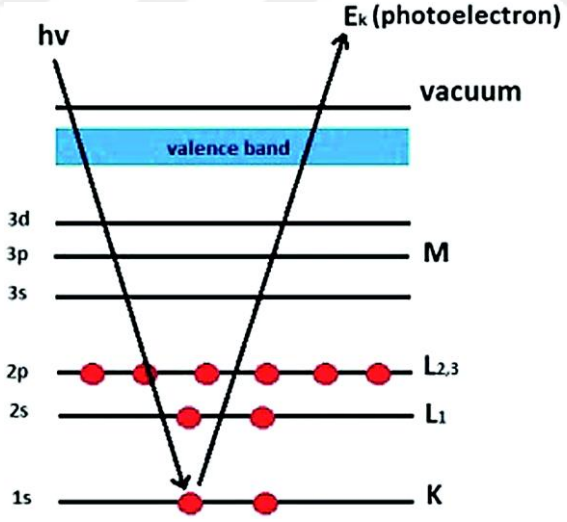

Figure 2.9. Schematic illustration of the photoelectric effect. [151]

UV-Vis-NIR diffuse reflectance spectroscopy (UV-Vis-DRS)

UV-Vis-DRS spectroscopy is a technique used to obtain information about the optical properties of powdered or solid materials. When UV-Vis radiation hits a surface,

two types of radiation are reflected from the surface. On smooth surfaces, radiation reflected at the same angle as the incident angle results in regular reflectance, whereas on rough, non-homogeneous surfaces, UV-Vis radiation undergoes multiple scattering, leading to diffuse reflectance [152]. Reflectance data is converted to absorbance data using the Kubelka-Munk equation as illustrated in **Eq. 2.4**; where K and S are absorption and scattering coefficients, R_∞ is the reflectance of a thick layer. The band gap value of semiconductor materials is a significant parameter for assessing their light-harvesting capabilities. The Tauc plot equation based on absorbance values obtained using the Kubelka-Munk equation, is used to draw a curve that provides the band gap of the semiconductor material. **Eq. 2.5** shows the Tauc plot equation where a is the absorption coefficient, h is the Planck constant, v is the frequency of the photon, B is constant and Eg is the bandgap of the semiconductor.
The value of $1/\gamma$ varies depending on whether the semiconductor has a direct or indirect bandgap. For materials with a direct bandgap, γ is typically 2, whereas for indirect bandgap semiconductors, γ is equals to 1/2. The point at which the Tauc plot curve intersects the X-axis indicates the band gap value of the semiconductor [153].

$$F(R_\infty) = \frac{K}{S} = \frac{(1-R_\infty)^2}{2R_\infty} \tag{2.4}$$

$$(ahv)^{1/\gamma} = B(hv - E_g) \tag{2.5}$$

Photoluminescence Spectroscopy(PL)

The luminescence process involves the excitation of electrons from the ground state to the excited state, followed by the emission of a photon as they relax and return to the ground state. The photoluminescence (PL) process, which involves exciting a semiconductor material with a light source, begins with the transition of electrons in the valence band (VB) to the conduction band (CB) when excited by light with higher energy than the semiconductor's band gap. Holes are created in the VB. The excited electrons in the CB then release their energy as heat, returning to the conduction band minimum (CBM). Subsequently, electrons are released from the CB minimum to the VB maximum, resulting in radiative recombination, where photons are emitted. Radiative recombination,

emitted in the form of photon emission, occurs through two different mechanisms: intrinsic emission (band-to-band), which denotes radiative recombination directly from the CB to the VB, and extrinsic emission (sub-band gap), which occurs when an electron in the CB is captured by defects or impurities. PL spectroscopy investigates the charge carrier behavior of semiconductor materials, providing insights into their optical properties [154].

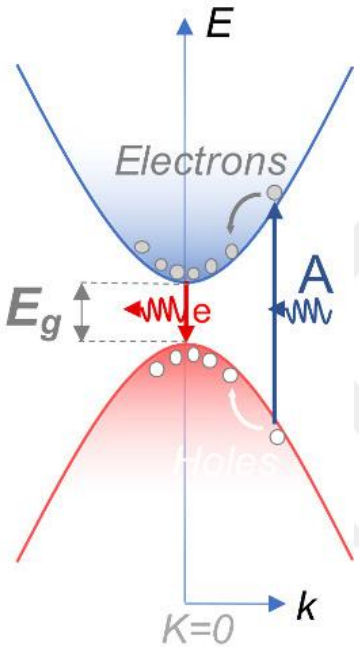

Figure 2.10. PL process for a semiconductor direct-band gap material. [154]

Time-Resolved Photoluminescence Spectroscopy (TRPL)

TRPL spectroscopy is a technique based on measuring the photoluminescence emission of a semiconductor over time. The apparatus typically includes a laser light source, a spectrograph, and a detector such as a CCD camera. The lifetime of a molecule's lowest excited singlet state can be measured from picoseconds to microseconds. Various parameters can influence the lifetime of a semiconductor material. Processes such as adding elements, atoms, or ions to the semiconductor, interactions with other semiconductors, or introducing metal into the structure can all cause changes in the lifetime.

Inductively Coupled Plasma Mass Spectroscopy (ICP-MS)

ICP-MS (Inductively Coupled Plasma Mass Spectrometry) is a technique that provides information about the concentration of elements constituting a material. It can detect the quantity of many elements from the periodic table, even at low concentrations, from ppm to ppb. While highly effective, it has some limitations. Elements with low molecular weights or those that cannot ionize within the plasma cannot be detected using this method, such as H, He, Ne, Ar, CO, N, F, etc. In ICP-MS, atoms in the sample are ionized using inductively coupled plasma. Calibration curves are constructed using reference standards containing various elements, and the concentrations of elements in the sample are determined by matching them to the calibration curves. Samples are placed in an appropriate acid to decompose into a gaseous form within the plasma and prevent solid particles from contaminating the device. Samples containing particulate matter are prepared using the microwave digestion technique.

Gas Chromatography-mass spectrometry (GC-MS) analysis

GC/MS (Gas Chromatography/Mass Spectrometry) is a powerful analytical technique that combines the principles of gas chromatography and mass spectrometry and overcomes limitations encountered when using each technique individually for sample identification. GC/MS is widely used in various fields such as environmental analysis, forensic science, pharmaceuticals, airports, criminal investigations, anti-doping testing in sports, etc. It allows for the detection of different substances within a sample. GC separates organic compounds into their components based on retention times on a column, while MS ionizes and fragments each molecule, allowing for detection based on mass-to-charge ratio [155].

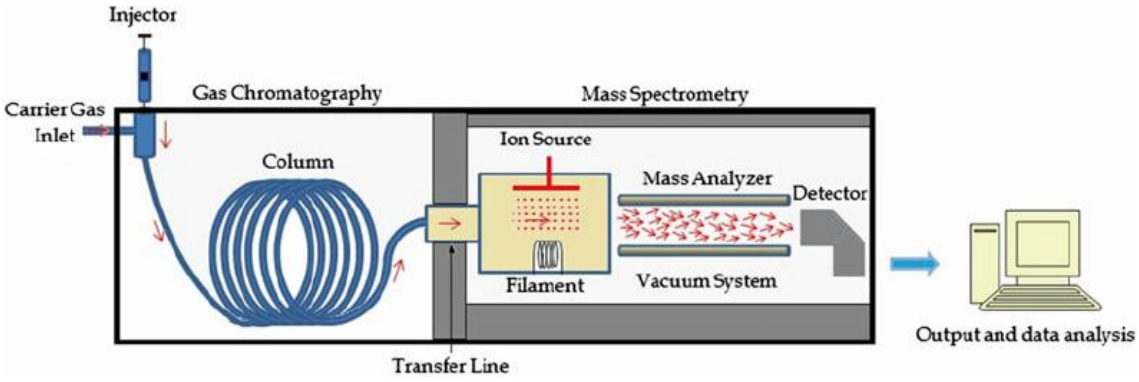

Figure 2.11. GC-MS equipment. [156]

Nuclear Magnetic Resonance Spectroscopy(NMR)

NMR is one of the most important and comprehensive spectroscopic techniques used for elucidating the structures of organic molecules. The technique is based on the absorption of Radiofrequency by atomic nuclei placed within a strong magnetic field. However, not every atomic nucleus yields an NMR spectrum. Nuclei that give rise to an NMR spectrum are called NMR-active nuclei. If a nucleus has an even number of protons and neutrons, the nucleus does not exhibit a net overall rotation, and the spin quantum number is l=0. Such elements are not NMR-active. For an element to be NMR-active, l must be greater than 0. If the atomic mass number is odd, l can be 1/2, 3/2, or 5/2. Nuclei with these characteristics possess magnetic properties and can be subjected to NMR measurements, including ^{1}H, ^{13}C, ^{15}N, ^{17}O, ^{19}F, and ^{31}P [157].

In NMR measurements, tetramethylsilane (TMS) is commonly used as a standard. The preference for TMS as a standard is attributed to its numerous advantages. Due to silicon's higher electropositivity than carbon, the TMS signal is observed significantly upfield, and more than 99% of organic compounds resonate to the left of TMS. TMS is inexpensive and non-reactive; it does not react with the measured compounds. The difference in a proton's resonance frequency compared to a standard's resonance frequency is defined as a chemical shift. Identifying functional groups present in a molecule is possible through chemical shifts. Protons with different environments will resonate in other regions of the spectrum because they will be shielded by electrons to varying degrees, leading to peaks in the various areas of the spectrum. An appropriate solvent must be used to prepare a sample for NMR measurement. The solvent should be

inert and not react with the sample; it should also be inexpensive. If the solvent's proton overlaps with the proton of the substance being analyzed, a proper spectrum cannot be observed. Therefore, the solvent should not contain protons. For this purpose, solvents containing approximately 98-99% deuterium, with the remaining 1% being protons, are used. In the case of CdCl3, this corresponds to a peak observed at 7.26 ppm in the proton NMR spectrum. For liquid sample preparation, approximately 0.5 ml of the substance to be analyzed is taken, and about 0.5-0.6 ml of $CdCl_3$ is added. This mixture is then transferred to a 5 mm glass NMR tube. For solid samples to yield a good NMR spectrum, at least 5 mg of the substance is taken, dissolved in an appropriate 5-30 mg solvent for optimal analysis, and transferred to an NMR tube. After obtaining the proton NMR spectrum (1H spectrum), many complex parameters must be evaluated together for interpretation. Chemical shift data, J-coupling values, integrals, and the reactant's conversion are determined with the assistance of an appropriate internal standard.

Mott-Schottky Analysis

Mott-Schottky analysis is a technique used to determine the electronic properties of semiconductors. It provides information about the charge transport and charge transfer processes measured with a potential applied using electrochemical impedance spectroscopy (EIS). According to the Mott-Schottky equation; where C is the capacitance of the semiconductor at the space-charge layer, ϵ, and $\epsilon 0$ are the dielectric constant and the vacuum permittivity, *kB* is the Boltzmann constant, *e* is the electronic charge, *T* is the temperature, and *U* is the applied potential [158]. Drawing a graph from the Mott-Schottky equation (**Eq. 2.6**) provides information about the type of semiconductor. The positive slope of the graph indicates an n-type semiconductor, while the negative slope indicates a p-type semiconductor. The flat-band potential represents the potential applied until there is no difference between the semiconductor's Fermi level and the electrolyte's Fermi level, indicating the absence of a band-bending or charge depletion layer. Determining the flat-band potential *Vfb* from the graph of 1/C2versus *V*, the straight line intersects the X-axis at *Vfb*. At this point, *Vfb* will also determine the Fermi level of the semiconductor.

$$\frac{1}{C^2} = \frac{2}{\varepsilon\varepsilon_0 \varepsilon N_d}(U - U_{FB} - \frac{k_b T}{\varepsilon}) \quad (2.6)$$

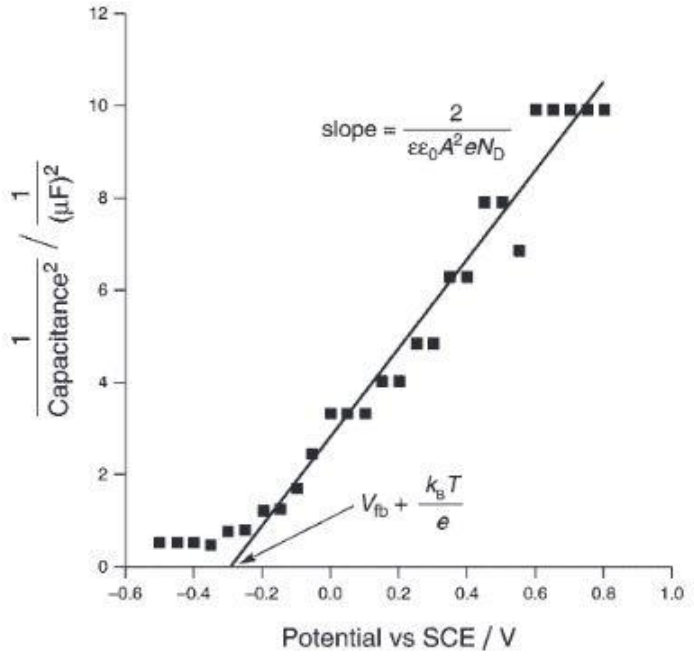

Figure 2.12..An example of a Mott-schottky plot where Vfb indicates the flat band potential [159]

Chapter 3:

TANDEM PHOTOCATALYTIC HYDROGEN EVOLUTION AND SELECTIVE REDUCTION OF NITROARENES USING RP/BP-Pt+PtP_2 HETEROJUNCTIONS

3.1. Introduction

As described in Chapter 2, the outlined synthesis procedure facilitates the one-pot generation of BP nanosheets from RP alongside the concurrent formation of Pt and PtP_2 species within the RP-BP binary heterostructure. This method represents the first example of in-situ generation of PtP_2 Nps from RP, as verified by advanced characterization techniques. Notably, the synthesis protocol is distinctive in its ability to achieve: 1) the simultaneous production of BP nanosheets from RP at mild conditions and 2) the in-situ generation of Pt and PtP_2 NPs from chloroplatinic acid ($H_2PtCl_6.6H_2O$), serving as the platinum precursor, followed by their deposition onto RP-BP binary heterostructures, resulting in RP-BP/Pt+PtP_2 heterojunctions in a single step. Following comprehensive structural characterization of the resulting RP-BP/Pt+PtP_2 heterojunctions, their efficacy as photocatalysts was first evaluated for the HER under visible light irradiation, utilizing TEOA as a hole scavenger and Eosin Y as a photosensitizer, which is higher than that of RP and BP. The notable efficacy demonstrated by the synthesized heterojunctions in the photocatalytic HER, surpassing that of pristine RP and BP, prompted us to formulate a combined strategy for the tandem photocatalytic HER and nitroarene hydrogenation utilizing RP-BP/Pt+PtP_2 heterojunctions as photocatalysts. To facilitate this process, photocatalytic hydrogenation reactions of nitrobenzene were carried out under visible-light irradiation within a homemade photoreactor equipped with 24 W white LED. All necessary equipment for both reactions (HER and nitrobenzene reduction reaction) was integrated into a single reactor. The devised one-pot protocol employing RP-BP/Pt+PtP_2 heterojunctions demonstrated exceptional selectivity in converting nitrobenzene derivatives into corresponding azoxy compounds, achieving remarkable conversion yields of up to 99% using water as the sole hydrogen source.

3.2. Results and Discussion

The RP-BP/Pt+PtP_2 heterojunctions(RP/BP-Pt in short) were synthesized employing RP, a suitable Pt precursor , EDA as stabilizer and solvent and DMF as solvent within a single teflon-coated stainless-steel autoclave reactor. Pt precursor $Pt(acac)_2$ was utilized in synthesizing the RP/BP-Pt heterojunctions, aiming to achieve theoretical Pt ratios of 7 wt% and 10 wt% within the heterojunctions. Upon observing enhanced catalytic activity with the catalyst containing a 7 wt% Pt ratio, the synthesis procedure was repeated by using $H_2PtCl_6.6H_2O$ instead of $Pt(acac)_2$. Interestingly, the catalyst prepared with the $H_2PtCl_6.6H_2O$ exhibited notably higher HER activity than that of $Pt(acac)_2$ (**Figure 3.1**). Subsequent characterization studies were performed by using this optimized catalyst. The experimental Pt ratio, as determined by ICP-MS, was calculated to be 2.56 wt%.

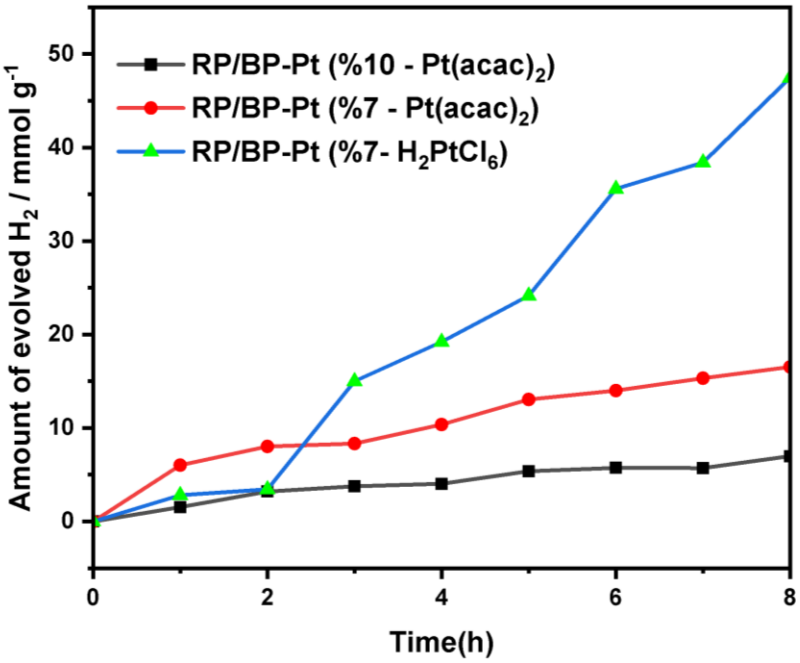

Figure 3.1. Photocatalytic HER activities of the synthesized materials.

During the synthesis of the photocatalyst, as shown in **Figure 2.1.a**, it was observed that alongside the black, crystalline materials resembling BP, as illustrated in **Figure 2.1.b**, the presence of another phase was observed within the sample. This structure appeared dark brown and resembling RP, but unlike the crystalline black phase,

it exhibited a non-crystalline nature. Subsequently, these two distinct phases were carefully separated, and their crystal structures were analyzed by powder XRD. As it is concluded by the XRD patterns in **Figure 3.2**, the upper phase, denoted as RP/BP-Pt_u, revealed a highly crystalline nature, distinctly different from the amorphous RP. A distinct peak at 2θ= 12.6° suggested an expansion of the orthorombic BP lattices compared to those of pristine, crystalline BP, possibly due to EDA intercalation into the BP lattice, namely periodic distortion.[98] The peak detected at 2θ= 20.6°, displaying an approximate 2° shift, was assigned to the (020) plane characteristic of the orthorhombic BP.[160] Changes in diffraction angles and peak positions may occur due to modifications in the BP lattice parameters upon adding Pt or EDA interaction. Besides BP formation, the peak observed at 2θ= 27.6° was attributed to the (111) plane of crystalline cubic PtP_2, further supporting the generation of PtP_2 NPs during the synthesis [161]. After the observation of PtP_2 formation, the name of this heterostructure was denoted as RP/BP-Pt+PtP_2. The lower phase, RP/BP-Pt_b, which is observed as dark brown and resembling RP but exhibits a different amorphous structure from RP, is noteworthy characterized. The literature survey states that there are various phases of RP possible. The observed new amorphous structure suggests the formation of a new amorphous phase of RP or one of its amorphous allotropes [162]. Peaks observed at 2θ= 40.0°, 46.5°, and 67.7° corresponded to the (111), (200), and (220) planes of face-centered cubic (fcc) Pt, respectively, indicating the successful synthesis of Pt NPs within the structure. (JCPDS no. 00-004-0802).

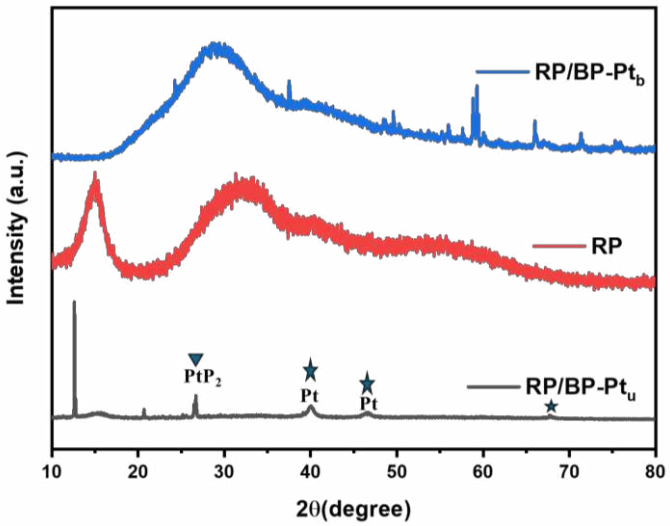

Figure 3.2.XRD pattern of RP, RP/BP-Pt_u, and RP/BP-Pt_b.

TEM and HR-TEM analyses were conducted to examine the morphological properties of as-synthesized materials. **Figure 3.3.a** illustrates the layered structure of RP, with regions of varying thicknesses observed within the material, depicted as light and dark areas in TEM images corresponding to different thicknesses. **Figure 3.3.b** demonstrates the thin, layered structure of BP nanosheets. **Figure 3.3.c** shows the TEM image of RP/BP-Pt, the material containing both upper and lower phases, to be further analyzed in subsequent characterization sections. Similar to BP, this image exhibits a thin-layered structure, with Pt NPs distributed uniformly on the surface with an approximate particle size of 3.5 nm. **Figure 3.3.d** displays the HR-TEM image of RP/BP-Pt. The lattice spacing calculated using inverse-fast-fourier-transform (IFFT) analysis, with d=0.254 nm, corresponds to (040) plane of BP. The presence of Pt NPs is confirmed by a lattice spacing of d=0.23 nm, corresponding to the (111) plane of face centered cubic (fcc) Pt, indicating successful synthesis of the heterostructure. **Figure 3.3.e** presents the HR-TEM image of RP/BP-Pt_u, with a lattice spacing of d=0.282 nm calculated by using IFFT, corresponding to the (020) plane of PtP_2, thus confirming PtP_2 formation [163]. **Figure 3.3.f** shows the TEM image of RP/BP-Pt_b, with Pt NPs evenly distributed on the structure's surface and the observed thin, layered structure of BP.

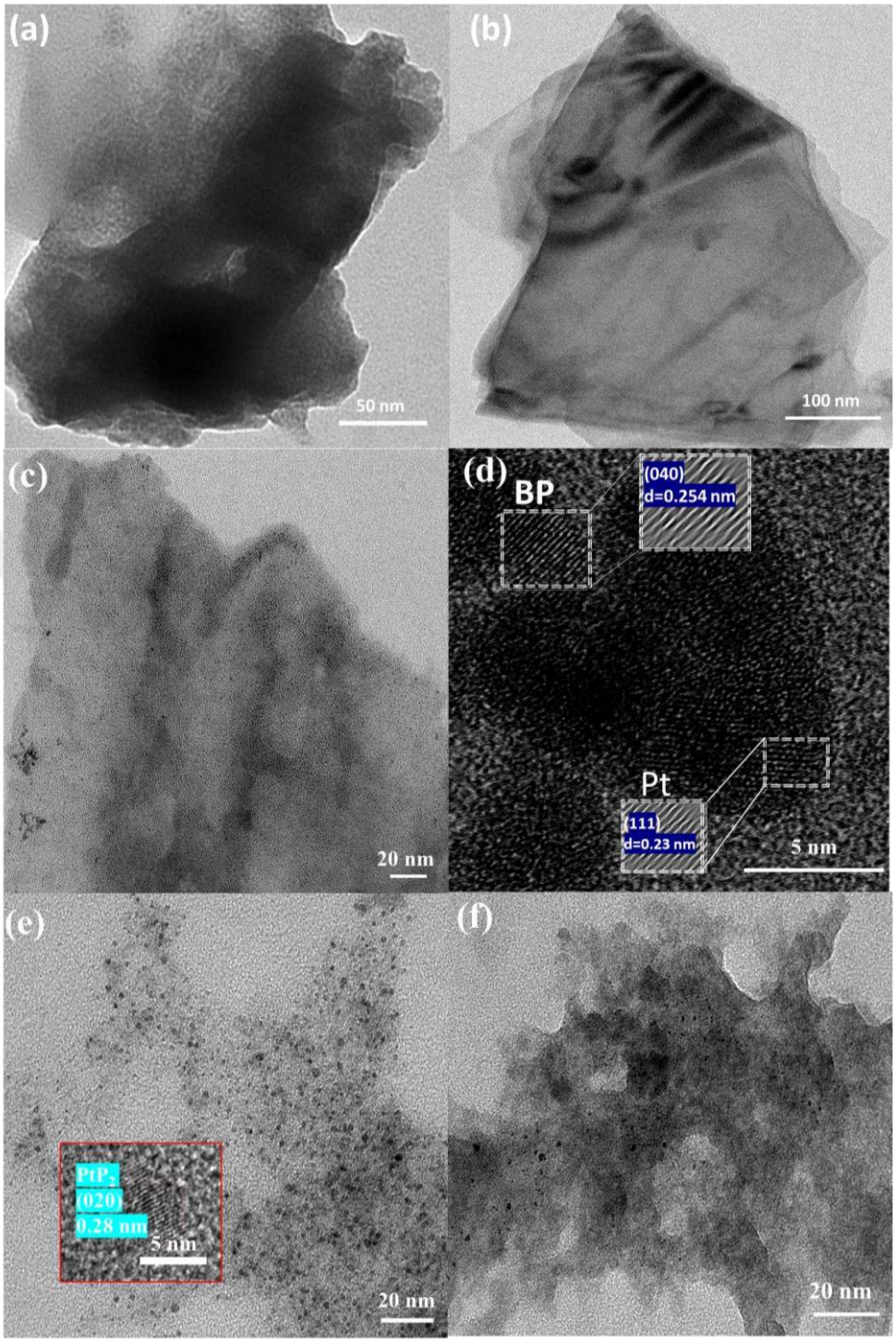

Figure 3.3. TEM image of a)RP, b)BP nanosheets, c)RP/BP-Pt(overall), HR-TEM image of d)RP/BP-Pt, e)RP/BP-Pt_u, f)TEM image of RP/BP-Pt_b.

Figure 3.4 displays the High-Angle Annular Dark Field (HAADF) STEM images of RP/BP-Pt. The images illustrate the distribution of corresponding elements within the

structure, including P, Pt, and O. It is evident that the entire structure is covered with oxygen due to the unavoidable oxidation of BP during synthesis and laboratory conditions. Pt NPs exhibit a uniform distribution on the heterostructure.

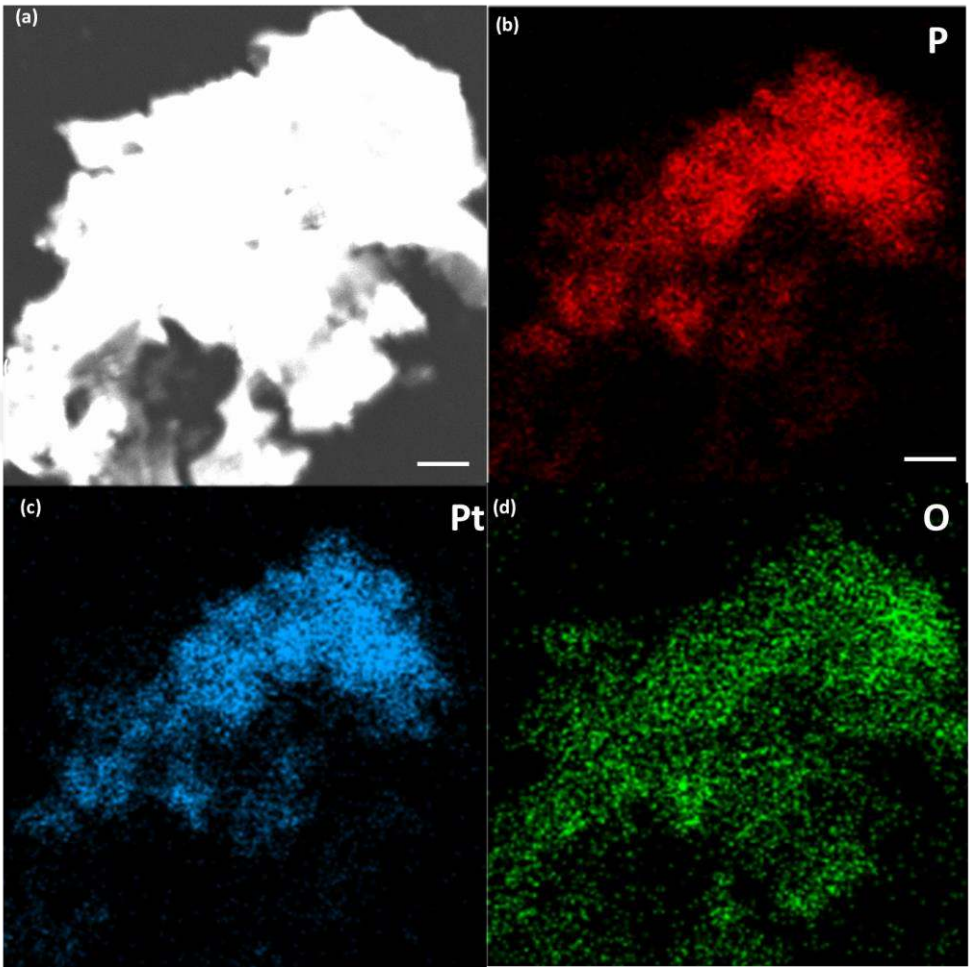

Figure 3.4. HAADF-STEM image of RP/BP-Pt.

The surface morphology of the materials was examined via SEM analysis. In **Figure 3.5**, an SEM image of RP reveals the presence of irregularly shaped particles of various sizes. **Figure 3.5.b** shows the structure of RP/BP-Pt, characterized by flat sheets and plate-like structures. The more regular appearance compared to RP is attributed to the crystalline structure of BP within RP/BP-Pt. The presence of both regular layered structures and irregular shapes resembling RP suggests the presence of RP or another amorphous allotrope of RP within the structure. When evaluated alongside XRD data, the nomenclature of this heterostructure as RP/BP-Pt can be attributed to these findings.

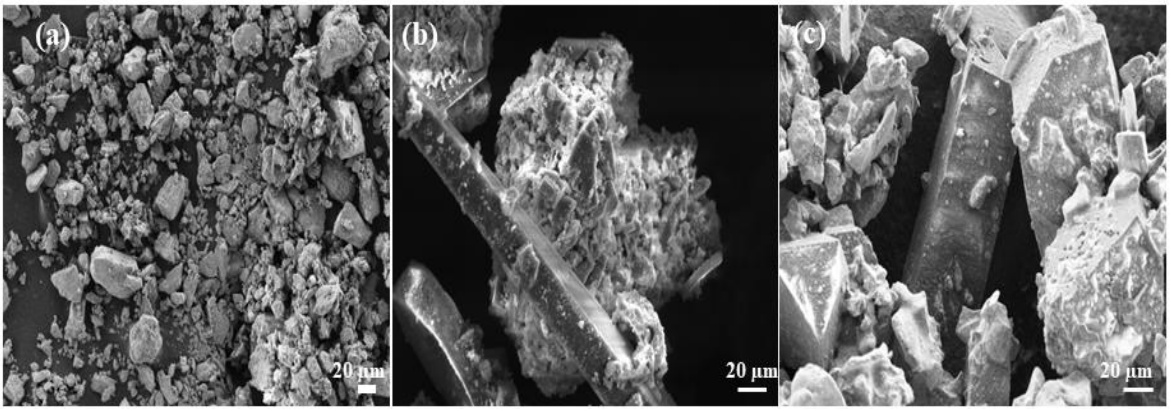

Figure 3.5. SEM image of a)pristine RP, b,c)RP/BP-Pt.

XPS analysis was performed to obtain information about the chemical states of elements on the surface of RP/BP-Pt The XPS survey spectrum confirms the presence of all elements constituting the structure: C, N, O, P, Pt (see Appendix **Figure A.1**). **Figure 3.6.a** shows the high-resolution P2p XPS spectrum of RP and RP/BP-Ptu. Peaks in the 129-131 eV range correspond to the elemental phosphorus $P2p_{3/2}$ and $P2p_{1/2}$ core levels, indicating the presence of tetrahedral P_4 molecules bonded to other phosphorus atoms (P-P) [90]. Compared to pristine RP, a decrease in intensity of P_4 molecule-related peaks and their shifts to lower binding energies in the binding energy range of 129-131 eV indicates less percentage of elemental P atoms within the structure in the P2p spectrum of RP/BP-Pt_u. Conversely, the intensity of phosphorus atoms with higher oxidation states (P_xO_y and other oxidized phosphorus species) increases compared to RP, with no significant shift in binding energy. These results suggest a remarkable Pt-P interaction and PtP_2 formation, indicating that P atoms transfer their lone pair electrons to the appropriate d orbitals of Pt (increased intensity at 132-134 eV represents the higher oxidation state of P, and decreased intensity at 129-131 eV represents the elemental phosphorus) and partially retrieve some electrons through π-back bonding (shifting towards the low binding energy observed on elemental P peaks) [164] [165]. Compared to the P2p spectrum of RP, the increased intensity of the peak in the 132-134 eV range is attributed not only to the P_xO_y species but also to the contribution of the Pt-P bond in this region to the peak intensity. Higher intensity of this peak in RP/BP-Pt_u indicates that PtP_2 species are predominantly present within RP/BP-Pt_u. The presence of PtP_2 within this phase has been further confirmed through HR-TEM and XRD analysis. The most significant challenge

encountered when working with RP and BP is their exposure to oxidation due to lone pair electrons of phosphorus atom. Therefore, XPS analysis often reveals oxidized phosphorus species such as phosphates (PO_4^{2-}) and phosphites (PO_3^-), contributing to the increased intensity observed in the peaks in the high binding energy range of 132-134 eV. Consequently, oxidized phosphorus species are observed in RP/BP-Pt_u samples. **Figure 3.6.b** shows the Pt4f spectrum, where two pairs of doublets are observed at 71.4-74.7 eV and 72.6-76 eV. These peaks indicate different oxidation states of Pt, corresponding to metallic Pt and Pt(II), respectively. Pt(IV) ions are entirely reduced to predominantly form Pt (O), i.e., Pt NPs, with the Pt NP ratio being higher than Pt(II). Additionally, the presence of Pt(II) indicates the formation of PtP_2 [166]. **Figure 3.6.c** depicts the O1s spectrum, showcasing various oxidized P2p species observed in the P2p spectrum, including chemisorbed oxygen and surface oxygen.

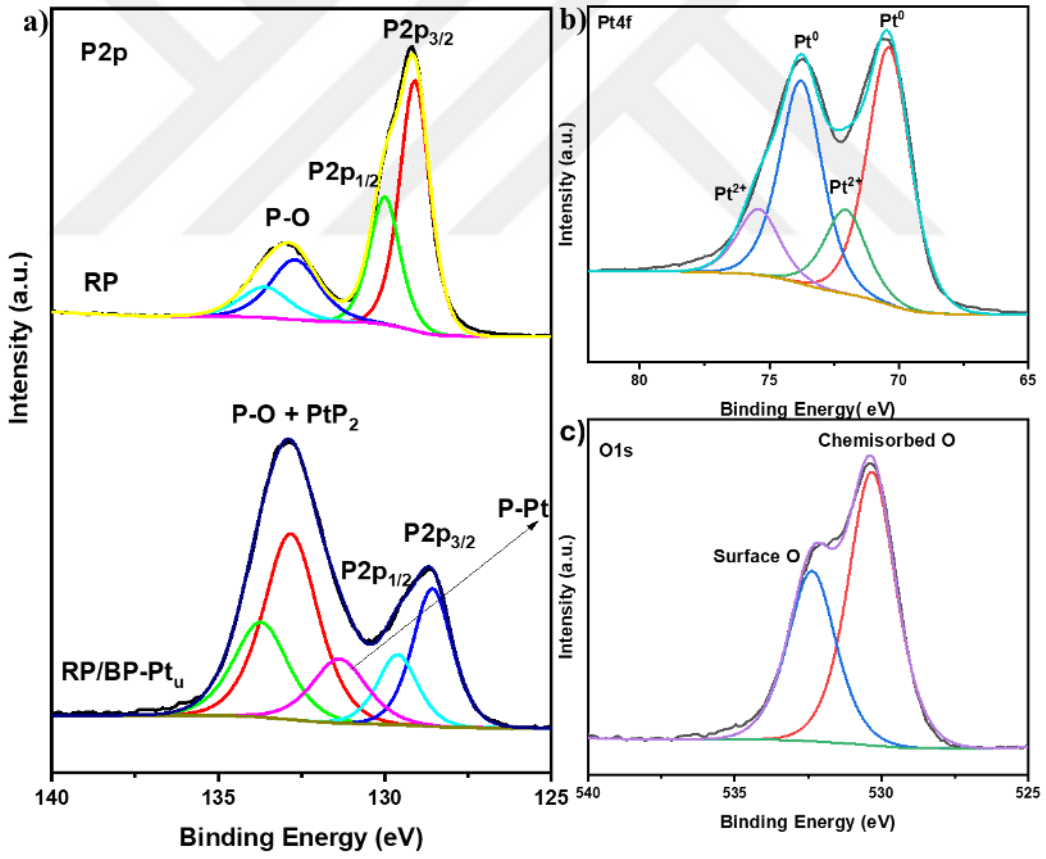

Figure 3.6. High Resolution XPS (HR-XPS) Spectra of RP/BP-Pt_u, a)P2P spectra of RP and RP/BP-Pt_u, b)Pt4f spectra, c)O1s spectra.

Figure 3.7 shows the C1s spectrum. The peak at 284.5 eV corresponds to the reference C-C peak from the carbon grid. The peak at 286 eV arises from the carbon-nitrogen (C-N) bond of ethylenediamine (EDA), which was used as a chelating agent during the synthesis stage. It indicates the coordination of EDA into the structure [167].

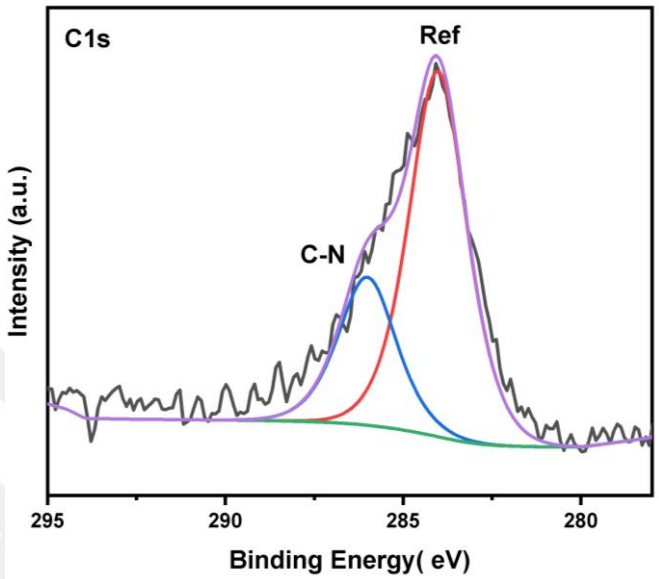

Figure 3.7. HR-XPS C1s spectra of RP/BP-Pt_u.

Figure 3.8 illustrates the P2p and Pt4f spectra of RP/BP-Pt, comprising both the lower and upper phases-RP/BP-Pt_b and RP/BP-Pt_u, respectively-without undergoing a separation process into two parts after synthesis. A noticeable shift to higher binding energy is observed in the P2p spectrum of RP/BP-Pt_b compared to RP and RP/BP-Pt. As mentioned in the XRD spectrum of RP/BP-Pt_b, besides phosphorus' amorphous allotrope other than RP, sharp peaks indicating the presence of other species have also formed within the material. Additionally, P-O peaks in the 132-134 eV range indicate the dominance of oxidized phosphorus species such as PO_4^{2-} or PO_3^- within the material. No peak attributed to Pt-P is observed within this phase. Within RP/BP-Pt, which includes RP/BP-Pt_u or PtP_2 species, a lower binding energy is observed compared to RP/BP-Pt_b—PtP_2 species within this phase, resulting in a lower binding energy. Upon examination of the Pt4f spectrum, it is observed that the ratio of Pt NPs within RP/BP-Pt is much higher than that of Pt(II), indicating the successful generation of Pt NPs by the synthesis method.

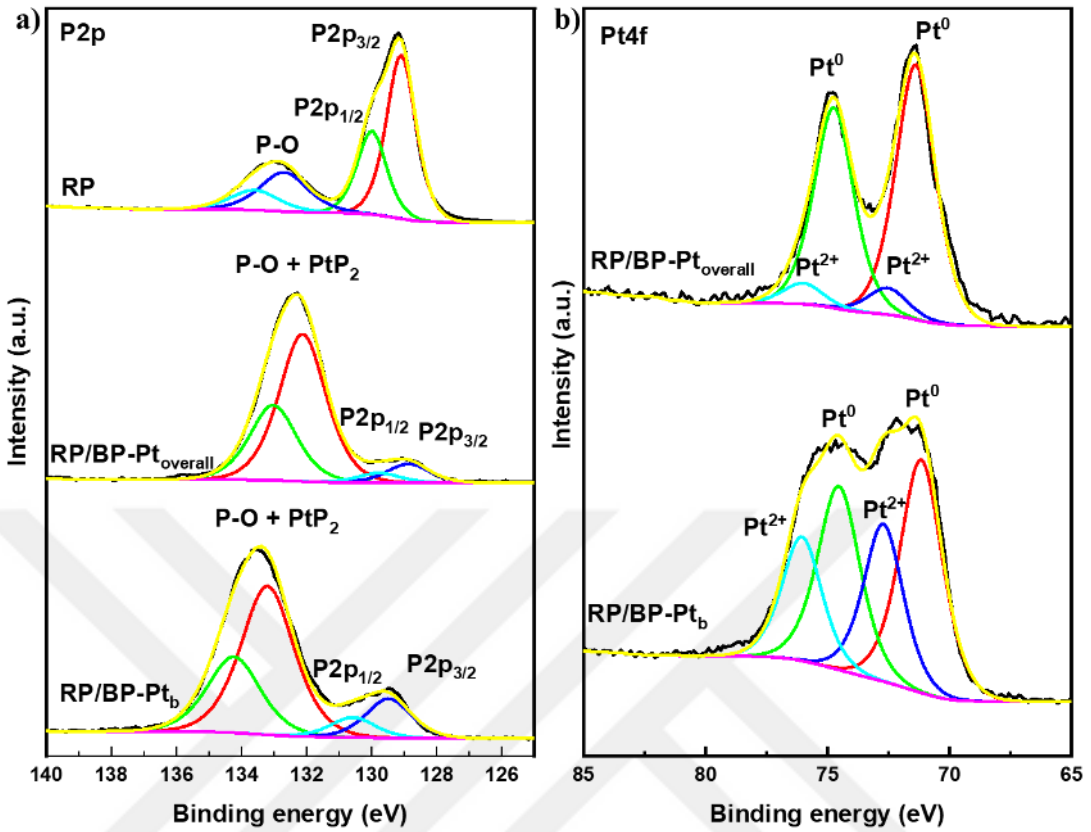

Figure 3.8. HR-XPS spectra, a)P2p spectra and b)Pt4f spectra of RP/BP-Pt and RP/BP-Pt_b.

UV-Vis diffuse reflectance spectroscopy (UV-Vis DRS) analysis was conducted to examine the optical properties of the materials. The reflectance spectrum was converted to the absorbance spectrum using the Kubelka-Munk equation. **Figure 3.9.a** illustrates the absorption behavior of the synthesized materials. RP/BP-Pt_u exhibits a significantly broad light absorption capacity, shifting towards the near-infrared (NIR) region compared to RP and RP/BP-Pt_b. RP/BP-Pt overall also possesses an absorption edge shifting towards the NIR region, similar to RP/BP-Pt_u. These observations indicate the presence of interfacial interactions between RP and BP in the heterostructure of RP/BP-Pt [96]. Band gap energies were determined from the reflectance spectra using the Tauc plot analysis (**Figure 3.9.b**). According to **Eq. 2.5**, the Tauc plot equation for a direct band gap semiconductor transforms to $(\alpha h\nu)^2 = A(h\nu - Eg)$. Compared to pristine RP, all samples demonstrated enhanced light absorption capabilities and reduced band gap

energies. RP/BP-Pt_u and RP/BP-Pt showcased a significantly diminished band gap compared to pristine RP, leading to enhanced charge transport mobility and improved photocatalysis performance. **Figure 3.9.c** demonstrates a decline in the emission intensity of the overall sample (RP/BP-Pt) compared to pristine RP. Reduced photoluminescence emission signifies effective charge separation, consequently reducing electron-hole pair recombination and enhancing photocatalytic performance. In RP/BP-Pt, there is a slight decrease in the average lifetime of charges, as depicted in **Figure 3.9.d.** For a Schottky junction catalyst, this decrease in lifetime suggests an accelerated transfer of charges from the semiconductor to the metal through electron transfer pathways [168]. Consequently, this process enhances photocatalytic efficiency by minimizing charge carrier recombination.

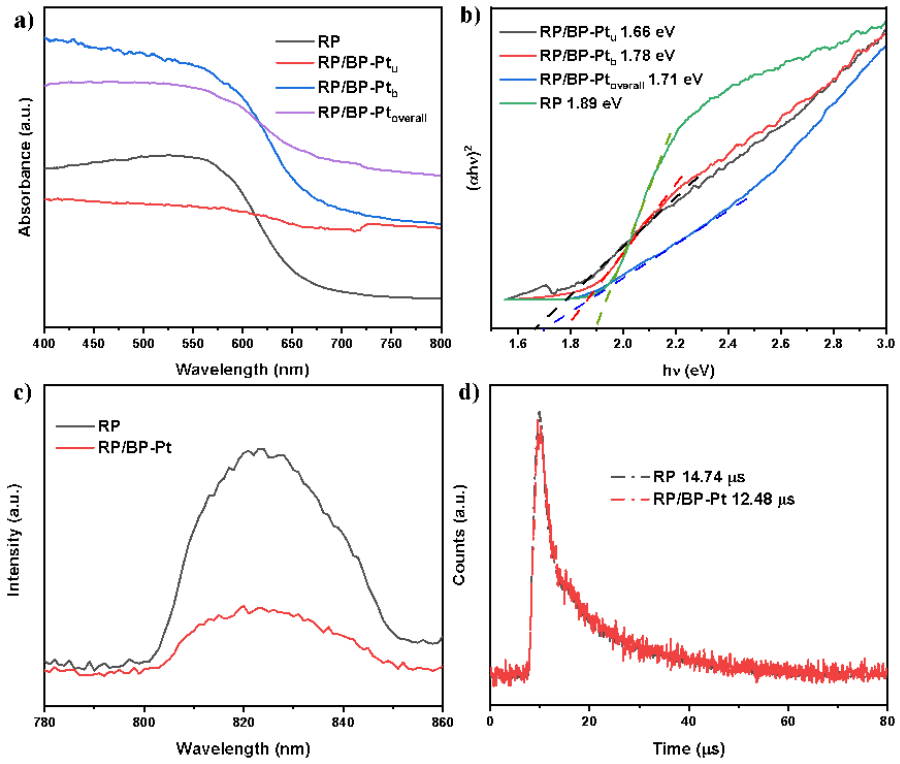

Figure 3.9. a)UV-Vis-DRS spectra, b)Tauc plot analysis of RP/BP-Pt, RP/BPPt_u, RP/BP-Pt_b, RP, c)PL and d)TRPL spectra of RP and RP/BP-Pt heterostructure

Mott-Schottky analyses were conducted to elucidate the migration of charge carriers between the semiconductor and the metal interface. **Figure 3.10** displays the calculated flat band potentials (E_{fb}) for RP and RP/BP-Pt obtained through Mott-Schottky

analysis. For RP, it was determined to be -0.76 V, and for RP/BP-Pt, it was -0.87 V vs. Ag/AgCl. The Efb values were converted to NHE using $E_{NHE} = E_{Ag/AgCl} + 0.197$ [169]. The positive slope of the graphs indicates that the semiconductor is n-type, confirming that both RP and RP/BP-Pt are n-type semiconductor materials. It is known that for n-type semiconductors, the calculated Efb equals the Fermi level (Efl) (RPfl: -0.56 V vs. NHE, RP/BP-Ptfl: -0.67 V vs. NHE). It is also known that the conduction band (E_{CB}) of an n-type semiconductor is approximately 0.1 V negative relative to the Fermi level [170]. Thus, the E_{CB} values for RP and RP/BP-Pt were determined to be -0.66 V and -0.77 V vs. NHE, respectively. It was observed that RP/BP-Pt exhibits a more negative conduction band potential than RP.

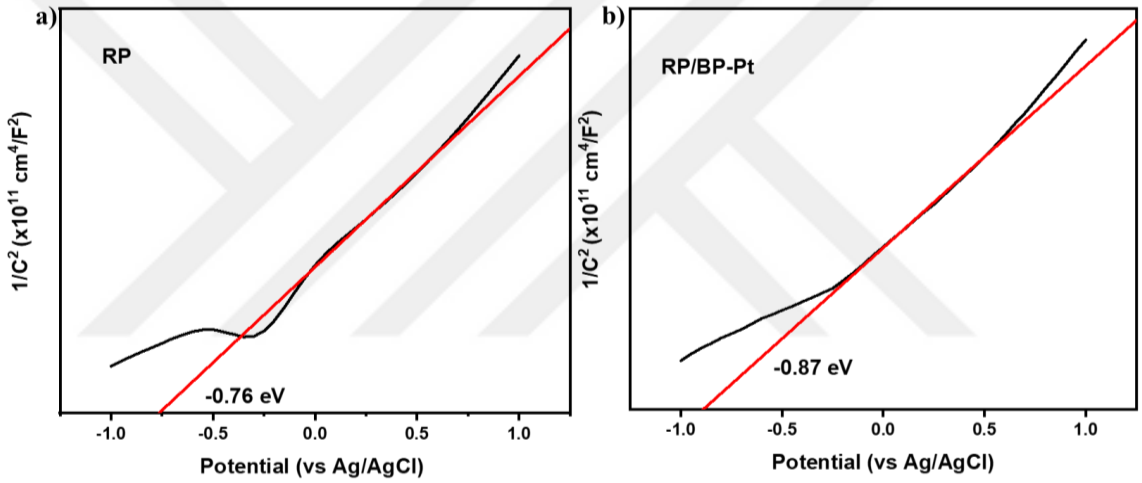

Figure 3.10. Mott Schottky plots of a)RP , b) RP/BP-Pt heterostructure.

Figure 3.11 depicts the performance of all synthesized materials and their pristine derivatives. The experiments were conducted under visible light irradiation, employing TEOA as a hole scavenger and Eosin Y as a light sensitizer. In the experiments conducted without EY, no hydrogen production was observed, necessitating the addition of EY to all experiments. Upon the introduction of EY into the reaction cell, the hydrogen evolution rate of RP/BP-Pt reached 47.46 mmol g^{-1} h^{-1}, emphasizing the crucial role of EY dye sensitization in observing HER activity. RP and BP, RP/BP-Pt_u, and RP/BP-Pt_b were evaluated to compare HER performances. The photocatalytic HER rates achieved by RP, BP, RP/BP-Pt_b, and RP/BP-Pt_u were 1.204, 2.964, 9.577, and 13.102 mmol g^{-1} h^{-1}, respectively. Notably, the enhancement in HER activity upon combining RP/BP could

be attributed to the forming of an internal heterojunction between two distinct semiconductor materials. Despite having lower Pt content (2.16 wt% for RP/BP-Pt_u and 2.56 wt% Pt for RP/BP-Pt_b), RP/BP-Pt_u exhibited higher HER performance. The overall sample, RP/BP-Pt, demonstrated significantly higher HER activity than both RP/BP-Pt_u and RP/BP-Pt_b. The superior activity of the overall RP/BP-Pt heterostructured photocatalysts, derived from both individual phases by mixing the two materials, can be attributed to the formation of homojunctions that creates a synergistic effect between PtP_2 species in RP/BP-Pt_u and the amorphous material in the below phase [171].

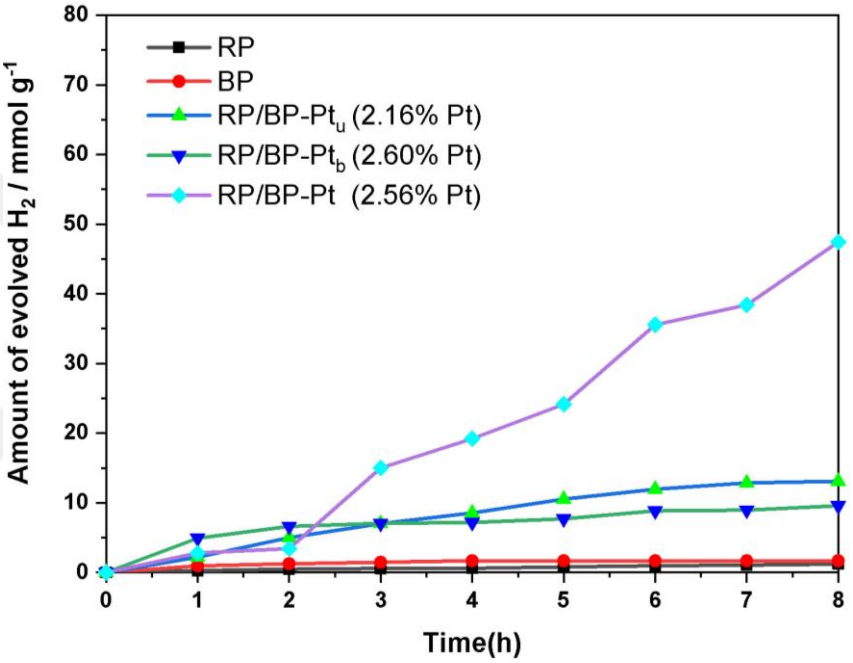

Figure 3.11.Photocatalytic HER performances of RP, BP, RP/BP-Pt_b, RP/BP-Pt_u and RP/BP-Pt.

Through detailed characterization studies, an Eosin Y (EY) sensitized photocatalytic HER mechanism has been proposed for RP/BP-Pt. HER. EY molecules absorb visible light and reach a single excited state, EY1*. Subsequently, EY1* is transformed into the more stable triplet state, EY3*. In this process, the EY3* state is quenched to form $EY^{-\bullet}$ by triethanolamine (TEOA), acting as an electron donor [172]. The photogenerated electrons are then transferred through the CB of RP/BP due to the energy level difference. The electrons are transferred from the CB of RP/BP to Pt and combine with protons (H^+) on Pt to facilitate H_2 production. TEOA acts as an electron

donor, facilitating the regeneration of EY molecules. Additionally, TEOA acts as a hole scavenger, preventing the recombination of electrons and holes, thereby enhancing the efficiency of the photocatalytic reaction (**Figure 3.12**).

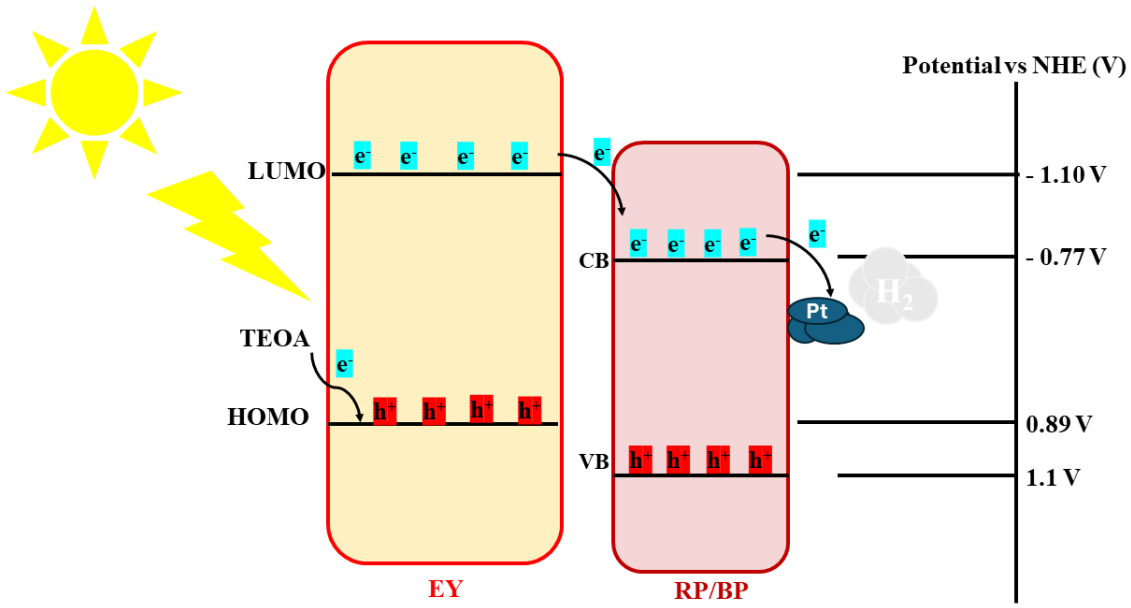

Figure 3.12. Proposed photocatalytic HER mechanism of EY sensitized RP/BP-Pt heterostructure.

3.2.1. Photocatalytic Reduction of Nitrobenzene compounds

This section elaborates on the outcomes of nitrobenzene reduction reactions using the RP/BP-Pt-PtP_2 (RP/BP-Pt in short) heterostructured photocatalyst. After observing the superior performance of the RP/BP-Pt catalyst in photocatalytic HER, we selected the reduction of the nitrobenzene compound as a model reaction. It aims to integrate the concept of one-pot tandem photocatalytic HER and photocatalytic nitrobenzene reduction to utilize hydrogen produced from water in transfer hydrogenation. We combined all necessary components for photocatalytic HER and nitrobenzene compound reduction in a single vessel to conduct reactions. TEOA and EY served as hole scavengers and photosensitizers respectively, for the HER reaction conducted under visible-light irradiation. White LED (24 W) was used as the light source in RP/BP-Pt catalyst experiments. Light, photocatalyst, and base are crucial parameters for photocatalytic reactions, and the absence of any of these components resulted in no reaction. While

methanol is known as a hole scavenger, it was found insufficient to reduce nitrobenzene compounds. Methanol's role here was elucidated as acting as a solvent and providing a suitable environment for the dissolution of nitrobenzene compounds. Hence, TEOA introduced to the system as an effective hole scavenger. The base was identified as an essential parameter in these experiments. It contributes to the formation of azoxybenzene(AOB) and azobenzenes(AZB) by facilitating the combination of nitrosobenzene (NSB) and phenylhydroxylamine (PHA) generated during the reduction of nitrobenzene. Sodium hydroxide (NaOH) was selected as the base used in this experiment because it exhibited higher performance than other alternatives, such as KOH.

Table 3.1. Comparison of the photocatalytic activities in nitrobenzene reduction

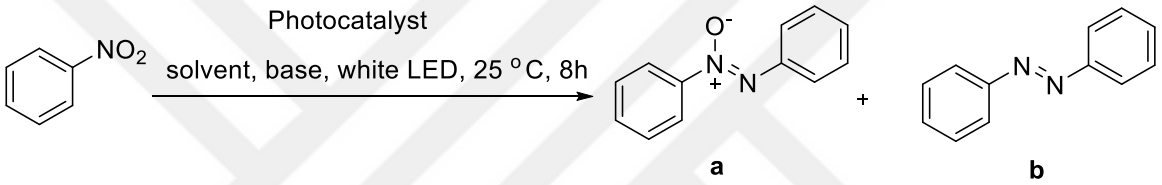

Entry	Catalyst	Solvent	Sacrificial agent	Conversion (%)	Selectivity (%) a	b
1	RP/BP-Pt	H_2O:MeOH	TEOA	>99	>99	
2	RP/BP-Pt_u	H_2O:MeOH	TEOA	>99	>99	
3	RP/BP-Pt_b	H_2O:MeOH	TEOA	>99	>99	

Reaction conditions: 0.25 mmol nitrobenzene, 5 M NaOH, 10 mg photocatalyst, irradiation with white LED(24 W) for 8h at 25 ^{o}C, EY(3.25×10^{-4} M), TEOA(5%), H_2O:MeOH(2:3)

During the characterization studies, the photocatalytic HER activities of the RP/BP-Pt, RP/BP-Pt_u, and RP/BP-Pt_b catalysts were measured separately. The photocatalytic activities of these catalysts in the photocatalytic nitrobenzene reduction reaction were compared. Nitrobenzene was selected as the substrate for the reaction. No difference in activity was observed among the catalysts (**Table 3.1**.). Therefore, experiments continued with the overall RP/BP-Pt catalyst when conducting substrate-

scope studies with nitrobenzene molecules containing different groups.

The synthesized overall RP/BP-Pt heterojunction photocatalysts exhibited efficient reduction capabilities in the reaction of 1-chloro-4-nitrobenzene, achieving complete conversion with >99% selectivity towards the azoxybenzene derivatives (**Table 3.2.,** Entry 1). The efficacy of the RP/BP-Pt photocatalyst and associated reaction parameters extends beyond nitrobenzene to encompass different nitrobenzene derivatives, as evidenced by the reduction capabilities demonstrated for both nitrobenzene itself, as outlined in **Table 3.1**, and various nitrobenzene derivatives detailed in **Table 3.2**. Pristine BP and RP (Entry 2 and 3) yielded low results under the same reaction conditions. Parallel to the results observed in photocatalytic HER, the newly established heterostructure yielded superior results in nitrobenzene reduction reactions compared to the pristine forms. We selected TEOA as the hole scavenger for the photocatalytic HER reaction and incorporated it into the one-pot tandem reaction for the same purpose. However, we conducted experiments to observe their effects using known hole scavengers, including ethylene glycol, acetic acid, formic acid, oxalic acid, and glycerol. These alternative hole scavengers resulted in lower conversions than TEOA (**Table 3.2**, entries 4, 5, 6, 7, 8). Eosin Y is employed in photocatalytic HER as a light sensitizer. We propose that its role is to function as a light sensitizer, as there is an overlap between its absorption spectra and that of the catalyst (**Figure A.2**.). Under these conditions, excluding the photocatalyst, while keeping other variables constant, the reaction conversion yields can be measured at around 30%, leading to a mixture of azoxy and azobenzene derivatives. (**Table 3.2**, entry 9) This finding indicates that Eosin Y can donate electrons to the nitrobenzene molecules to some extent. However, upon introducing the photocatalyst into the reaction system, a significant improvement in conversion was observed, reaching >99% with an exceptional selectivity of >99%. The presence of base (NaOH) is crucial for the reaction, as its absence leads to a significantly low conversion (**Table 3.2**, entry 10). We performed the reaction under a nitrogen atmosphere (**Table 3.2**, entry 11), and no substantial decrease in reaction yield was noted, affirming that the reaction proceeds through an electron transfer pathway.

Table 3.2. Optimization of the reaction conditions

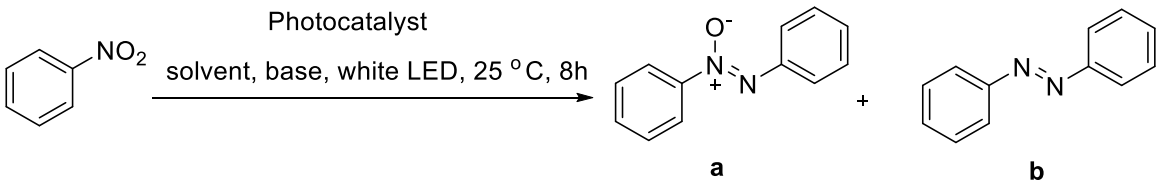

					Selectivity (%)	
Entry	R	Catalyst	Hole scavanger	Conversion (%)	a	b
1	p-Cl	RP/BP-Pt	TEOA	>99	>99	-
2	p-Cl	BP	TEOA	47	>99	-
3	p-Cl	RP	TEOA	60	>99	-
4	p-Cl	RP/BP-Pt	Ethylene glycol	10	-	-
5	p-Cl	RP/BP-Pt	Acetic acid	5	-	-
6	p-Cl	RP/BP-Pt	Formic acid	10	-	-
7	p-Cl	RP/BP-Pt	Oxalic acid	10	-	-
8	p-Cl	RP/BP-Pt	Glycerol	-	-	-
9	p-Cl	-	TEOA	30	>99	-
10	p-Cl	RP/BP-Pt	TEOA	10[a]	-	-
11	p-Cl	RP/BP-Pt	TEOA	77[b]	>99	

Reaction conditions: 0.25 mmol 1-chloro-4-nitrobenzene, 10 mg photocatalyst, NaOH solution used as base, EY(3.25×10^{-4} M), irradiation with white LED(24 W) for 8 h at 25 ^{0}C, a=without base, b=N_2 atmosphere

We broadened our investigation to encompass further nitrobenzene derivatives, employing the optimized reaction conditions for the tandem photocatalytic HER and hydrogenation of nitroarenes facilitated by the RP/BP-Pt heterostructure. As mentioned in Table 3.2, when a nitrobenzene molecule without substituents is employed, the reaction proceeds with complete conversion, yielding azoxybenzene product with over 99% selectivity (**Table 3.3**., 2a). The reduction of halogenated nitrobenzene compounds, specifically 1-chloro-4-nitrobenzene and 1-bromo-4-nitrobenzene, was investigated. The substrates underwent complete conversion, resulting in the exclusive formation of azoxybenzene derivatives with a selectivity of more than 99% (**Table 3.3.** 2b and 2c). Conversely, 1-iodo-4-nitrobenzene led to a complex reaction mixture that couldn't be identified (**Table 3.3.**, 2g). When the 4-nitrotoluene substrate was employed, azoxybenzene derivative was obtained with complete conversion and high selectivity. (**Table 3.3**., 2d) In the reaction with 1-bromo-4-nitrobenzene, only the azoxybenzene derivative was produced. However, using 1-bromo-3-nitrobenzene resulted in a mixture of azoxy and azobenzene derivatives. The major product in this mixture was the azobenzene derivative, with a high selectivity of 95% (**Table 3.3**., 2f and 3f). This indicates a preference for the azobenzene derivative when 1-bromo-3-nitrobenzene is the starting material. The differences observed in product formation stem from the electronic and steric effects exerted by the substituents' positions on the aromatic ring. In line with the observations, another experimental outcome illustrates that while 1-chloro-4-nitrobenzene produced the azoxybenzene derivative, the use of 1-chloro-2-nitrobenzene led to low conversion and the generation of a dehalogenation product.(**Table 3.3.**, 2h The following attributes this phenomenon: with the para-substituted compound, the increased distance between the chlorine and nitro groups reduces steric hindrance, thus facilitating a more effective reduction reaction. Conversely, in the ortho-substituted analog, the proximity of the chlorine and nitro groups promotes interactions between them, decreasing the photocatalyst's ability to interact with the nitro group. This reduced reactivity eventually fosters the formation of the dehalogenation product, making the reduction process less favorable. The substrate scope study of the RP/BP-Pt catalyst has been limited to these nitrobenzene compounds. We could not achieve noteworthy outcomes with nitrobenzene compounds containing diverse substituents.

Table 3.3. Substrate scope study of RP/BP-Pt

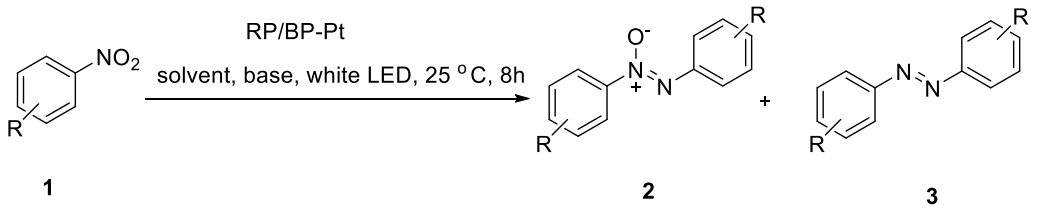

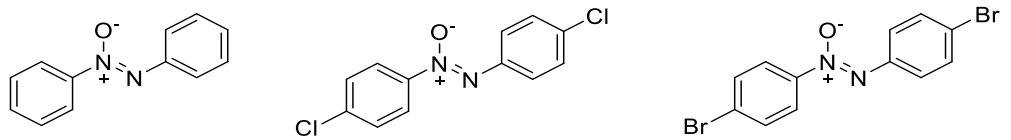

2a
C: >99%
S: > 99%

2b
C: >99%
S: >99%

2c
C: >99%
S: >99%

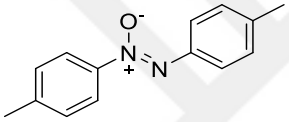

2d
C: >99%
S: >99%

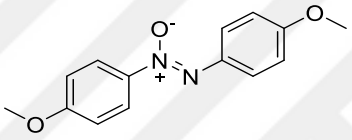

2e
C: >99%
S: >99%

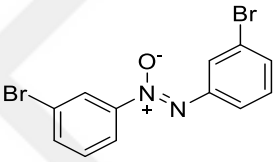

2f
C: >99
S: 5%

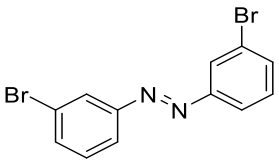

3f
C:>99
S: 95%

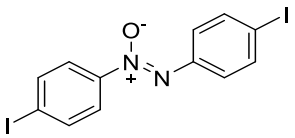

2g, NI

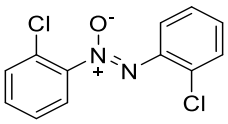

2h, NR

Reaction conditions: All reactions were performed custom-made, tightly-sealed photoreactor equipped with 0.25 mmol nitrobenzene derivative, photocatalyst (10 mg), H_2O:MeOH(2:3), 2 ml NaOH solution, TEOA(5%) and Eosin Y dye solution at room temperature and irradiated with white LED(24 W), NI:not identified, NR: no reaction, The numerical data were obtained from GC-MS and calculated using an internal standard.(1,3-dinitrobenzene), C:Conversion, S:Selectivity

We conducted reusability tests to evaluate the stability of the catalyst. Unlike the standard conditions, the amount of catalyst was increased to 40 mg after each experiment to prevent loss during the washing process. At the end of each trial, we separated the catalyst from the organic phase by washing it with hexane and ethyl acetate. The selectivity value gradually decreased after each experiment, reaching 65% by the fourth trial. (**Figure 3.13**) The decrease in reaction conversion can be attributed to the oxidation of phosphorous atoms in the aqueous solution, which leads to a decline in catalyst activity. In addition, the loss of catalyst quantity experienced at the end of each experiment also contributed to the reduced reaction activity.

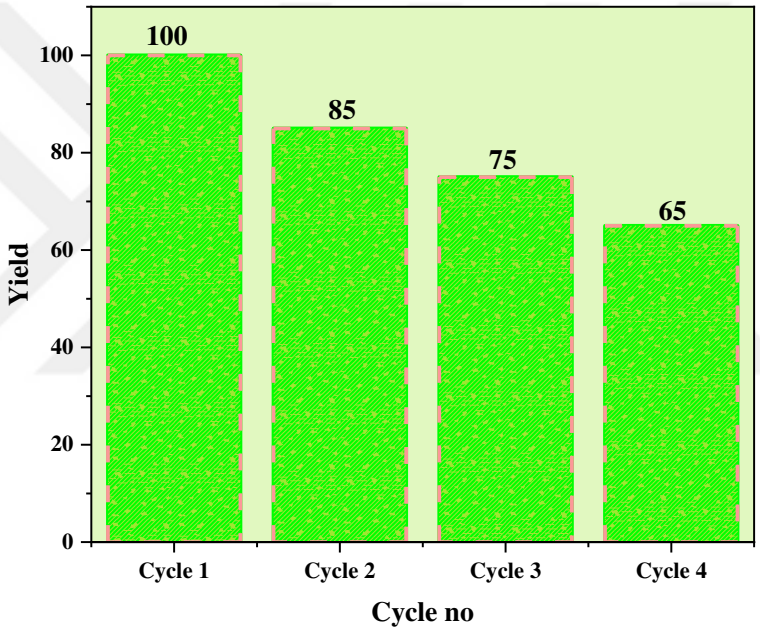

Figure 3.13..Reusability of RP/BP-Pt on nitrobenzene reduction reaction.

Mechanistic studies

We performed a series of mechanistic studies to comprehend the processes involved in the hydrogenation mechanism. In the tandem HER (hydrogen evolution reaction) and photocatalytic reduction of nitrobenzene experiment using the RP/BP-Pt catalyst, deuterium labeling experiments were performed to identify the source of hydrogen required for the reaction under optimized reaction conditions. Upon examining the reaction results, the predominant products were mainly azoxybenzene derivatives and

azobenzene, compounds devoid of hydrogen atoms. Hence, nitrobenzene, the substrate, was substituted with benzaldehyde. The product formed upon the hydrogenation of benzaldehyde was investigated by substituting the hydrogen with deuterium atoms. Similarly, to prevent the hydrogen atoms originating from NaOH, which served as the base, NaOH was replaced with KOtBu and dissolved in D_2O. The deuterated product was detected at m/z=109 via GC-MS analysis.(**Figure A.3**) This outcome is crucial evidence indicating that the hydrogen atoms originate from water.

We investigated potential pathways to enhance our understanding of the hydrogenation mechanism through water splitting. The hydrogen sources used in the hydrogenation reactions have been described in the previous sections. To date, hydrogenation for the one-pot tandem HER (hydrogen evolution reaction) and photocatalytic reduction of nitrobenzene described here can be achieved using hydrogen obtained from water splitting. Another possible route for hydrogenation involves the dehydrogenation of water, where the breaking of the O-H bond leads to the production of hydrogen atoms, which can undergo hydrogenation by being incorporated into electron acceptor molecules during hydrogen peroxide (H_2O_2) production (See **Figure 1.13**) [145]. A spectrophotometric I_3^- titration experiment was conducted to observe the formation of hydrogen peroxide and the resulting I_3^- was detected using UV-Vis spectrophotometer (**Figure 3.14**). The H_2O_2 reacts with KI to yield a yellow I_3^- formation, which was observed with a peak at approximately 350 nm. The presence of this peak indicates the photocatalytic production of H_2O_2 (Equation 3.1) The RP/BP-Pt-PtP_2 photocatalyst is restricted in its ability to drive the water oxidation reaction because of its valence band potential, which is lower than the required minimum of 1.78 V [173]. Consequently, H_2O_2 can be generated through the oxygen reduction mechanism, which demands a potential of 0.68 V (Equation 3.3), as our photocatalyst possesses a conduction band potential below this value [174]. However, for the oxygen evolution reaction to occur via water splitting, a photocatalyst with a valence band potential of at least 1.23 V is necessary. In our case, the RP/BP-Pt photocatalyst only has a valence band potential of 1.01 eV, which falls short of the required potential for oxygen evolution [175]. Thus, the oxygen evolution reaction can proceed only in the presence of dissolved oxygen in water. Despite the limitation imposed by the energy level requirement on the valence band potential of

BP-based photocatalysts, their role in photoredox catalytic processes for H_2O_2 reactions can be explored. Considering all this information, in addition to photocatalytic water splitting for hydrogen atom transfer reactions, water can also transfer its hydrogen atoms to substrates via the hydrogen peroxide production pathway,

$$H_2O_{2(aq)} + 3I^-_{(aq)} + 2H^+ \rightarrow {I_3}^-_{(aq)} + H_2O \quad (3.1)$$

$$H_2O \rightarrow H^+OH^- \quad (3.2)$$

$$O_2 + 2H^+ + 2e^- \rightarrow H_2O \quad (3.3)$$

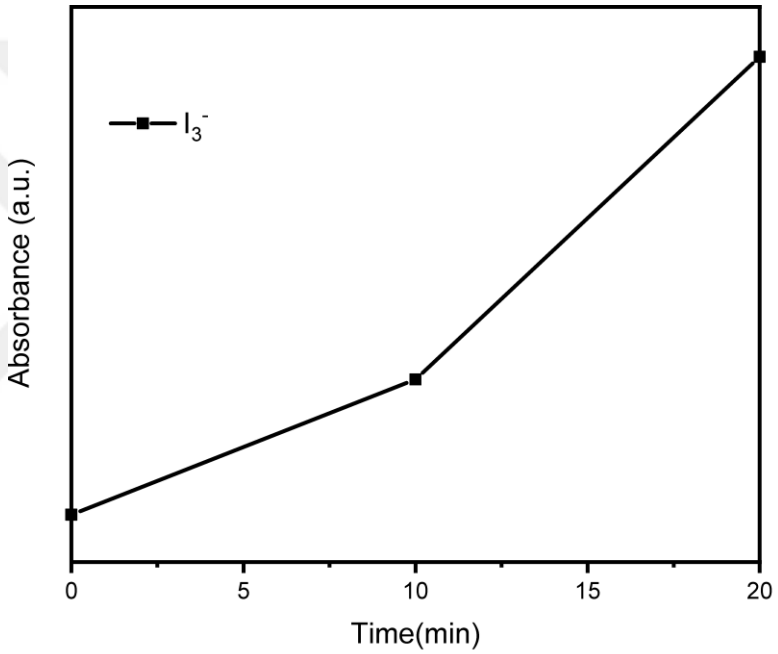

Figure 3.14. Absorption spectra of I_3^-

In Section 1.7.1, the proposed mechanisms for the hydrogenation of nitrobenzene are outlined. Among these, the Haber mechanism, which is still widely accepted today, describes two pathways for the reduction of nitrobenzene to aniline: a direct pathway via NSB and PHA and an indirect pathway where NSB and PHA combine to form AOB, AZB, HAB, and finally, aniline. Other proposed mechanisms suggest that intermediate products such as NSB or PHA do not form, and the processes involved in this mechanism continue to be a subject of debate today. To confirm whether one of the intermediate products is NSB, nitrobenzene was reacted under standard reaction conditions along with

aniline. The complete consumption of aniline and the formation of AOB confirm that NSB is an intermediate product. Under standard reaction conditions, 100 mg of 2,2',6,6'-tetramethylpiperidine N-oxyl (TEMPO) was employed as a hydrogen atom scavenger and reacted with nitrobenzene. The presence of TEMPO inhibits the formation of PHA, thereby preventing any product transformation. This observation indicates that the reaction proceeds via adsorbed hydrogen atoms rather than molecular H_2 derived from water splitting, and it also demonstrates the presence of PHA as the second intermediate [139]. Following this, 1,4-benzoquinone (BQ) was introduced as an electron scavenger to the reaction mixture to examine the influence of electrons on the reaction mechanism. The complete inhibition of the reaction emphasizes the critical role of electron transfer in the reduction process of nitrobenzene. These results indicate that electron and proton transfers are indispensable factors for reducing nitrobenzene, consistent with the mechanisms proposed in the literature.

Chapter 4 :
TANDEM PHOTOCATALYTIC HYDROGEN EVOLUTION AND SELECTIVE REDUCTION OF NITROARENES USING RP/Pt and RP/Pd HETEROJUNCTION PHOTOCATALYSTS

4.1. Introduction

Chapter 3 discusses the synthesis, characterization and the photocatalytic activity of the RP/BP-Pt heterojunction photocatalysts in the photocatalytic HER and nitrobenzene reduction reactions. The synthesis procedure of the heterostructure, supported by numerous characterization studies, enabled the formation of BP crystals and Pt nanoparticles within an autoclave heated to 180°C in the presence of EDA as a chelating agent and DMF solvent. However, challenges arose during the characterization of the synthesized structure because of its complex nature, such as observing the formation of different species rather than a homogeneous phase within the heterostructure.

In this chapter, we propose the RP/Pt structure synthesis based on the synthesis procedure shown in Chapter 2, **Figure 2.2**. This proposed synthesis procedure for RP/Pt offers a much more accessible and convenient approach for the in-situ formation of Pt nanoparticles compared to the procedure suggested for RP/BP-Pt. The photocatalytic HER activity of the RP/Pt catalyst, synthesized through a more straightforward procedure, significantly surpassed that of the RP/BP-Pt-PtP_2 heterostructure. In addition, a one-pot tandem nitrobenzene reduction reaction was conducted alongside the photocatalytic HER activity of the RP/Pt catalyst.

Moreover, Pd metal is known for its superior performance in hydrogenation studies, synthesized using the method indicated in Chapter 2, **Figures 2.3** and the HER and hydrogenation activities were compared. The synthesized heterostructures were characterized using various characterization techniques.

4.2. Results and Discussion

4.2.1. RP/Pt photocatalysts

The RP/Pt catalysts were synthesized following the synthesis procedure described in Chapter 2, Figure 2.2. Catalysts with 3, 5, 7, and 10 wt % Pt theoretical loading ratios were synthesized. First, the photocatalytic HER activity of these catalysts was investigated in the presence of TEOA as a hole scavenger and EY as a light sensitizer. The RP/Pt catalyst with an experimental loading ratio of 2.70 wt% Pt exhibited the highest HER activity compared to RP and all other synthesized materials (Experimental ratios calculated by ICP-MS are provided in parentheses, **Figure 4.1a**). Subsequently, the photocatalytic HER activities of the pristine RP, BP, and RP/BP-Pt, as well as the RP/BP-Pt_u and RP/BP-Pt_b catalysts discussed in the previous section were compared with these newly synthesized RP/Pt catalysts.

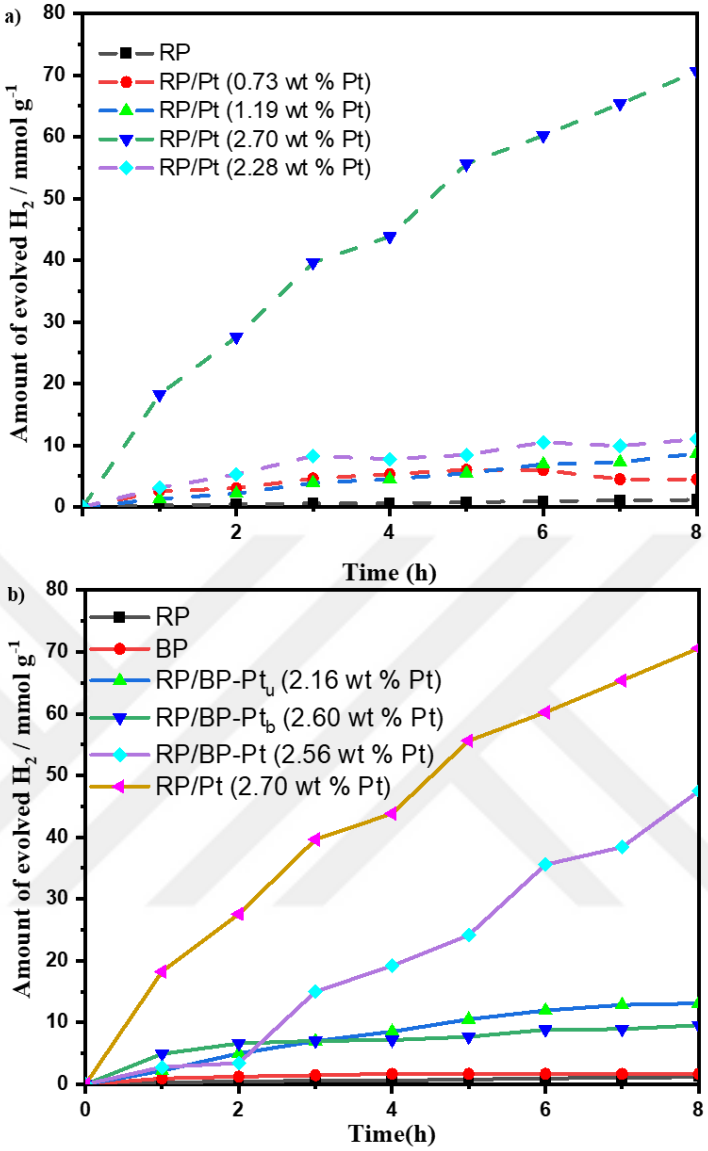

Figure 4.1. a) Photocatalytic HER activities with different Pt loading ratios, b) Photocatalytic activities of RP,BP, RP/Pt, RP/BP-Pt, RP/BP-Pt_u and RP/BP-Pt_b,

The RP/Pt catalyst, synthesized via a novel and simplified method, demonstrated higher activity in HER applications than all previously investigated catalysts. (**Figure 4.1.b**) After observing its high activity, the structure of this catalyst was elucidated by using various advanced instrumental techniques.

Using the same synthesis method and keeping the Pt amount same (theoretical loading of 7 wt % Pt), Pt NPs were synthesized within crystalline BP as well. The HER activity of this newly prepared catalyst was then compared with that of RP/Pt. It was

observed that RP/Pt exhibited significantly higher HER activity than BP/Pt. This indicates that RP is a more suitable semiconductor material for HER in the presence of the Pt NPs (**Figure 4.2**).

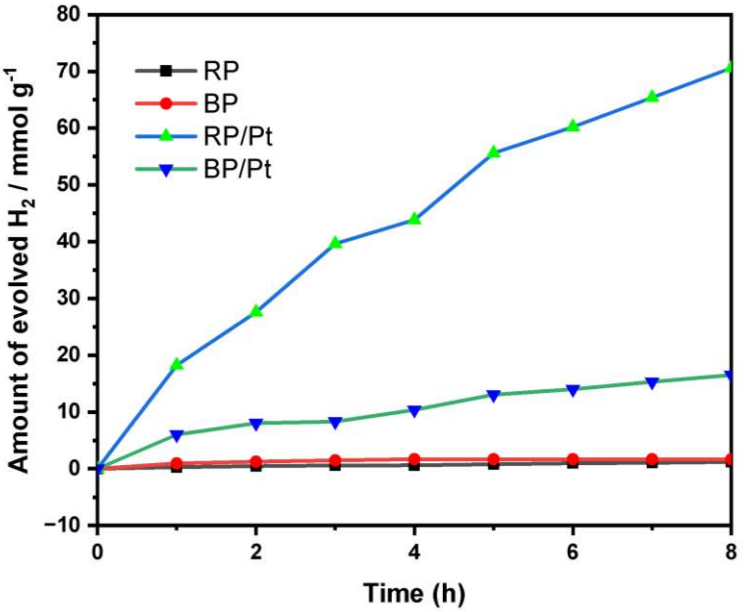

Figure 4.2. Photocatalytic HER activities of RP,BP,RP/Pt and BP/Pt.

Figure 4.3 shows the XRD patterns of RP and RP/Pt. Amorphous RP exhibits three diffraction peaks at 2θ = 15°, 32° and 55° [176]. The synthesized RP/Pt structure maintains the amorphous nature of RP while exhibiting diffraction peaks at 2θ = 15°, 33°, and 60°. A noticeable shift towards higher 2θ degrees is observed compared with RP. However, no diffraction peaks corresponding to Pt were observed. According to XRD principles, for a substance to exhibit diffraction peaks, it generally needs to have a minimum mass of 3-5 wt% [146]. Because of the low loading ratio of Pt (2.70 wt%) and their small particle size in this case, no diffraction peak attributed to Pt is observed in the XRD pattern. In addition, the diffraction peaks of Pt may be obscured by the amorphous nature of RP. Confirmation of the presence of Pt NPs was achieved through HR-TEM analysis (vide infra).

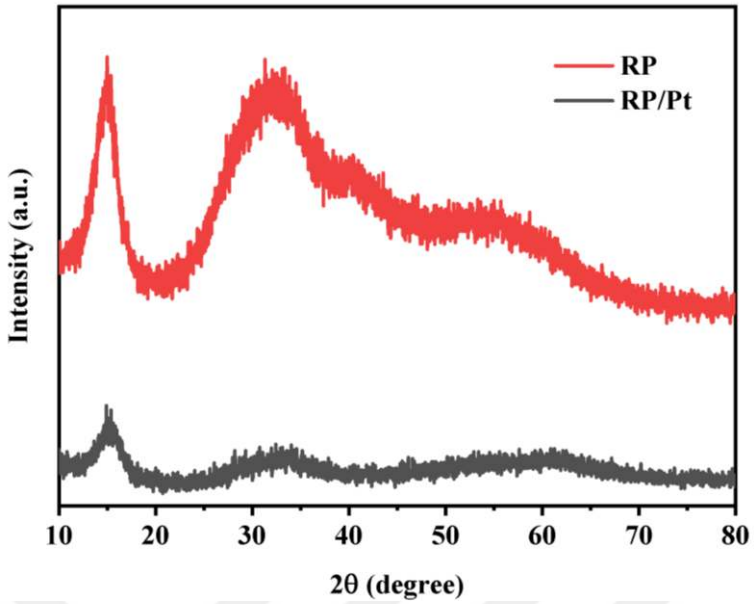

Figure 4.3.XRD pattern of RP and RP/Pt (2.70 wt % Pt).

The morphological characteristics of RP/Pt are depicted in the TEM and HR-TEM images in **Figure 4.4**. While the layered structure of RP is preserved, a more uniform thickness than that of RP is noted in the following synthesis. The uniform distribution of Pt NPs on the RP is obvious.(**Figure 4.4.**a-b) **Figure 4.4.c** illustrates the HR-TEM image of RP/Pt. The inset indicates the average particle size obtained from the HR-TEM image. The particle size of the Pt NPs was calculated to be 2.4 nm. **Figure 4.4.d** illustrates the HR-TEM image of RP/Pt, the presence of Pt NPs was confirmed by inverse-fast-fourier-transform (IFFT) analysis, which corresponds to the (111) plane of fcc Pt with a calculated lattice distance of 0.226 nm [177].

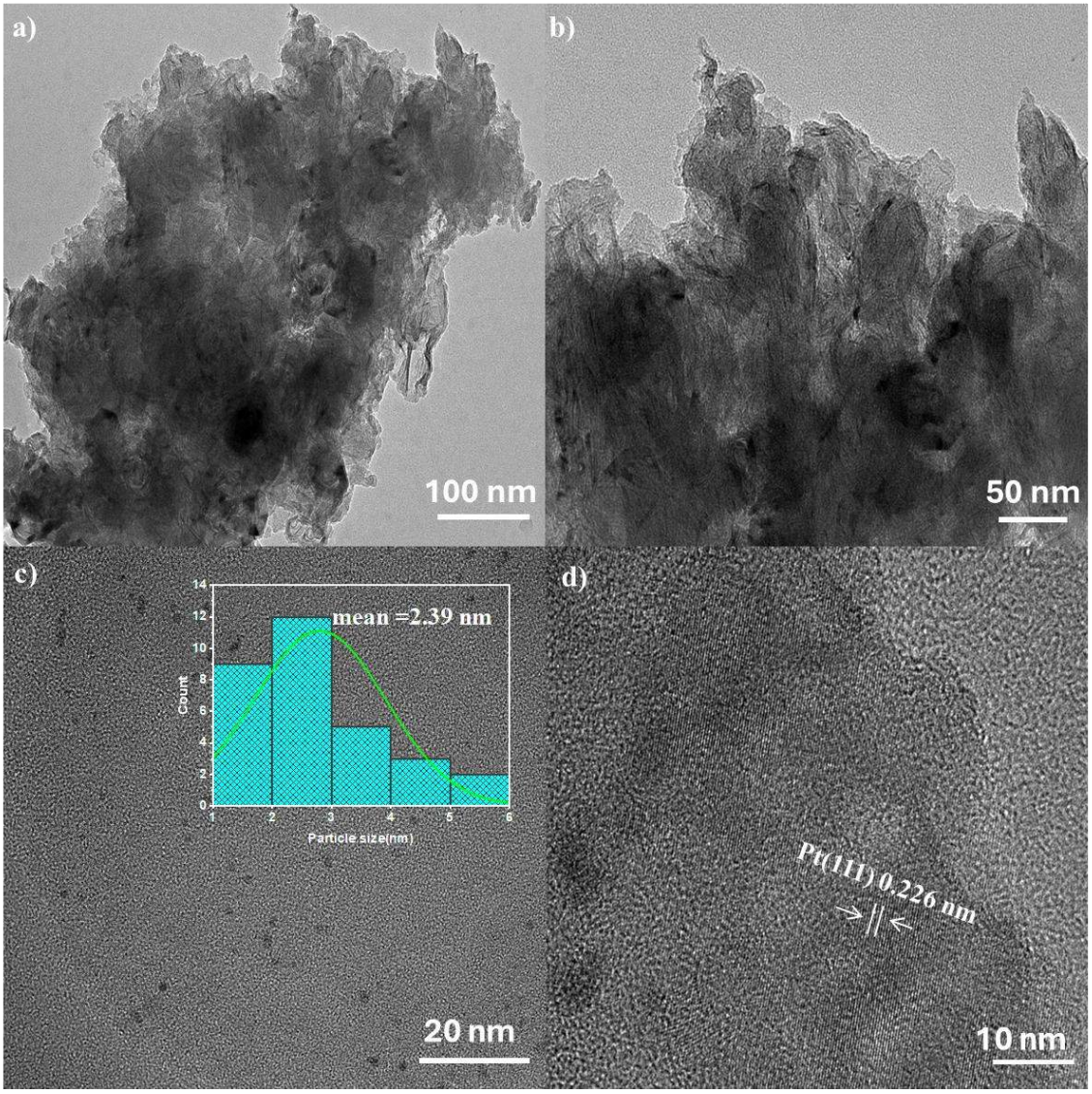

Figure 4.4. a,b,)TEM images of RP/Pt, c,d)HR-TEM image of RP/Pt (2.70 wt% Pt).

The HAADF-STEM and the associated elemental mapping images illustrate the distribution of elements constituting the heterostructure (**Figure 4.5**). This analysis also confirms the uniform distribution of Pt NPs on RP. The coverage of the structure by the oxygen indicates the oxidation of the RP surface.

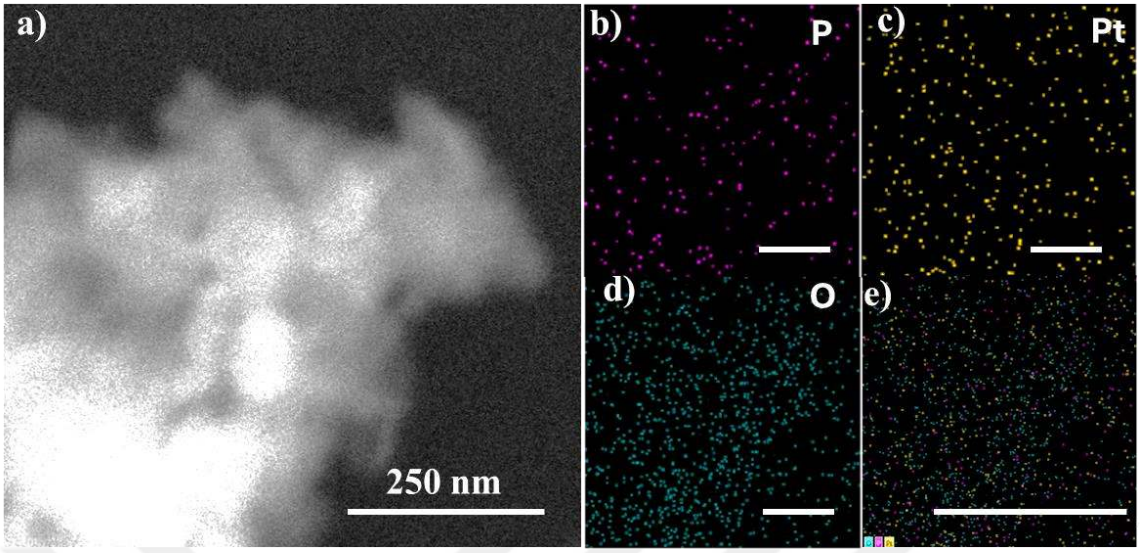

Figure 4.5.a) HAADF-STEM image, b-e) Elemental mapping images of RP/Pt (Scale bar=250 nm for b-e).

The surface chemistry of the materials was investigated using XPS analysis. The XPS survey spectrum indicates the following elements constituting the material: P, Pt, and O (**Figure A.4**). In the high-resolution P2p XPS spectrum of RP/Pt, the peaks observed at binding energies of 129.3 and 130.3 eV correspond to the $P2p_{3/2}$ and $P2p_{1/2}$ core levels of the elemental P atom, respectively.(**Figure 4.6.a**) These peaks exhibit a shift of approximately 0.4 eV towards higher binding energy than those observed at 128.9 eV and 129.9 eV for the elemental P's $P2p_{3/2}$ and $P2p_{1/2}$ core levels in RP. This shift signifies the electron flow from P to Pt. It denotes the electronic interaction between the two elements, indicating the construction of a Schottky junction in the RP/Pt structure [178]. The peak at 133.2 eV demonstrates the P-O bond resulting from oxidation on the material surface. **Figure 4.6.**b shows the Pt4f spectrum. Two doublet pairs at 71.1 eV - 74.4 eV and 72.2 - 75.8 eV indicate the oxidation states of Pt as Pt(0) and Pt(II), respectively [179]. This suggests that Pt(IV) ions have been partially reduced, indicating the predominance of metallic Pt NPs.

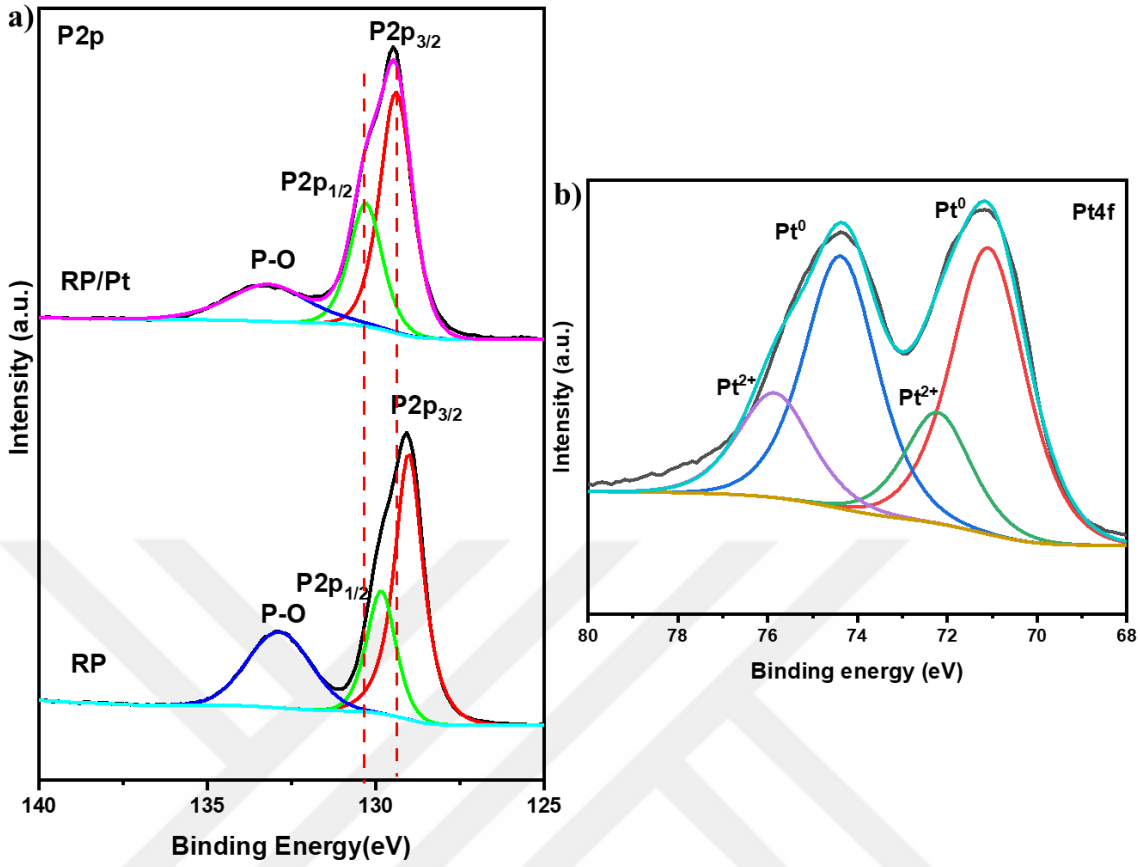

Figure 4.6. HR-XPS spectra of RP/Pt, a) P2p spectra, b) Pt4f spectra.

The absorption properties of RP and RP/Pt were investigated using UV-Vis DRS. (**Figure 4.7a** and **b**) The observed reflectance data were converted to the absorption spectrum using the Kubelka-Munk function. RP/Pt exhibits a strong absorption capability shifting toward the NIR region. **Figure 4.7.b** shows the DRS spectrum, where the Tauc plot analysis were conducted considering that RP is a direct band gap semiconductor. The region where the graph intersects the x-axis gives the semiconductor's band gap. It was found that RP/Pt (1.95 eV) possesses similar band gap compared to RP (1.95 eV), while both materials exhibit similar light absorption behavior. The charge carrier behaviors of the materials were measured by PL and TRPL analyses. A decrease in PL intensity was observed in RP/Pt compared with that in RP. This decrease in PL intensity indicates that after the interaction of RP and Pt, Pt acts as an electron trap center, hindering the transfer of electrons from the metal back to RP. This prevents the recombination of electrons with holes on RP, implying the establishment of a Schottky junction between RP and Pt. (**Figure 4.7.c**) Additionally, the average lifetime (τ_{ave}) of charge carriers in RP/Pt (12.4

µs) shows a slight decrease compared to RP (14.7 µs) (**Figure 4.7d**). The average lifetime decrease is expected situation in Schottky junction indicating available new paths that accelerate charge transfer from the semiconductor to metal [180].

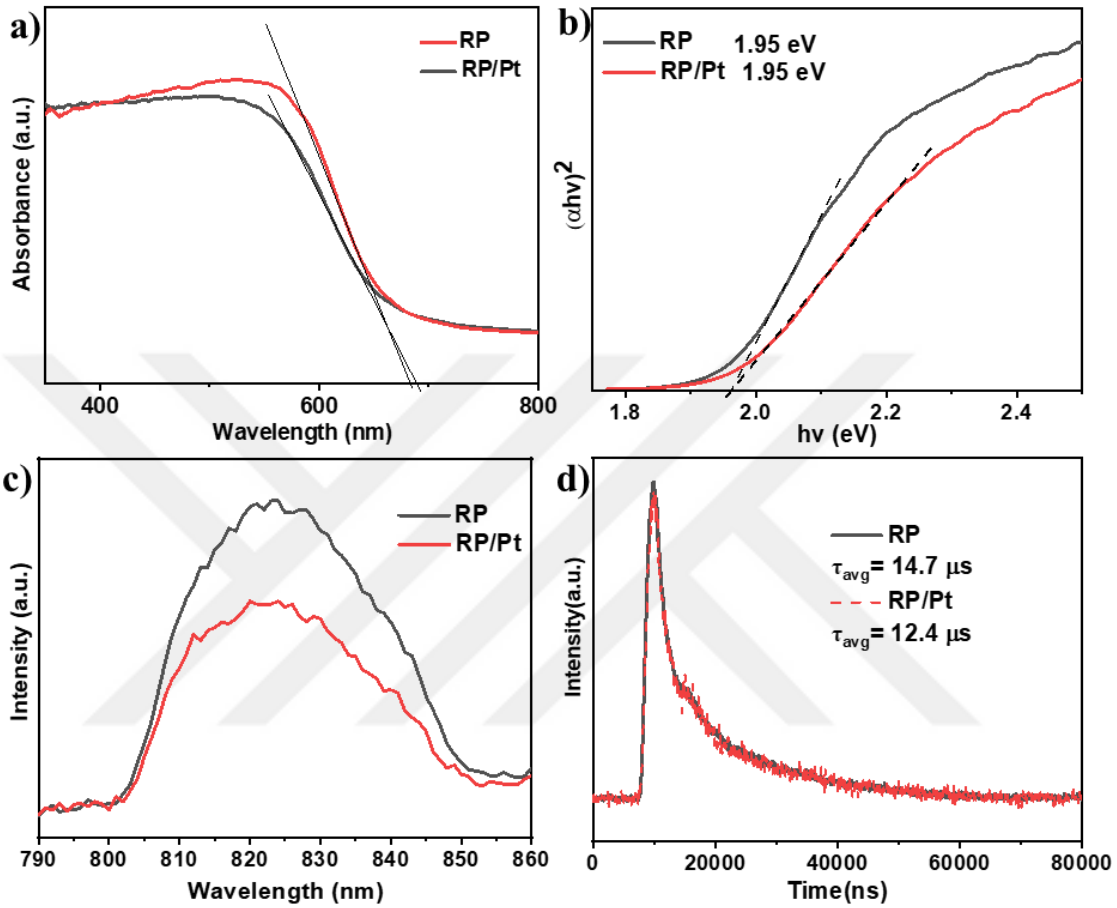

Figure 4.7.a)UV-Vis-DRS spectra, b) Tauc plot analysis, c)PL emission, d)lifetime of RP/Pt(2.70 wt% Pt).

4.2.2. RP/Pt Catalyzed Photocatalytic Tandem HER and Hydrogenation of Nitrobenzenes

The catalytic activity of RP/Pt in the tandem photocatalytic and hydrogenation of nitrobenzenes in one-pot using water as a hydrogen source was investigated. It should be noted that the conversion (C%) refers to the conversion of nitrobenzene substrates to the products with respect to the the internal standard. The selectivity (S%) expresses the ratio of a desired product (e.g. aniline) with respect to the other products yielded (**Table 4.1**). **Table 4.1** entry 1 highlights the significance of employing light sources with varying

power in the reaction medium. In the experiment utilizing a 24 W White LED, the conversion value was notably low, at 10% within 20 hours reaction time. Since HER conditions were performed using EY as a photosensitizer and TEOA as a hole scavenger, these two components were also integrated into the nitrobenzene reaction. Here, in the experiment without a catalyst, the conversion was 40%, and aniline selectivity was 30% (**Table 4.1.** entry 2). In the presence of RP/Pt catalysts, the conversion and aniline selectivity of the substrate were measured as 81% and 41%, respectively (**Table 4.1.** entry 3). The reaction was carried out in an oil bath at 100 ^{0}C for 20 h to observe the thermal effect in the presence of RP/Pt catalyst and EY was not used in this non-light experiment. (**Table 4.1.** entry 4) Even at high temperatures and long reaction times, the conversion of nitrobenzene did not occur. This indicates that the reaction proceeds through the photocatalytic pathway. An increase in conversion and selectivity rate was observed by increasing the reaction time from 6 h to 8 h, so the optimized conditions were set at 8 hours. (**Table 4.1.** entry 5). In the experiment with pristine RP, the selectivity towards aniline was measured to be 40%. (**Table 4.1.** entry 6)

Table 4.1. Optimization of the reaction conditions

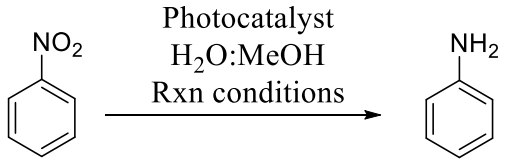

Entry	Catalyst	Hole Scav.	Light senst.	Light source	Time(h)	Temp(°C)	C (%)	S (%)
1	RP/Pt	TEOA	EY	White LED(24 W)	20	RT	10	
2	-	TEOA	EY	White light(150W)	6	RT	40	30
3	RP/Pt	TEOA	EY	White light	6	RT	81	41
4	RP-Pt	TEOA	-	-	20	100	trace	
5	RP/Pt	TEOA	EY	White light	8	RT	92	50
6	RP	TEOA	EY	White light	8	RT	90	40

Reaction conditions: 0.25 mmol nitrobenzene,10 mg photocatalyst, EY(3.25 × 10-4 M), TEOA(5%), H2O: MeOH(10:3), Numerical values are calculated by GC-MS using 1,3-dinitrobenzene as internal standard. C:Conversion, S:Selectivity to aniline.

When evaluating the conversion and selectivity values resulting from the reaction mixture, it is evident that the selectivity towards aniline differs, indicating the presence of other products in addition to the target compounds. As explained in the previous sections, the formation of by-products in addition to aniline significantly affects the selectivity of the reaction, as outlined by the Haber mechanism, which is one of the most widely accepted mechanisms proposed for the nitrobenzene reduction. The low selectivity towards aniline suggests the coexistence of azoxybenzene (AOB) and azobenzene (AZB) in the reaction mixture (**Figure 4.8**).

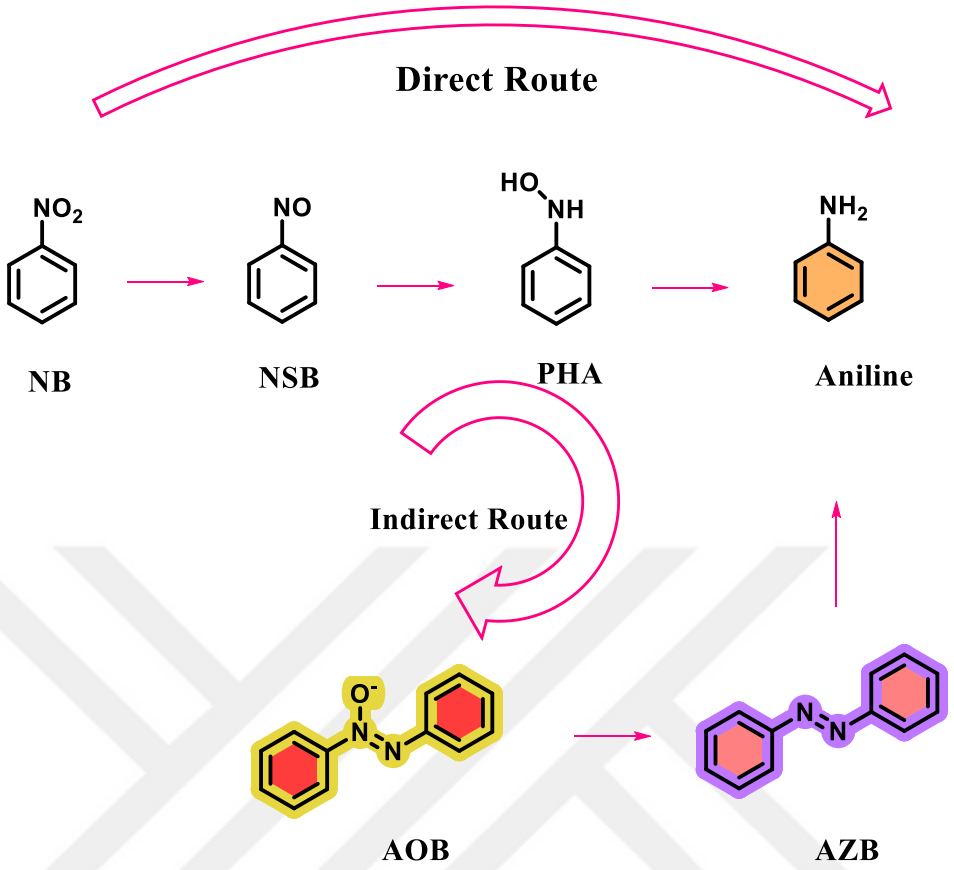

Figure 4.8. A proposed reaction mechanism and possible products

With the optimum reaction conditions in hand, substrate-scope of RP/Pt catalyzed tandem photocatalytic HER and hydrogenation of nitrobenzenes was studied over 15 different nitrobenzene derivatives (**Table 4.2**). Conversion values were supported bilaterally by GC-MS and NMR. Halogenated nitrobenzene derivatives readily undergo dehalogenation (**Table 4.2.,** compound **2** and **3**), but the product mixture could not be fully elucidated because side products other than the dehalogenated product were also observed [144]. It was observed that the nitrobenzene derivative containing Br at the m-position was reduced entirely, but the aniline selectivity was almost negligible. Similarly, other by-products, along with the aniline derivative, were observed (**Table 4.2**, compound **15**). When utilizing 1-fluoro-4-nitrobenzene (**Table 4.2**, compound **7**), an aniline derivative was achieved with superior conversion (89%) and notably high selectivity (86%) compared to other nitrobenzene derivatives bearing a halogenated substituent at the para position. In the presence of the large-sized nitrobenzene compound

1-nitronaphthalene, remarkable conversion and selectivity were obtained. (**Table 4.2, compound** 10, C:80-85%, S:>99) When the analysis results were evaluated, compared to the excellent HER performance of RP/Pt, it was observed that its performance was limited in terms of nitrobenzene reduction and its performance in reducing different nitrobenzene derivartives.

Hydrogenation reactions, described in Section 1.7, mention the parameters that affect their performance. As mentioned before, metals such as Pt and Pd are known for their superior performance in hydrogenation reactions. However, the different electronic properties of these metals ensure that their catalytic properties in the reactions are different. The position of the d-band centers of the metals determined by theoretical studies determines their adsorption with the substrate [181]. For example, Pt and Pd's d band center positions are reported to be -2.2 and -1.8 eV, respectively [182]. When Pt interacts with H, the bonding and antibonding levels are below the fermi level, the antibonding levels are filled with electrons, and the interaction of the Pt surface with H is reduced. Therefore, while Pt is the preferred catalyst for H evolution because of its electronic properties, the weak interaction of H with the metal may create an undesirable effect for hydrogenation. Because the reported d band center level of Pd remains above the fermi level, the antibonding level formed when H interacts with the Pd surface remains well above the fermi level, which strengthens the Pd-H adsorption. In this case, although Pd shows limited activity for HER, the hydrogenation performance will be stronger than that of Pt [183]. Considering all these parameters, the RP/Pd catalyst was synthesized using the method mentioned in section 2.4 to better understand the relationship between HER and hydrogenation. The performance of this catalyst in HER and hydrogenation reactions was investigated.

Table 4. 2. Substrate scope study of RP/Pt

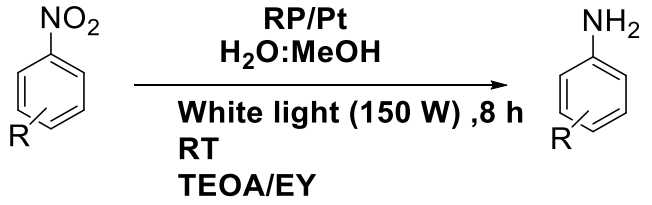

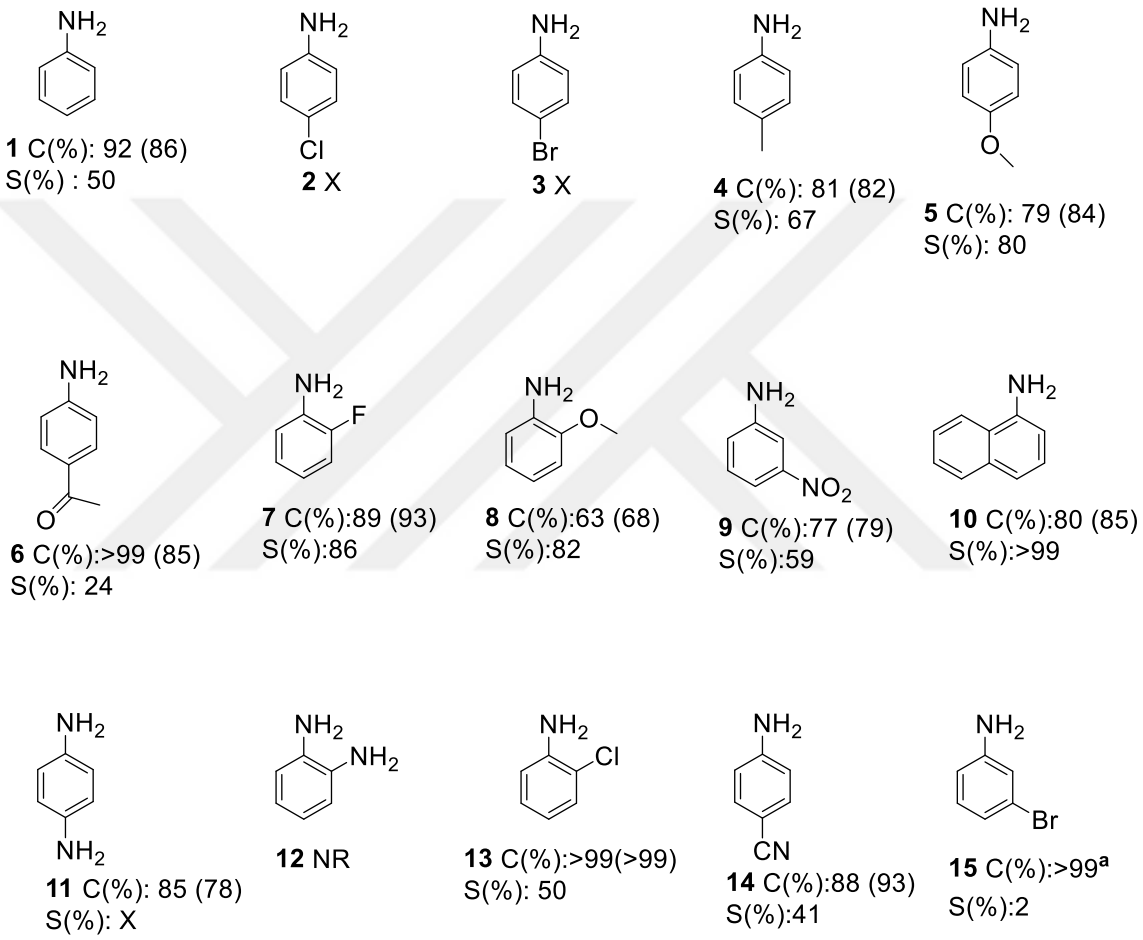

Reaction conditions: 0.25 mmol nitrobenzene,10 mg photocatalyst, EY(3.25 × 10-4 M), TEOA(5%), H_2O: MeOH(10:3), Conversion values were calculated by GC-MS and NMR using 1,3-dinitrobenzene as the internal standard. The GC-MS conversion value is outside the brackets, and the NMR conversion value is in brackets. C(%):Conversion, S(%):Selectivity to aniline. NR:No reaction, X:Not identified. Selectivity was determined by assessing the ratio between the yield of the desired product and the detected by-products. a=Conversion value obtained from the H-NMR due to the overlap of substrates in the GC-MS

4.2.3. RP/Pd photocatalysts

Keeping the amount of metal constant in synthesized catalysts while evaluating their

comparative activities in the same reactions is an accurate approach. In this respect, the RP/Pd catalyst was synthesized by using a similar synthesis method of RP/Pt, except using K_2PdCl_4 as the Pd precursor, and keeping the metal loading same as RP/Pt. The experimental Pd ratio in RP/Pd was calculated as 2.40 wt % by ICP-MS analysis.

The photocatalytic HER activity of RP/Pd was studied in the presence of hole scavenger TEOA and light sensitizer EY. Since all synthesized catalysts did not show activity without EY, the light sensitizer is a necessary parameter in HER applications. It was observed that RP/Pd exhibited higher performance than pristine RP and BP, while RP/Pd demonstrated lower HER activity compared to all Pt-based catalysts. This outcome aligns with expectations, that Pt-based catalysts are benchmark in HER applications (**Figure 4.9**).

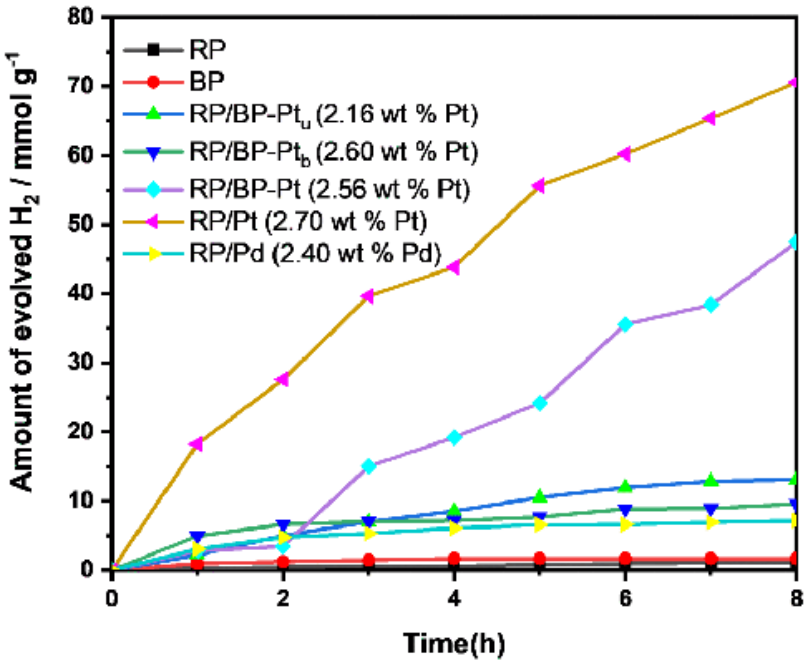

Figure 4.9. Photocatalytic HER performance of all catalysts.

XRD pattern of RP/Pd was analyzed (**Figure 4.10**). The broad peaks of RP observed at 2θ = 15.6° and 32.7° reveal the amorphous structure of commercial RP.[184] The diffraction peaks at 2θ = 40.3° and 46.7° correspond to the (111) and (200) planes of fcc metallic Pd, respectively. (JCPDS card no: 05-0681) [185]. The peaks displayed in the XRD pattern indicate that Pd nanoparticles can be successfully synthesized in RP.

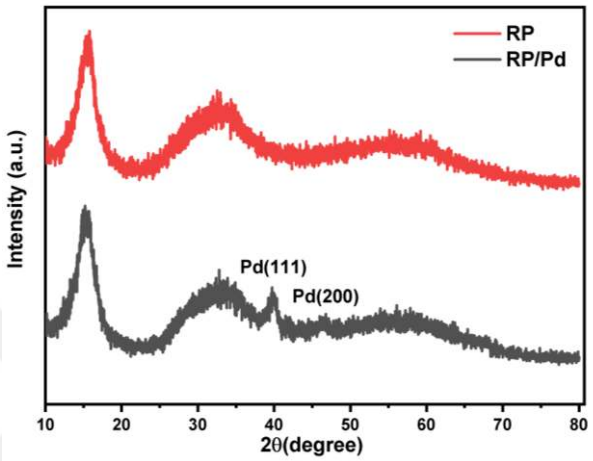

Figure 4.10. XRD pattern of RP and RP/Pd.

The morphological properties of RP/Pd were examined using TEM analysis (**Figure 4.11a-b**). Similar to RP, the material has a layered structure with varying thicknesses. Since the presence of Pd NPs in TEM images could not be confirmed, HR-TEM analysis was performed (**Figure 4.11c-d**). White dots in the HR-STEM dark field image indicate the presence of Pd Nps. The average particle diameter of Pd NPs for 40 points selected from the HR-STEM image was calculated as 1.75 ± 0.13 nm by size distribution histogram (**Figure 4.11e**). The ultrasmall size of the particles prevents their visualization in TEM analysis. The presence of Pd NPs, shown in the HR-TEM image (**Figure 4.11.d**), was confirmed by the lattice spacing of 0.226 nm calculated by IFFT analysis and corresponding to the (111) plane of fcc Pd [186]. HAADF-STEM image and EDX elemental mapping images (**Figure 4.11f-i**) were used to visualize the presence and distribution of the elements forming the heterostructure. While the presence of oxygen(O) shows the oxidation of RP/Pd, the uniform distribution of Pd NPs on RP is displayed and demonstrates the formation of the RP/Pd structure.

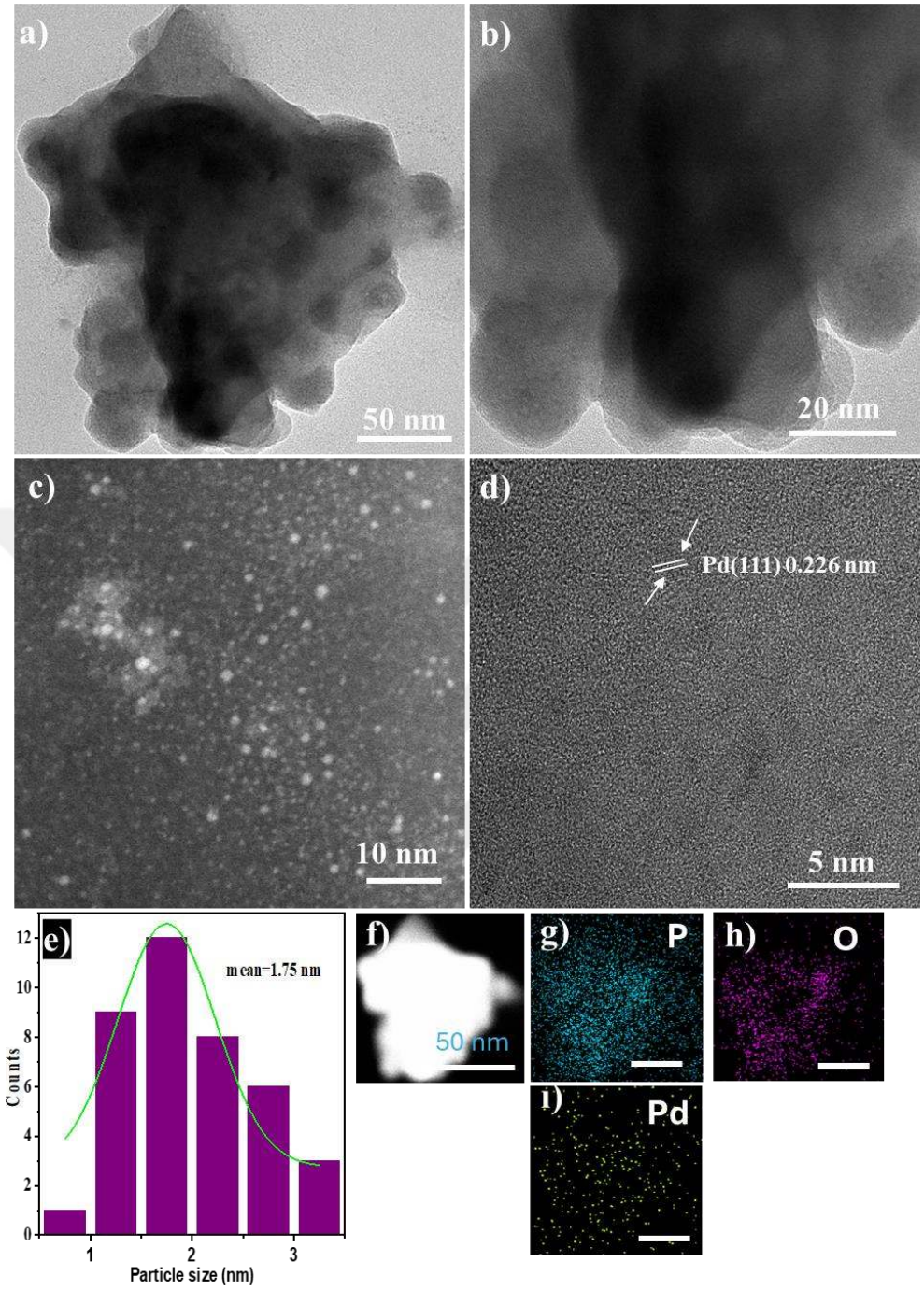

Figure 4.11.a-b) TEM images, c) HR-STEM dark field image, d) HR-TEM image, e)Pd NP size histogram, f)HAADF-STEM image, g-i) EDX elemental mapping images of RP/Pd (2.40%Pd) (scale bar=100nm)

The chemical state of the elements on the surface and their interactions with each other were investigated by HR-XPS analysis (**Figure 4.12**). The presence of the elements (P, Pd, O) forming the heterostructure was observed by XPS survey spectra (**Figure A.5**). In the P2p spectrum, peaks corresponding to the $P2p_{3/2}$ and $P2p_{1/2}$ core levels of elemental P of RP were observed at 129.1 and 129.9 eV, respectively. Peaks corresponding to the $P2p_{3/2}$ and $P2p_{1/2}$ core levels of RP/Pd were observed at 129.3 and 130.1 eV, respectively, showing a shift in binding energy about 0.2 eV higher than that of RP. This change in binding energy indicates that P gives its electrons to Pd and the interaction of P with Pd [187]. Peaks observed at approximately 132.7 and 133.6 eV due to the oxidation of RP surface, indicating P-O bonding, were also observed at 133.1 and 134.2 eV in RP/Pd and shifted to high binding energies. When the HR-XPS of Pd3d was analyzed, it was observed to be separated into two doublet pairs. The peaks of zero-valent Pd were observed at 335.8 and 341 eV, whereas those associated with Pd^{2+} species were observed at 336.9 and 342 eV referring to the unreduced Pd(II) species. The higher intensity of Pd NPs compared with Pd(II) indicates that the synthesis method successfully forms Pd NPs.

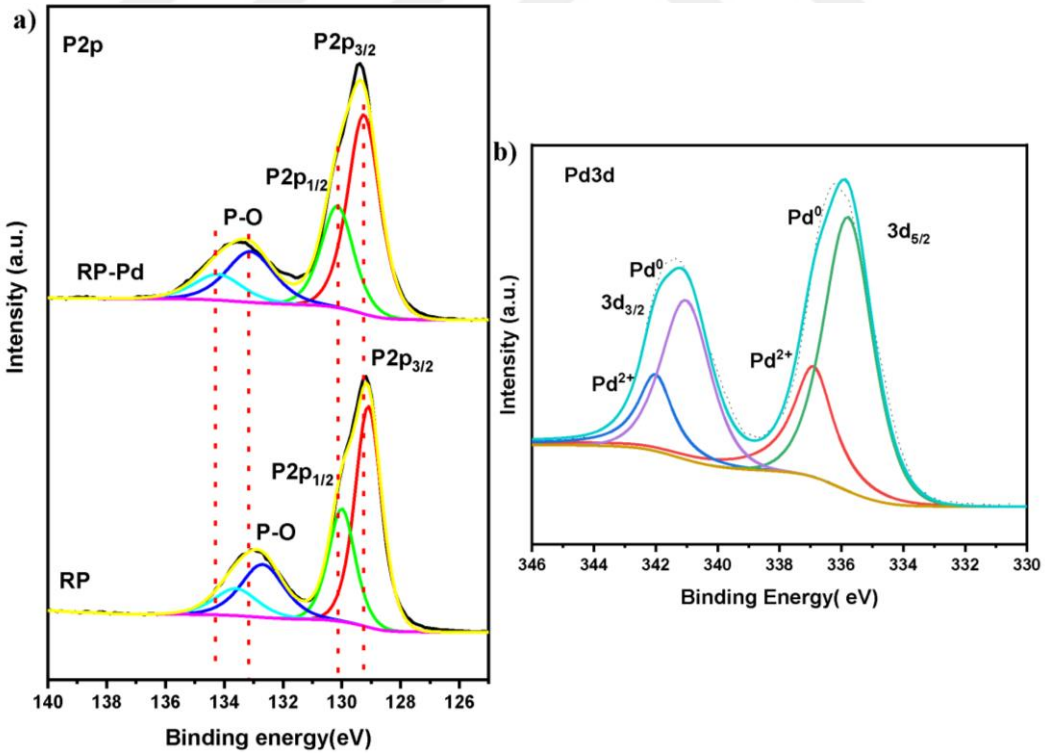

Figure 4.12.HR-XPS spectra of RP/Pd, a) P2p, b) Pd3d spectra.

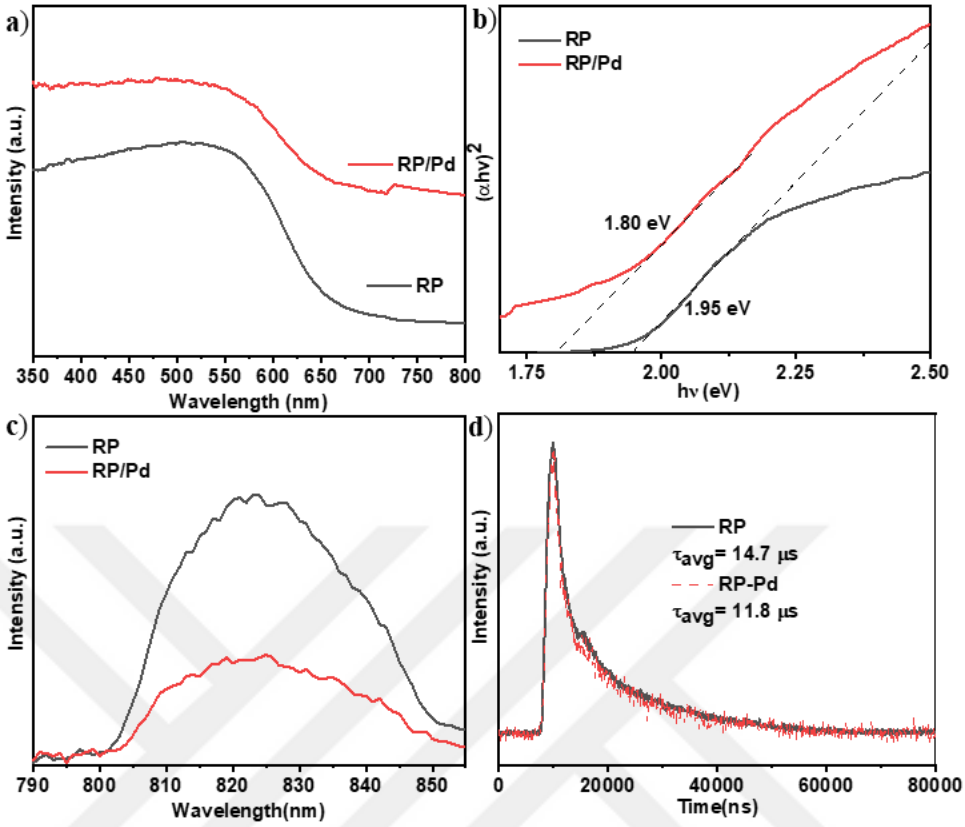

Figure 4.13. a)UV-Vis-DRS spectra, b) Tauc plot analysis, c)PL emission, d)lifetime of RP/Pd (2.40 wt% Pd).

The optical properties of RP and RP/Pd were investigated through UV-Vis DRS and Tauc plot analysis (**Figure 4.13a-b**). To elucidate the light absorption behavior, reflectance data were transformed into absorption data utilizing the Kubelka-Munk function. Notably, the absorption edge of RP/Pd exhibited a red shift accompanied by broader light absorption compared to RP, with a discernibly upgraded absorption intensity. Moreover, employing Tauc plot analysis facilitated the determination of the direct optical band gap values, yielding 1.95 eV for RP and 1.80 eV for RP/Pd. Insights into charge carrier dynamics were collected through PL and TRPL investigations (**Figure 4.13c-d**). The reduction in PL emission observed in RP/Pd relative to RP suggests a directional flow of electrons from the semiconductor to the metal upon Pd incorporation, consequently diminishing radiative electron-hole recombination (**Figure 4.13.c**) [188]. In TRPL analysis, the average charge lifetimes were quantified in the microsecond (μs) range via excitation with a 377 nm light source and subsequent biexponential fitting.

Notably, RP/Pd exhibited a shorter average lifetime (11.8 μs) than RP (14.7 μs), indicative of accelerated charge transfer facilitated by Schottky junction within RP/Pd.(**Figure 4.13.d**)

4.2.4. RP/Pd Catalyzed Photocatalytic Tandem HER and Hydrogenation of Nitrobenzenes

The catalytic activity of RP/Pd in the tandem HER and hydrogenation of nitrobenzenes in one-pot using water as a hydrogen source was investigated in a similar way to RP/Pt. Experiments were conducted using the optimum reaction conditions obtained for the RP/Pt catalyst. In **Table 4.3**, when indicating C:Conversion, the conversion values outside the brackets were obtained from GC-MS, and those inside the brackets were obtained from H-NMR, and the data were supported bilaterally. The conversion values were calculated by consuming nitrobenzene against the 1,3-dinitrobenzene internal standard. Selectivity values were calculated based on the target product and the formed by-products.

Excluding groups bearing halogens at the para position, numerous nitrobenzene derivatives have exhibited the capability to undergo reduction with high conversion and selectivity, resulting in the desired product—aniline derivative. While the reduction of derivatives (**Table 4.3** compound **2,3**) bearing Cl and Br at the p-position of nitrobenzene compounds predominantly results in dehalogenation products, a mixture of AOB, AZB, and HAB types, which are reduction products of nitrobenzene has also been observed. Hence, reporting these compounds' conversion and selectivity values was not feasible. There are several interpretations regarding when dehalogenation occurs. It can be proposed that the nitrobenzene derivative initially undergoes dehalogenation. Alternatively, dehalogenation may occur after the formation of the aniline derivative. It has been suggested that the electron-donating amino group in the aniline derivative donate electrons to the benzene ring and make the halogen more electron-rich. Thus, after the aniline derivative's formation, halogen removal may be facilitated [189]. In the presence of an electron-donating amino group, the para and ortho positions will have a higher electron density than the meta position. Thus, compounds bearing halogenated groups at these positions may undergo more dehalogenation. However, for compound **13**, it has

been observed that high selectivity (82%) for the aniline derivative can be achieved in the presence of Cl at the ortho position. The increased susceptibility of molecules to dehalogenation, especially in the presence of Cl and Br as good leaving groups at the para position, may be attributed to their relative distance from steric effects compared to the ortho position, rendering the reaction to proceed more quickly. For compound **7**, where fluorine is located at the ortho position, excellent conversion and selectivity in obtaining aniline derivatives have been achieved, and since fluorine (F) is the least reactive halogen substituent, no dehalogenation product or other side products were observed. The reaction outcomes varying with the positions of halogens led us to conduct an additional experiment to investigate this intriguing observation. When the reaction was carried out with the RP/Pd catalyst, the nitrobenzene compound underwent reduction with 90% selectivity, producing aniline (**Table 4.3** compound **1**). This time, chlorobenzene was reacted with nitrobenzene under standard reaction conditions. Contrary to the initial observation, only trace amounts of aniline were detected. This result suggests that when a nitrobenzene compound with a halogen in the para-position approaches the phosphorus surface, the distance prevents hydrogen atoms on the metal surface(hydride) from effectively transferring to the nitrobenzene. In contrast, the relatively higher selectivity for aniline production observed with halogens in the ortho or meta positions indicates that the hydrogen atoms can be more easily transferred to the nitrobenzene compound (**Table 4.3** compound **7** and **13**). Similar to the issue encountered in halogen-containing nitrobenzene compounds, if there are reducible groups other than nitrobenzene in the compound, the reduction of both nitrobenzene and other groups can result in undesired by-products.[134] In the reduction of 4-nitrobenzonitrile (**Table 4.3** compound **14**), the selectivity towards the aniline derivative was low (21%); other by-products were formed wherein the amine derivative formed through the reduction of the nitrile group, as well as intermediates such as NSB, PHA, and AOB resulting from the reduction of nitrobenzene, may interact with each other to form new intermediates.

In the reduction of the 1-nitronaphthalene compound (**Table 4.3** compound **10**), it was observed that the considerable molecule size of the nitrobenzene derivative did not impede its reduction to the intended aniline product, demonstrating exceptional conversion and selectivity. Another experimental result demonstrating the effect of

substituent position on the reaction outcome is investigated with reactants **11** and **12**. While p-nitroaniline yields the aniline derivative as the sole product with good conversion and superior selectivity, ortho-nitrobenzene remains unreacted, with no observed reaction occurring (**Table 4.3** compound **11** and **12**).

After analyzing the reaction outcomes, it was discovered that the RP/Pd catalyst could attain noteworthy conversion and selectivity when reducing numerous nitrobenzene derivatives to the desired aniline derivatives. Furthermore, it displayed superior performance in nitrobenzene reactions compared to RP/Pt. Upon evaluating the hydrogen evolution reaction (HER) and hydrogenation results it became evident that RP/Pt exhibited superior performance in HER. However, the performance in tandem photocatalytic nitrobenzene hydrogenation experiments, influenced by the HER results, needed to be improved. Despite RP/Pd showing HER performance at approximately one-tenth of the activity of RP/Pt, it outperformed RP/Pt in hydrogenation performance. These exciting results encouraged us to elucidate the relationships between HER and hydrogenation reactions, and a series of mechanistic studies were carried out.

Table 4.3. Substrate scope study of RP/Pd

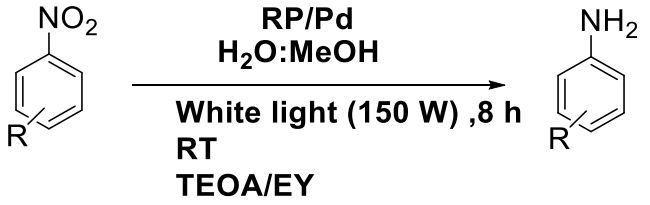

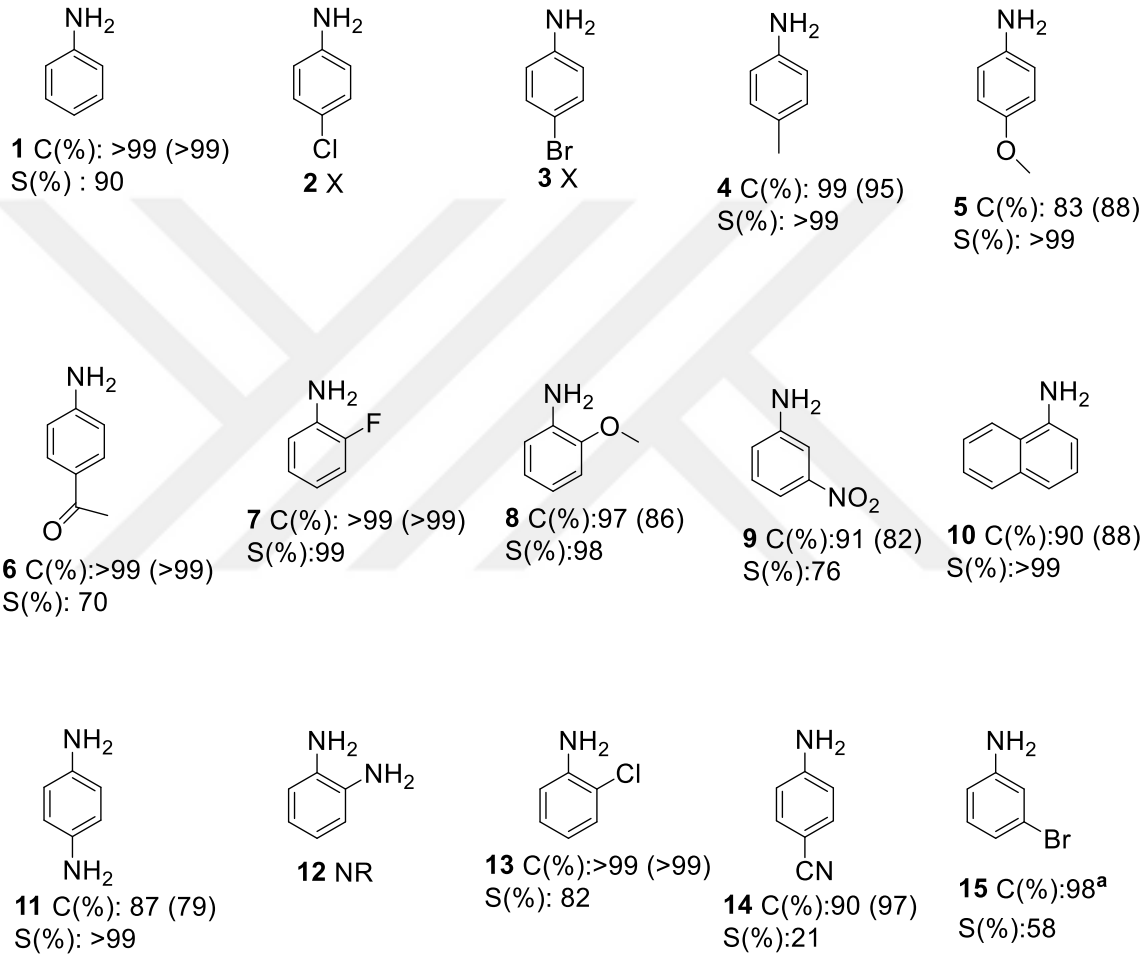

Reaction conditions: 0.25 mmol nitrobenzene,10 mg photocatalyst, EY(3.25×10^{-4} M), TEOA(5%), H_2O: MeOH(10:3), Conversion values were calculated by GC-MS and NMR using 1,3-dinitrobenzene as the internal standard. The GC-MS conversion value is outside the brackets, and the NMR conversion value is in brackets. C(%):Conversion, S(%):Selectivity to aniline. NR:No reaction, X:Not identified. Selectivity was determined by assessing the ratio between the yield of the desired product and the detected by-products. a=Conversion value obtained from the H-NMR due to the overlap of the peaks associated with the substrates in the GC-MS

With its high hydrogen affinity (280 kJ/mol), TEMPO has a strong tendency to capture hydrogen atoms [190]. The mechanism of the hydrogenation reaction was investigated

using TEMPO as a hydrogen atom scavenger in the RP/Pd and RP/Pt catalyzed reactions. In experiments conducted under standard reaction conditions in the presence of 100 mg (2 equivalents) of TEMPO, the conversion of nitrobenzene was inhibited entirely, and no products were observed. The capture of the hydrogen atom prevented the formation of PHA and all subsequent products. This result indicates that the hydrogenation reaction occurs through active hydrogen species generated by water reduction rather than molecular H_2 from water splitting. The hydrogen evolution reaction (HER) experiment was conducted under identical reaction parameters with the addition of nitrobenzene to further support this claim (**Figure 4.14**). For both RP/Pd and RP/Pt catalysts, nitrobenzene was observed to quench the HER activity significantly. More specifically, when photoelectrons reach the metal surface, they reduce protons to form atomic hydrogen. Under normal conditions, these hydrogen atoms combine to form H_2 gas, facilitating the HER. However, in the presence of nitrobenzene, the atomic hydrogen reduces the nitrobenzene, suppressing the HER. This inverse relationship between the two reactions indicates that nitrobenzene competes for the atomic hydrogen species, thus inhibiting the HER. Nitrobenzene reduction experiment was performed for both RP/Pt and RP/Pd under standard reaction conditions in the presence of BQ as an electron scavenger [191]. No product conversion was observed at the end of the experiment, indicating the inevitable role of electrons and adsorbed hydrogen species in the reaction.

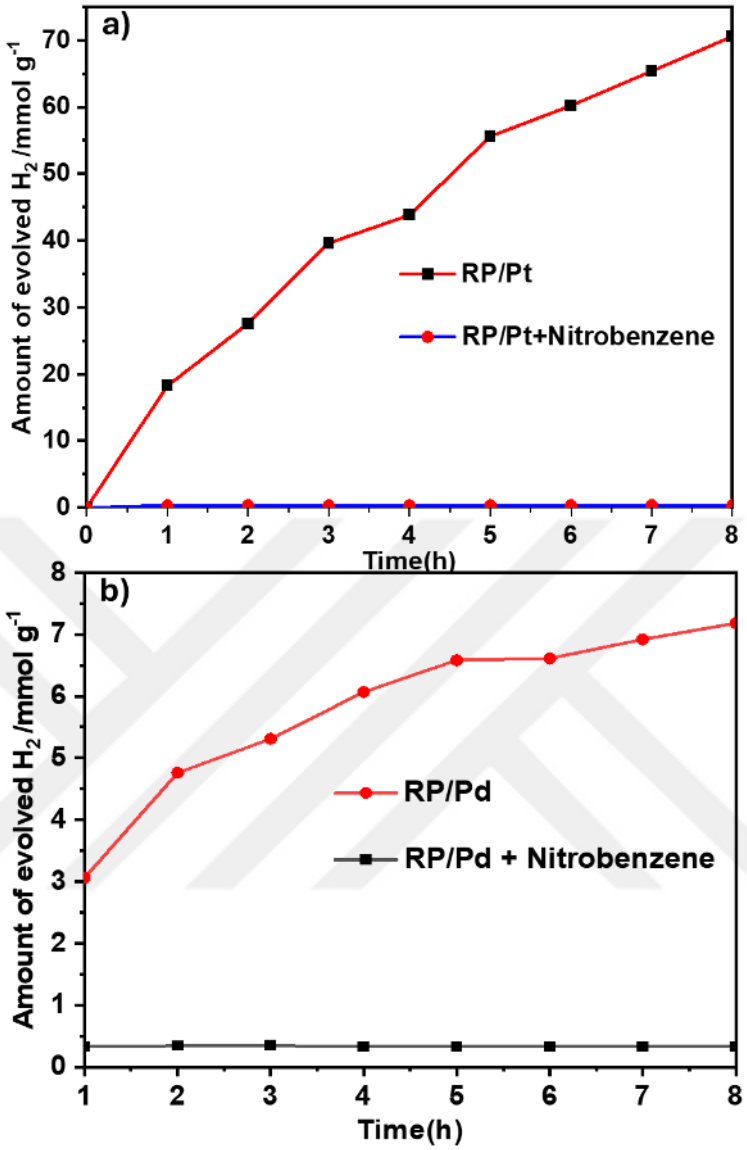

Figure 4.14. HER and hydrogenation relationship.

An isotope-labeling experiment was performed by keeping the reaction conditions constant to determine the source of hydrogen in nitrobenzene hydrogenation. Using H_2O, mass spectrometry identified aniline at m/z = 93.13. When D_2O was used, the peaks associated with the deuterated-aniline shifted to m/z = 94.15 and 95.15 (**Figure 4.15**). These shifts indicate the H-D exchange and confirm that the hydrogen source for the transfer hydrogenation predominantly originates from water.

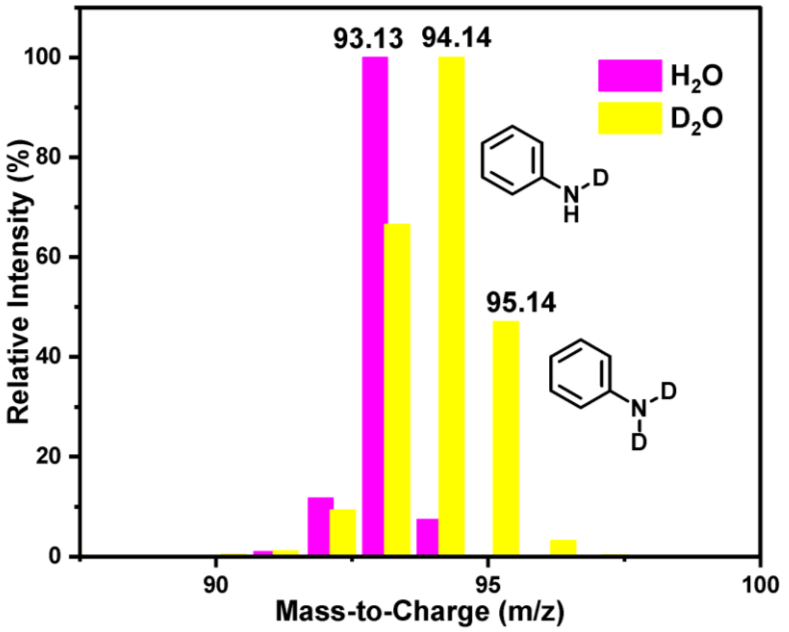

Figure 4.15. Mass spectra of the nitrobenzene hydrogenation product using H_2O and D_2O.

Mott-Schottky analyses were conducted to calculate the conduction band level of the semiconductor at three different frequencies (1000, 1500, and 2000 Hertz) (**Figure 4.16**). The RP's flat band potential (Efb) was determined to be -0.79 V vs. Ag/AgCl from the point where the Mott-Schottky plot intersects the x-axis. The flat band energy (Efb) vs. Ag/AgCl was converted to the standard hydrogen electrode (NHE) using the formula $E_{NHE} = E_{Ag/AgCl} + 0.197$ [192]. The positive slopes of the Mott-Schottky plots indicate that RP is an n-type semiconductor. For n-type semiconductors, the calculated E_{fb} is equivalent to the Fermi level (E_{fl}). Therefore, the E_{fl} of RP is found as -0.59 V vs. NHE. It is also known that the conduction band potential (E_{CB}) of an n-type semiconductor is approximately 0.1 V more negative than the E_{fl} [193]. Consequently, the E_{CB} of RP is

calculated to be -0.69 V vs. NHE. Using the band gap value (Eg) and the calculated E_{CB} ; the valence band potential (E_{VB}) was determined using the equation $E_g=E_{VB}-E_{CB}$. With these energy band values, the photocatalytic mechanism for RP and its composites with Pt, Pd, and Ru was proposed to better understand the Mott-Schottky kinetics.

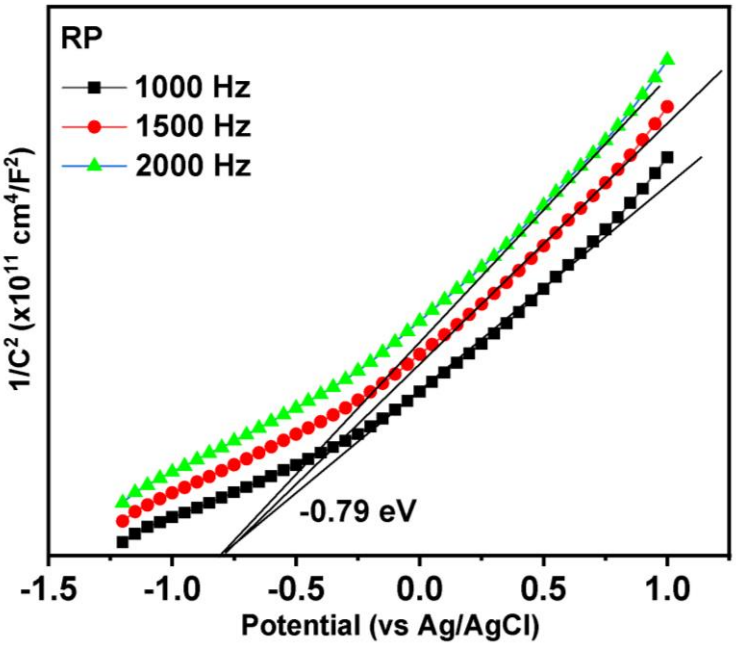

Figure 4.16. The Mott-schottky plot of RP.

After calculating the energy band values, schematic illustration for the band structures was proposed to elucidate the charge transfer between the metal and semiconductor (**Figure 4.17**). Noble metals are known for their high work functions. Based on the literature data; Pt and Pd exhibit higher work functions and lower Fermi levels than the semiconductor RP [194; 195]. When the n-type semiconductor RP interacts with these metals, an internal electric field is established at the interface due to the difference in Fermi levels, causing electrons to flow from the RP to the metal surface. This electron transfer occurs because the Fermi level of the semiconductor is higher than that of the metal. As electrons migrate from RP to the metal, the region near the interface in RP becomes electron-deficient, creating an electron-poor zone. This results in upward band bending in the semiconductor's conduction band near the interface. The continuous flow of electrons from the semiconductor to the metal forms a potential barrier at the interface, known as the Schottky barrier. This barrier prevents the backflow of electrons

from the metal to the semiconductor. The formation of the Schottky barrier is critical as it enhances the separation of charge carriers by hindering their recombination. The metal surface, now rich in electrons, becomes an active site for reduction reactions. The accumulated electrons on the metal surface facilitate the reduction of H^+ ions to H_2 gas, or they may interact with the substrate molecules to perform hydrogenation reactions on the metal surface.

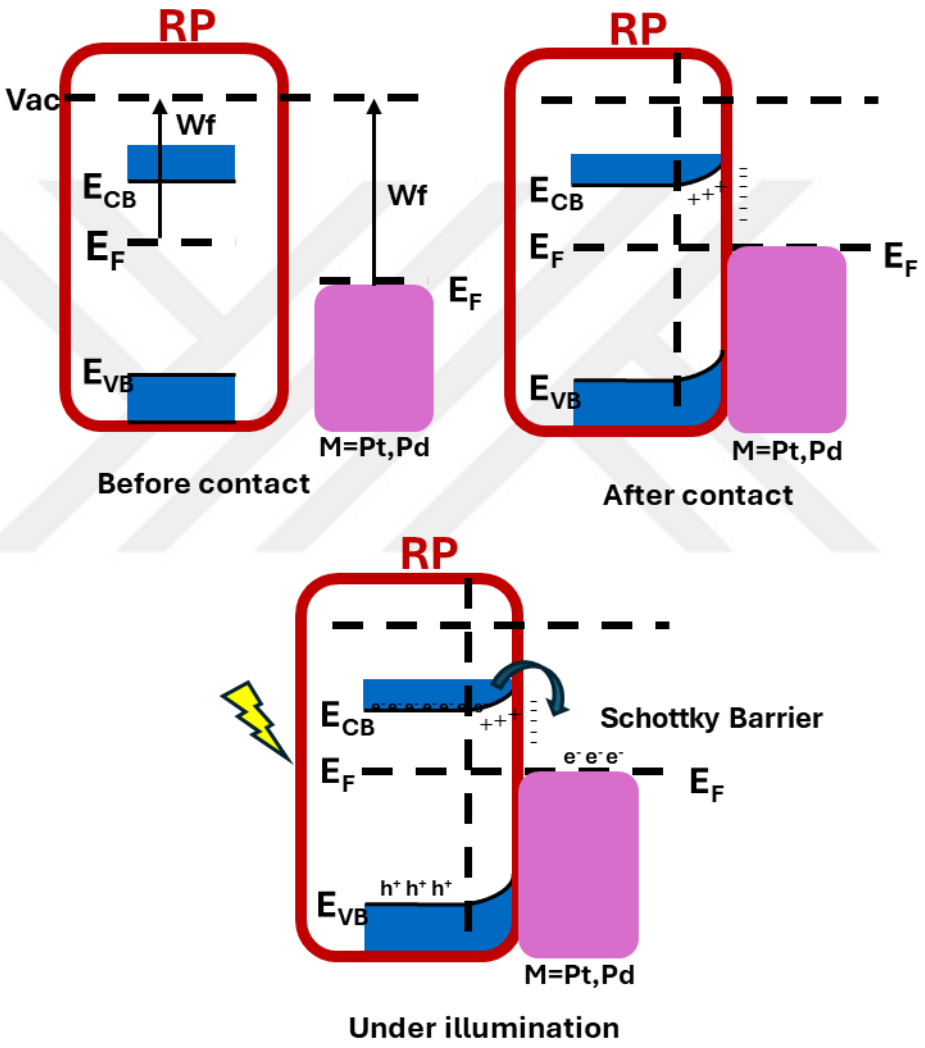

Figure 4.17. Schematic illustration of the band structure, a)before contact, b)after contact, c)under illumination.

Table 4.4 presents the performance of RP/Pt and RP/Pd photocatalysts in reducing 15 different nitrobenzene derivatives. The conversion values for each catalyst

were determined using H-NMR and GC-MS analyses, and the average values are reported as conversion percentages. Examination of the data reveals that the catalytic activity of RP/Pt in the reduction of nitrobenzenes is lower than that of RP/Pd. For substrates with Cl and Br substituents in the para-position (**Table 4.4,** compound **2** and **3**), a mixture of dehalogenation and nitrobenzene reduction products was observed, and all three catalysts failed to reduce these derivatives. Benzene-1,4-diamine (**Table 4.4,** compound **11**) could be obtained only in the presence of the RP/Pd catalyst. Overall analysis of all substrates showed that RP/Pd could convert ten substrates to the target product with high activity and selectivity. Regarding hydrogenation performance, RP/Pd was the most active catalyst. Conversely, when evaluated regarding hydrogen evolution reaction (HER) performance, the activity ranking was RP/Pt, and RP/Pd, respectively. The distinct differences suggest that the choice of catalyst may need to be tailored to specific reaction requirements. The results also provided insight into how the relationship between the support and metal influences the reaction dynamics.

Table 4.4. Comparison table of hydrogenation performance by RP/Pt and RP/Pd

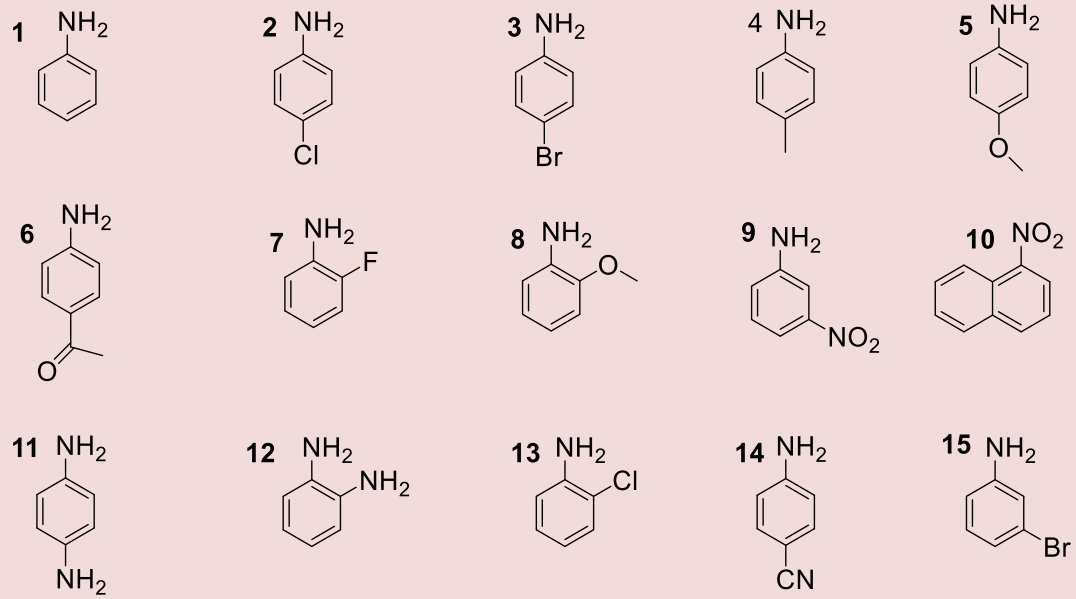

Substrate	RP/Pt C.(%)	RP/Pt S.(%)	RP/Pd C. (%)	RP/Pd S.(%)
1	89	50	>99	90
2	X	X	X	X
3	X	X	X	X
4	82	67	97	>99
5	81	80	86	>99
6	92	24	>99	70
7	91	86	>99	>99
8	65	82	92	98
9	78	59	87	76
10	83	>99	89	>99
11	81	X	82	>99
12	X	X	X	X
13	>99	50	>99	82
14	88	41	94	21
15	99	2	98	58

Reusability experiments

Reusability experiments were conducted to assess the durability of the catalysts (**Table 4.5**). During these experiments, catalyst loss occurred due to the washing

procedures required to prepare the catalyst for subsequent reaction. To mitigate this issue, the initial amount of catalyst was increased to 40 mg, deviating from the standard reaction conditions. However, this increase in catalyst quantity reduced the catalytic activity of the RP/Pd in the first experiment. The performance of all three catalysts exhibited a significant decline by the third cycle of the reusability tests. To investigate the cause of this pronounced decrease in activity, characterization studies were performed on these catalysts after reusability experiments. These studies aimed to elucidate the factors contributing to the observed degradation in catalytic performance.

Table 4.5. Reusability experiment

Catalyst	1st experiment Selectivity (%)	2nd experiment Selectivity (%)	3rd experiment Selectivity (%)
RP/Pt	58	52	32
RP/Pd	75	74	47

Reaction conditions: 0.25 mmol nitrobenzene,40 mg photocatalyst, EY(3.25×10^{-4} M), TEOA(5%), H_2O: MeOH(10:3)

The characterization studies of the catalysts after three experiments were conducted using X-ray diffraction (XRD) and X-ray photoelectron spectroscopy (XPS) analyses (**Figure 4.18** and **Figure A.6**). XPS analysis revealed that the peaks corresponding to oxidized phosphorus species remained unchanged, indicating that the observed decline in performance was not due to oxidation. Additionally, no changes were observed in the oxidation states of the metals. XRD analysis showed that the crystal structures of the catalysts did not undergo any significant structural changes. Based on these characterization data, it was concluded that the decrease in catalytic performance was primarily due to a substantial reduction in the amount of catalyst.

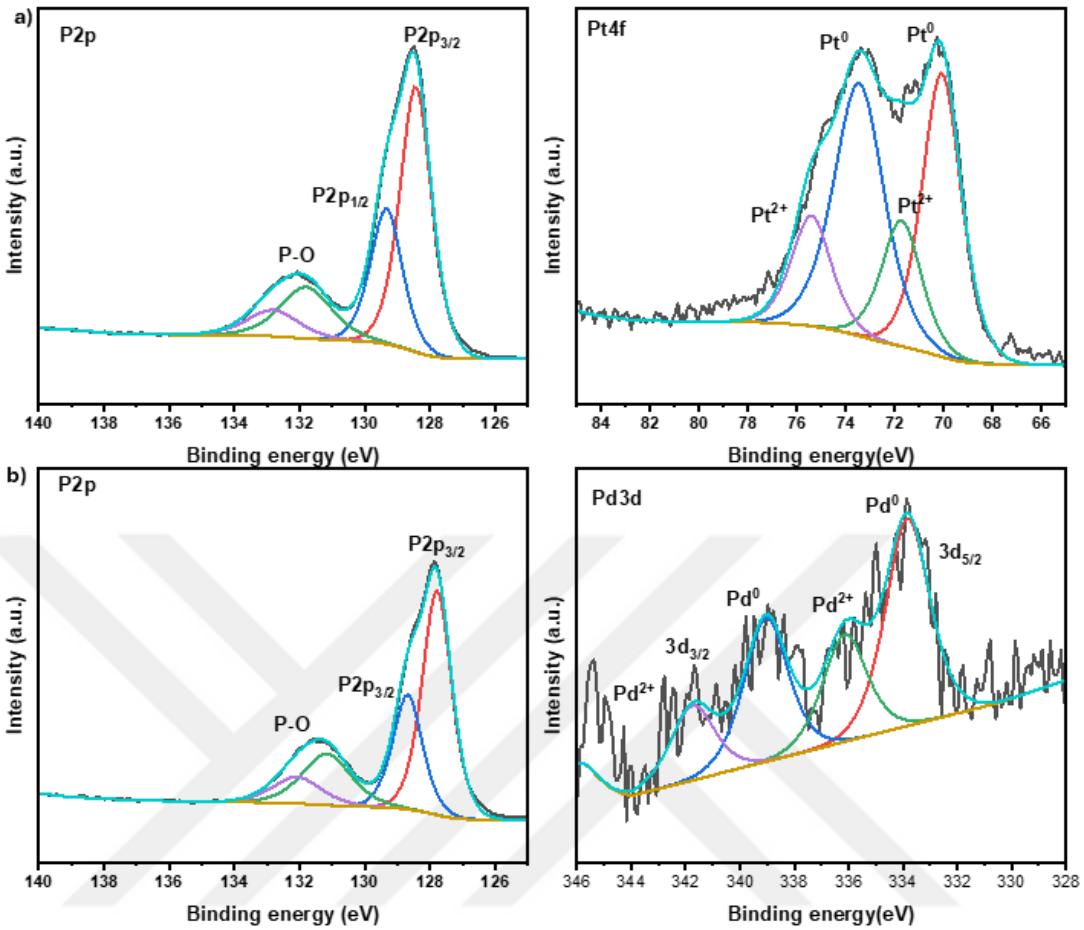

Figure 4.18. HR-XPS spectra of a)RP/Pt and b)RP/Pd after reusability study.

Chapter 5:

CONCLUSION

Part 1: TANDEM PHOTOCATALYTIC HYDROGEN EVOLUTION AND SELECTIVE REDUCTION OF NITROARENES USING RP-BP/Pt+PtP_2 HETEROJUNCTIONS

RP/BP-Pt+PtP_2 heterojunctions were synthesized from RP via a one-pot solvothermal synthesis method in the presence of ethylenediamine (EDA), dimethylformamide (DMF) and H_2PtCl_6 salt. The characterization of the synthesized structure, particularly through X-ray diffraction (XRD) analysis, indicated the presence of a minor peak corresponding to amorphous RP and shifted peaks indicative of orthorhombic BP. These findings led to the designation of the structure as RP/BP-Pt. Significantly, the synthesized catalyst exhibited two distinct phases: the upper phase (RP/BP-Pt_u), which was black and crystalline, resembled BP, and the lower phase (RP/BP-Pt_b), which was dark brown, reminiscent of RP.

Subsequently, the overall mixture and the separated upper and lower phases underwent detailed characterization. This meticulous analysis revealed the formation of PtP_2 NPs in addition to the Pt NPs. Notably, this study represents the first demonstration of PtP_2 synthesis from RP in the presence of Pt. The overall heterostructure, RP/BP-Pt, displayed superior hydrogen evolution reaction (HER) performance compared to the individual phases. This HER performance suggests the formation of a homojunction between the upper and bottom phases, wherein the interaction between the two phases enhances the overall HER activity.

The favorable photocatalytic HER results inspired us to integrate the photocatalytic HER concept with transfer hydrogenation to conduct one-pot transfer hydrogenation of nitroarenes in water as a hydrogen generator. By using the RP/BP-Pt-PtP_2 catalyzed tandem photocatalytic HER and the transfer hydrogenation of nitrorenes, several nitrobenzene derivatives were selectively reduced to azoxybenzene species. Deuterium labeling experiments confirmed that water served as the hydrogen source. The employment of water-derived hydrogen in transfer hydrogenation reactions is particularly

noteworthy in the context of green chemistry, as it enables the synthesis to occur under significantly milder conditions without using another hydrogen donor reagent and it provides atom economy and less chemical waste compared to the traditional hydrogenation and transfer hydrogenation protocols. This novel synthesis method offers a promising route for conducting transfer hydrogenation reactions with enhanced efficiency and reduced environmental impact, which is very important for the sustainable chemistry.

Part 2: TANDEM PHOTOCATALYTIC HYDROGEN EVOLUTION AND SELECTIVE REDUCTION OF NITROARENES USING RP/Pt and RP/Pd HETEROJUNCTION PHOTOCATALYSTS

In the previous section, the synthesized RP/BP-Pt heterojunctions exhibited significantly enhanced HER performance compared to the pristine RP. However, the synthesis method posed several challenges, primarily due to the use of ethylenediamine (EDA) as a chelating agent and the demanding solvothermal conditions. While the structure was comprehensively characterized, the characterization studies revealed the formation of complex species that were difficult to interpret and separate.

In the second part of the thesis, we explored the feasibility of forming Pt NPs in situ by introducing H_2PtCl_6 platinum source into commercially available and cost-effective RP through ultrasonication and following chemical reduction. Transmission electron microscopy (TEM) results confirmed the effective formation of Pt NPs using this method. Subsequently, the HER performance of the RP/Pt catalysts was evaluated with varying Pt ratios, demonstrating superior performance compared to both RP and the RP/BP-Pt heterostructures synthesized in the first chapter.

Given that all synthesized catalysts showed no activity in the absence of EY, HER experiments and one-pot tandem HER/nitrobenzene reduction experiments were conducted by incorporating EY into the reaction medium. Anticipating that the superior HER performance would translate into effective reduction of nitrobenzene derivatives, we performed hydrogenation experiments. Despite our expectations, the RP/Pt catalyst did not yield the desired outcomes in these hydrogenation experiments. Therefore, given the well-established hydrogenation performance of Pd, we incorporated Pd into our study.

The RP/Pd structure was synthesized using the same ultrasonication method as RP/Pt, and its HER activity was initially evaluated. It was observed that RP/Pd exhibited approximately one-tenth of the HER activity compared to RP/Pt.

Subsequently, we investigated the hydrogenation performance of RP/Pd in the reduction of 15 different nitrobenzene derivatives. The results indicated that RP/Pd showed significantly better hydrogenation performance than RP/Pt. These findings prompted us to conduct additional mechanistic experiments to explore the dynamics between HER and hydrogenation reactions. The experiments demonstrated that hydrogen atoms derived from water preferentially participate in hydrogenation when a substrate is present, thereby preventing HER. This indicates that HER and hydrogenation reactions are in direct competition. Deuterium labeling experiments confirmed that the primary source of hydrogen was water. The observed trend in hydrogenation performance, from highest to lowest, was RP/Pd > RP/Pt, while the HER performance exhibited the opposite trend.

This comprehensive study examined the reasons behind the distinct performances of these metals in HER and hydrogenation applications. The investigation of reaction dynamics provided valuable insights into the underlying mechanisms driving the catalytic behaviors of these metals in these two critical applications. Our findings highlight the competitive nature of HER and hydrogenation reactions and underscore the importance of selecting appropriate catalysts based on the specific requirements of each application. The hypotheses proposed in this thesis will be supported by ongoing computational studies currently in the initial stages, which aim to provide deeper insights into the different outcomes underlying the photocatalytic HER, thereby contributing to the advancement of the current knowledge.

BIBLIOGRAPHY

[1] Apak, S., Atay, E., & Tuncer, G. (2017). Renewable hydrogen energy and energy efficiency in Turkey in the 21st century. *International Journal of Hydrogen Energy*, *42*(4), 2446-2452.https://doi.org/10.1016/j.ijhydene.2016.05.043

[2] Shafiee, S., & Topal, E. (2009). When will fossil fuel reserves be diminished? *Energy Policy*, *37*(1), 181-189.https://doi.org/10.1016/j.enpol.2008.08.016

[3] Mohajan, H. K. (2017). Greenhouse gas emissions, global warming and climate change. Proceedings of the 15th Chittagong Conference on Mathematical Physics, Jamal Nazrul Islam Research Centre for Mathematical and Physical Sciences (JNIRCMPS), Chittagong, Bangladesh, https://doi.org/10.1149/2.F03152if

[4] Beland, L.-P., & Oloomi, S. (2019). Environmental disaster, pollution and infant health: Evidence from the Deepwater Horizon oil spill. *Journal of Environmental Economics and Management*, *98*, 102265.https://doi.org/10.1016/j.jeem.2019.102265

[5] Ramzan, M., Razi, U., Usman, M., Sarwar, S., Talan, A., & Mundi, H. S. (2024). Role of nuclear energy, geothermal energy, agriculture, and urbanization in environmental stewardship. *Gondwana Research*, *125*, 150-167.https://doi.org/10.1016/j.gr.2023.08.006

[6] Bai, L., Wang, X., Tang, S., Kang, Y., Wang, J., Yu, Y., Zhou, Z.-K., Ma, C., Zhang, X., Jiang, J., Chu, P. K., & Yu, X.-F. (2018). Black Phosphorus/Platinum Heterostructure: A Highly Efficient Photocatalyst for Solar-Driven Chemical Reactions. *Advanced Materials*, *30*(40), 1803641.https://doi.org/10.1002/adma.201803641

[7] Zainal, B. S., Ker, P. J., Mohamed, H., Ong, H. C., Fattah, I. M. R., Rahman, S. M. A., Nghiem, L. D., & Mahlia, T. M. I. (2024). Recent advancement and assessment of green hydrogen production technologies. *Renewable and Sustainable Energy Reviews*, *189*, 113941.https://doi.org/10.1016/j.rser.2023.113941

[8] Yoshida, T., & Kojima, K. (2015). Toyota MIRAI Fuel Cell Vehicle and Progress

Toward a Future Hydrogen Society. *The Electrochemical Society Interface*, *24*(2), 45.10.1149/2.F03152if

[9] Zhang, L., Jia, C., Bai, F., Wang, W., An, S., Zhao, K., Li, Z., Li, J., & Sun, H. (2024). A comprehensive review of the promising clean energy carrier: Hydrogen production, transportation, storage, and utilization (HPTSU) technologies. *Fuel*, *355*, 129455.https://doi.org/10.1016/j.fuel.2023.129455

[10] Rana, S., Kumar, A., Dhiman, P., Sharma, G., Amirian, J., & Stadler, F. J. (2024). Progress in graphdiyne and phosphorene based composites and heterostructures as new age materials for photocatalytic hydrogen evolution. *Fuel*, *356*, 129630.https://doi.org/10.1016/j.fuel.2023.129630

[11] Maeda, K., & Domen, K. (2010). Photocatalytic Water Splitting: Recent Progress and Future Challenges. *The Journal of Physical Chemistry Letters*, *1*(18), 2655-2661. https://doi.org/10.1021/jz1007966

[12] Li, Y., Ma, Z., Hou, S., Liu, Q., Yan, G., Li, X., Yu, T., Du, Z., Yang, J., Chen, Y., You, W., Yang, Q., Xiang, Y., Tang, S., Yue, X., Zhang, M., Zhang, W., Yu, J., Huang, Y., .Sun, K. (2024). Recent progress in hydrogen: From solar to solar cell. *Journal of Materials Science & Technology*, *176*, 236-257.https://doi.org/10.1016/j.jmst.2023.08.030

[13] Takata, T., Jiang, J., Sakata, Y., Nakabayashi, M., Shibata, N., Nandal, V., Seki, K., Hisatomi, T., & Domen, K. (2020). Photocatalytic water splitting with a quantum efficiency of almost unity. *Nature*, *581*(7809), 411-414. https://doi.org/10.1038/s41586-020-2278-9

[14] Chowdhury, P., Malekshoar, G., & Ray, A. K. (2017). Dye-Sensitized Photocatalytic Water Splitting and Sacrificial Hydrogen Generation: Current Status and Future Prospects. *Inorganics*, *5*(2). https://doi.org/10.3390/inorganics5020034

[15] Zhang, X., Peng, T., & Song, S. (2016). Recent advances in dye-sensitized semiconductor systems for photocatalytic hydrogen production [10.1039/C5TA08939E]. *Journal of Materials Chemistry A*, *4*(7), 2365-2402.

https://doi.org/10.1039/C5TA08939E

[16] Maeda, K., Eguchi, M., Youngblood, W. J., & Mallouk, T. E. (2008). Niobium Oxide Nanoscrolls as Building Blocks for Dye-Sensitized Hydrogen Production from Water under Visible Light Irradiation. *Chemistry of Materials*, *20*(21), 6770-6778. https://doi.org/10.1021/cm801807b

[17] Chowdhury, P., Gomaa, H., & Ray, A. K. (2015). Sacrificial hydrogen generation from aqueous triethanolamine with Eosin Y-sensitized Pt/TiO2 photocatalyst in UV, visible and solar light irradiation. *Chemosphere*, *121*, 54-61.https://doi.org/10.1016/j.chemosphere.2014.10.076

[18] Li, R., & Li, C. (2017). Chapter One - Photocatalytic Water Splitting on Semiconductor-Based Photocatalysts. In C. Song (Ed.), *Advances in Catalysis* (Vol. 60, pp. 1-57). Academic Press. https://doi.org/https://doi.org/10.1016/bs.acat.2017.09.001

[19] Hari, D. P., & König, B. (2014). Synthetic applications of eosin Y in photoredox catalysis. *Chemical Communications*, *50*(51), 6688-6699. https://doi.org/10.1039/C4CC00751D

[20] Bai, S., Yin, W., Wang, L., Li, Z., & Xiong, Y. (2016). Surface and interface design in cocatalysts for photocatalytic water splitting and CO2 reduction. *Rsc Advances*, *6*(62), 57446-57463. https://doi.org/10.1039/C6RA10539D

[21] Danish, M. S. S. (2023). Exploring metal oxides for the hydrogen evolution reaction (HER) in the field of nanotechnology. *RSC Sustainability*, *1*(9), 2180-2196. https://doi.org/10.1039/D3SU00179B

[22] Concina, I., Ibupoto, Z. H., & Vomiero, A. (2017). Semiconducting Metal Oxide Nanostructures for Water Splitting and Photovoltaics. *Advanced Energy Materials*, *7*(23), 1700706.https://doi.org/10.1002/aenm.201700706

[23] Aslan, E., Sarilmaz, A., Yanalak, G., Chang, C. S., Cinar, I., Ozel, F., & Patir, I. H. (2020). Facile preparation of amorphous NiWSex and CoWSex nanoparticles for the electrocatalytic hydrogen evolution reaction in alkaline condition. *Journal of Electroanalytical Chemistry*, *856*,

113674.https://doi.org/10.1016/j.jelechem.2019.113674

[24] Yang, J., & Shin, H. S. (2014). Recent advances in layered transition metal dichalcogenides for hydrogen evolution reaction. *Journal of Materials Chemistry A*, *2*(17), 5979-5985. https://doi.org/10.1039/C3TA14151A

[25] Gupta, U., & Rao, C. N. R. (2017). Hydrogen generation by water splitting using MoS2 and other transition metal dichalcogenides. *Nano Energy*, *41*, 49-65.https://doi.org/10.1016/j.nanoen.2017.08.021

[26] Fadojutimi, P. O., Gqoba, S. S., Tetana, Z. N., & Moma, J. (2022). Transition Metal Dichalcogenides [MX2] in Photocatalytic Water Splitting. *Catalysts*, *12*(5). https://doi.org/10.3390/catal12050468

[27] Zhao, H., Jian, L., Gong, M., Jing, M., Li, H., Mao, Q., Lu, T., Guo, Y., Ji, R., Chi, W., Dong, Y., & Zhu, Y. (2022). Transition-Metal-Based Cocatalysts for Photocatalytic Water Splitting. *Small Structures*, *3*(7), 2100229.https://doi.org/10.1002/sstr.202100229

[28] Wang, Y., Sun, L., Lv, H., Zheng, C., & Liu, B. (2022). Ordered Mesoporous Intermetallic PtP2 Nanoparticles with Enhanced Electrocatalytic Activity and Stability for Hydrogen Evolution. *CCS Chemistry*, *5*(8), 1896-1907. https://doi.org/10.31635/ccschem.022.202202451

[29] Akhoondi, A., Sharma, A., Pathak, D., Yusuf, M., Demissie, T. B., Guo, R.-t., & Ali, A. (2021). Hydrogen evolution via noble metals based photocatalysts: A review. *Synthesis and Sintering*, *1*(4), 223-241. https://doi.org/10.53063/synsint.2021.1468

[30] Yang, X., Guo, R., Cai, R., Shi, W., Liu, W., Guo, J., & Xiao, J. (2022). Engineering transition metal catalysts for large-current-density water splitting. *Dalton Transactions*, *51*(12), https://doi.org/10.1039/D2DT00037G

[31] Liu, S., Kuang, W., Meng, X., Qi, W., Adimi, S., Guo, H., Guo, X., Pervaiz, E., Zhu, Y., Xue, D., & Yang, M. (2021). Dual-phase metal nitrides as highly efficient co-catalysts for photocatalytic hydrogen evolution. *Chemical Engineering Journal*, *416*, 129116.https://doi.org/10.1016/j.cej.2021.129116

[32] Zhao, W., Chen, Z., Yang, X., Qian, X., Liu, C., Zhou, D., Sun, T., Zhang, M., Wei, G., Dissanayake, P. D., & Ok, Y. S. (2020). Recent advances in photocatalytic hydrogen evolution with high-performance catalysts without precious metals. *Renewable and Sustainable Energy Reviews*, *132*, 110040.https://doi.org/10.1016/j.rser.2020.110040

[33] Tran, T. D., Nguyen, M. T. T., Le, H. V., Nguyen, D. N., Truong, Q. D., & Tran, P. D. (2018). Gold nanoparticles as an outstanding catalyst for the hydrogen evolution reaction. *Chemical Communications*, *54*(27), 3363-3366. https://doi.org/10.1039/C8CC00038G

[34] Mariandry, K., Kokate, R., Somerville, S. V., Gloag, L., Cheong, S., Carroll, L. R., Kumar, P. V., Gooding, J. J., & Tilley, R. D. (2023). Controlling Platinum Active Sites on Silver Nanoparticles for Hydrogen Evolution Reaction. *Chemistry of Materials*, *35*(20), 8636-8644. https://doi.org/10.1021/acs.chemmater.3c01765

[35] Wang, N., Wang, J., Hu, J., Lu, X., Sun, J., Shi, F., Liu, Z.-H., Lei, Z., & Jiang, R. (2018). Design of Palladium-Doped g-C3N4 for Enhanced Photocatalytic Activity toward Hydrogen Evolution Reaction. *ACS Applied Energy Materials*, *1*(6), 2866-2873. https://doi.org/10.1021/acsaem.8b00526

[36] Liu, Y., Sun, Z., & Hu, Y. H. (2021). Bimetallic cocatalysts for photocatalytic hydrogen production from water. *Chemical Engineering Journal*, *409*, 128250.https://doi.org/10.1016/j.cej.2020.128250

[37] Wu, J., Xi, X., Zhu, W., Yang, Z., An, P., Wang, Y., Li, Y., Zhu, Y., Yao, W., & Jiang, G. (2022). Boosting photocatalytic hydrogen evolution via regulating Pt chemical states. *Chemical Engineering Journal*, *442*, 136334.https://doi.org/10.1016/j.cej.2022.136334

[38] Jiang, B., Liu, S., Cheng, L., Zhou, L., Cui, H., Liu, M., Wen, M., Wang, C., Wang, W., Li, S., & Sun, X. (2024). Mass synthesis of Pt/C catalysts with high Pt loading for low-overpotential hydrogen evolution. *International Journal of Hydrogen Energy*, *58*, 268-278.https://doi.org/10.1016/j.ijhydene.2024.01.183

[39] Zou, X., & Zhang, Y. (2015). Noble metal-free hydrogen evolution catalysts

for water splitting. *Chemical Society Reviews*, *44*(15), 5148-5180. https://doi.org/10.1039/C4CS00448E

[40] Pu, Z., Amiinu, I. S., Kou, Z., Li, W., & Mu, S. (2017). RuP2-Based Catalysts with Platinum-like Activity and Higher Durability for the Hydrogen Evolution Reaction at All pH Values. *Angewandte Chemie International Edition*, *56*(38), 11559-11564.https://doi.org/10.1002/anie.201704911

[41] Campelo, J. M., Luna, D., Luque, R., Marinas, J. M., & Romero, A. A. (2009). Sustainable Preparation of Supported Metal Nanoparticles and Their Applications in Catalysis. *ChemSusChem*, *2*(1), 18-45.https://doi.org/10.1002/cssc.200800227

[42] Dong, P., Wang, Y., Zhang, A., Cheng, T., Xi, X., & Zhang, J. (2021). REF1Platinum Single Atoms Anchored on a Covalent Organic Framework: Boosting Active Sites for Photocatalytic Hydrogen Evolution. *ACS Catalysis*, *11*(21), 13266-13279. https://doi.org/10.1021/acscatal.1c03441

[43] Fiorio, J. L., Gothe, M. L., Kohlrausch, E. C., Zardo, M. L., Tanaka, A. A., de Lima, R. B., da Silva, A. G. M., Garcia, M. A. S., Vidinha, P., & Machado, G. (2022). Nanoengineering of Catalysts for Enhanced Hydrogen Production. *Hydrogen*, *3*(2), 218-254, https://www.mdpi.com/2673-4141/3/2/14

[44] Zuo, Q., Liu, T., Chen, C., Ji, Y., Gong, X., Mai, Y., & Zhou, Y. (2019). Ultrathin Metal–Organic Framework Nanosheets with Ultrahigh Loading of Single Pt Atoms for Efficient Visible-Light-Driven Photocatalytic H2 Evolution. *Angewandte Chemie International Edition*, *58*(30), 10198-10203.https://doi.org/10.1002/anie.201904058

[45] Zheng, L.-L., Wang, D., Wu, S.-L., Jiang, X.-H., Zhang, J., Xing, Q.-J., Zou, J.-P., & Luo, S.-L. (2020). Unveiling localized Pt–P–N bonding states constructed on covalent triazine-based frameworks for boosting photocatalytic hydrogen evolution *Journal of Materials Chemistry A*, *8*(47), 25425-25430. https://doi.org/10.1039/D0TA10165F

[46] Xing, J., Li, Y. H., Jiang, H. B., Wang, Y., & Yang, H. G. (2014). The size and valence state effect of Pt on photocatalytic H2 evolution over platinized TiO2

photocatalyst. *International Journal of Hydrogen Energy*, *39*(3), 1237-1242.https://doi.org/10.1016/j.ijhydene.2013.11.041

[47] Zheng, L.-L., Li, X., Wang, D., Chen, Y., Fu, Q., Wu, D.-S., Liu, X.-Z., & Zou, J.-P. (2024). Selective anchoring of Pt NPs on covalent triazine-based frameworks via in situ derived bridging ligands for boosting photocatalytic hydrogen evolution. *Nanoscale*. https://doi.org/10.1039/D4NR00289J

[48] Xi, J., Zhang, X., Zhou, X., Wu, X., Wang, S., Yu, W., Yan, N., Loh, K. P., & Xu, Q.-H. (2022). Titanium dioxide hierarchical microspheres decorated with atomically dispersed platinum as an efficient photocatalyst for hydrogen evolution. *Journal of Colloid and Interface Science*, *623*, 799-807.https://doi.org/10.1016/j.jcis.2022.05.108

[49] Wang, X., Bai, L. C., Lu, J., Zhang, X., Liu, D. N., Yang, H. H., Wang, J. H., Chu, P. K., Ramakrishna, S., & Yu, X. F. (2019). Rapid Activation of Platinum with Black Phosphorus for Efficient Hydrogen Evolution. *Angewandte Chemie-International Edition*, *58*(52), 19060-19066. https://doi.org/10.1002/ange.201911696

[50] Xue, Y., Min, S., & Wang, F. (2019). Dye-sensitized black phosphorus nanosheets decorated with Pt cocatalyst for highly efficient photocatalytic hydrogen evolution under visible light. *International Journal of Hydrogen Energy*, *44*(39), 21873-21881.https://doi.org/10.1016/j.ijhydene.2019.06.087

[51] Zeng, Z., Su, Y., Quan, X., Choi, W., Zhang, G., Liu, N., Kim, B., Chen, S., Yu, H., & Zhang, S. (2020). Single-atom platinum confined by the interlayer nanospace of carbon nitride for efficient photocatalytic hydrogen evolution. *Nano Energy*, *69*, 104409.https://doi.org/10.1016/j.nanoen.2019.104409

[52] Lu, X., Tong, A., Luo, D., Jiang, F., Wei, J., Huang, Y., Jiang, Z., Lu, Z., & Ni, Y. (2022). Confining single Pt atoms from Pt clusters on multi-armed CdS for enhanced photocatalytic hydrogen evolution. *Journal of Materials Chemistry A*, *10*(9), 4594-4600. https://doi.org/10.1039/D2TA00198E

[53] Lian, Z., Wang, W., Li, G., Tian, F., Schanze, K. S., & Li, H. (2017). Pt-

Enhanced Mesoporous Ti3+/TiO2 with Rapid Bulk to Surface Electron Transfer for Photocatalytic Hydrogen Evolution. *ACS Applied Materials & Interfaces*, *9*(20), 16959-16966. https://doi.org/10.1021/acsami.6b11494

[54] Yu, X., An, X., Genç, A., Ibáñez, M., Arbiol, J., Zhang, Y., & Cabot, A. (2015). Cu2ZnSnS4–PtM (M = Co, Ni) Nanoheterostructures for Photocatalytic Hydrogen Evolution. *The Journal of Physical Chemistry C*, *119*(38), 21882-21888. https://doi.org/10.1021/acs.jpcc.5b06199

[55] Wang, C., Dragoe, D., Colbeau-Justin, C., Haghi-Ashtiani, P., Ghazzal, M. N., & Remita, H. (2023). Highly Dispersed Ni–Pt Bimetallic Cocatalyst: The Synergetic Effect Yields Pt-Like Activity in Photocatalytic Hydrogen Evolution. *ACS Applied Materials & Interfaces*, *15*(36), 42637-42647. https://doi.org/10.1021/acsami.3c08842

[56] Van Dao, D., Nguyen, T. T. D., Le, T. D., Kim, S.-H., Yang, J.-K., Lee, I.-H., & Yu, Y.-T. (2020). Plasmonically driven photocatalytic hydrogen evolution activity of a Pt-functionalized Au@CeO2 core–shell catalyst under visible light. *Journal of Materials Chemistry A*, *8*(16), 7687-7694. https://doi.org/10.1039/D0TA00811G

[57] Gao, M., Tian, F., Guo, Z., Zhang, X., Li, Z., Zhou, J., Zhou, X., Yu, Y., & Yang, W. (2022). Mutual-modification effect in adjacent Pt nanoparticles and single atoms with sub-nanometer inter-site distances to boost photocatalytic hydrogen evolution. *Chemical Engineering Journal*, *446*, 137127.https://doi.org/10.1016/j.cej.2022.137127

[58] Yang, F., Zhang, Q., Zhang, J., Zhang, L., Cao, M., & Dai, W.-L. (2020). Embedding Pt nanoparticles at the interface of CdS/NaNbO3 nanorods heterojunction with bridge design for superior Z-Scheme photocatalytic hydrogen evolution. *Applied Catalysis B: Environmental*, *278*, 119290.https://doi.org/10.1016/j.apcatb.2020.119290

[59] Elbanna, O., Zhu, M., Fujitsuka, M., & Majima, T. (2019). Black Phosphorus Sensitized TiO2 Mesocrystal Photocatalyst for Hydrogen Evolution with Visible and Near-Infrared Light Irradiation. *ACS Catalysis*, *9*(4), 3618-3626.

https://doi.org/10.1021/acscatal.8b05081

[60] Feng, R., Wan, K., Sui, X., Zhao, N., Li, H., Lei, W., Yu, J., Liu, X., Shi, X., Zhai, M., Liu, G., Wang, H., Zheng, L., & Liu, M. (2021). Anchoring single Pt atoms and black phosphorene dual co-catalysts on CdS nanospheres to boost visible-light photocatalytic H2 evolution. *Nano Today*, *37*, 101080.https://doi.org/10.1016/j.nantod.2021.101080

[61] Wu, J., Zheng, W., & Chen, Y. (2022). Definition of photocatalysis: Current understanding and perspectives. *Current Opinion in Green and Sustainable Chemistry*, *33*, 100580.https://doi.org/10.1016/j.cogsc.2021.100580

[62] Al-Samarraay, M., Al-Zuhairi, O., Alamoodi, A. H., Albahri, O. S., Deveci, M., Alobaidi, O. R., Albahri, A. S., & Kou, G. (2024). An integrated fuzzy multi-measurement decision-making model for selecting optimization techniques of semiconductor materials. *Expert Systems with Applications*, *237*, 121439.https://doi.org/10.1016/j.eswa.2023.121439

[63] Monfort, O., & Plesch, G. (2018). Bismuth vanadate-based semiconductor photocatalysts: a short critical review on the efficiency and the mechanism of photodegradation of organic pollutants. *Environmental Science and Pollution Research*, *25*(20), 19362-19379. https://doi.org/10.1007/s11356-018-2437-9

[64] Tang, L., & Zou, J. (2023). p-Type Two-Dimensional Semiconductors: From Materials Preparation to Electronic Applications. *Nano-Micro Letters*, *15*(1), 230,

[65] Wang, M., Qin, Z., Diao, Z., Li, R., Zhong, J., Ma, D., & Chen, Y. (2020). Red Phosphorus/Carbon Nitride van der Waals Heterostructure for Photocatalytic Pure Water Splitting under Wide-Spectrum Light Irradiation. *ACS Sustainable Chemistry & Engineering*, *8*(35), 13459-13466. https://doi.org/10.1021/acssuschemeng.0c04372

[66] Wang, H., Zhang, L., Chen, Z., Hu, J., Li, S., Wang, Z., Liu, J., & Wang, X. (2014). Semiconductor heterojunction photocatalysts: design, construction, and photocatalytic performances. *Chemical Society Reviews*, *43*(15), 5234-5244. https://doi.org/10.1039/C4CS00126E

[67] Wang, Z., Lin, Z., Shen, S., Zhong, W., & Cao, S. (2021). Advances in designing heterojunction photocatalytic materials. *Chinese Journal of Catalysis*, *42*(5), 710-730.https://doi.org/10.1016/S1872-2067(20)63698-1

[68] Balapure, A., Ray Dutta, J., & Ganesan, R. (2024). Recent advances in semiconductor heterojunctions: a detailed review of the fundamentals of photocatalysis, charge transfer mechanism and materials. *RSC Applied Interfaces*, *1*(1), 43-69. https://doi.org/10.1039/D3LF00126A

[69] Li, J., Yang, X., Ma, C., Lei, Y., Cheng, Z., & Rui, Z. (2021). Selectively recombining the photoinduced charges in bandgap-broken Ag3PO4/GdCrO3 with a plasmonic Ag bridge for efficient photothermocatalytic VOCs degradation and CO2 reduction. *Applied Catalysis B: Environmental*, *291*, 120053.https://doi.org/10.1016/j.apcatb.2021.120053

[70] Davis, B. E., & Strandwitz, N. C. (2024). Dependence of the Metal–Insulator–Semiconductor Schottky Barrier Height on Insulator Composition. *ACS Applied Electronic Materials*, *6*(2), 770-776. https://doi.org/10.1021/acsaelm.3c01231

[71] Kumaravel, V., Mathew, S., Bartlett, J., & Pillai, S. C. (2019). Photocatalytic hydrogen production using metal doped TiO2: A review of recent advances. *Applied Catalysis B: Environmental*, *244*, 1021-1064.https://doi.org/10.1016/j.apcatb.2018.11.080

[72] Hu, Z., Shen, Z., & Yu, J. C. (2017). Phosphorus containing materials for photocatalytic hydrogen evolution. *Green Chemistry*, *19*(3), 588-613. https://doi.org/10.1039/C6GC02825J

[73] Chen, L., Ren, J.-T., & Yuan, Z.-Y. (2022). Design strategies of phosphorus-containing catalysts for photocatalytic, photoelectrochemical and electrocatalytic water splitting. *Green Chemistry*, *24*(2), 713-747. https://doi.org/10.1039/D1GC03768D

[74] Shen, Z.-K., Yuan, Y.-J., Pei, L., Yu, Z.-T., & Zou, Z. (2020). Black phosphorus photocatalysts for photocatalytic H2 generation: A review. *Chemical Engineering Journal*, *386*, 123997.https://doi.org/10.1016/j.cej.2019.123997

[75] Yi, Y., Yu, X.-F., Zhou, W., Wang, J., & Chu, P. K. (2017). Two-dimensional black phosphorus: Synthesis, modification, properties, and applications. *Materials Science and Engineering: R: Reports*, *120*, 1-33.https://doi.org/10.1016/j.mser.2017.08.001

[76] Liu, H., Du, Y., Deng, Y., & Ye, P. D. (2015). Semiconducting black phosphorus: synthesis, transport properties and electronic applications. *Chemical Society Reviews*, *44*(9), 2732-2743. https://doi.org/10.1039/C4CS00257A

[77] Lange, S., Schmidt, P., & Nilges, T. (2007). Au3SnP7@Black Phosphorus: An Easy Access to Black Phosphorus. *Inorganic Chemistry*, *46*(10), 4028-4035. https://doi.org/10.1021/ic062192q

[78] Wang, F., Ng, W. K. H., Yu, J. C., Zhu, H., Li, C., Zhang, L., Liu, Z., & Li, Q. (2012). Red phosphorus: An elemental photocatalyst for hydrogen formation from water. *Applied Catalysis B: Environmental*, *111-112*, 409-414.https://doi.org/10.1016/j.apcatb.2011.10.028

[79] Fung, C.-M., Er, C.-C., Tan, L.-L., Mohamed, A. R., & Chai, S.-P. (2022). Red Phosphorus: An Up-and-Coming Photocatalyst on the Horizon for Sustainable Energy Development and Environmental Remediation. *Chemical Reviews*, *122*(3), 3879-3965. https://doi.org/10.1021/acs.chemrev.1c00068

[80] Singh, S., & Kansal, S. K. (2022). Recent progress in red phosphorus-based photocatalysts for photocatalytic water remediation and hydrogen production. *Applied Materials Today*, *26*, 101345.https://doi.org/10.1016/j.apmt.2021.101345

[81] Ding, K., Wen, L., Huang, S., Li, Y., Zhang, Y., & Lu, Y. (2016). Electronic properties of red and black phosphorous and their potential application as photocatalysts. *Rsc Advances*, *6*(84), 80872-80884. https://doi.org/10.1039/C6RA10907A

[82] Jing, L., Zhu, R., Ng, Y. H., Hu, Z., Teoh, W. Y., Phillips, D. L., & Yu, J. C. (2020). Visible-light photocatalysis and charge carrier dynamics of elemental crystalline red phosphorus. *The Journal of Chemical Physics*, *153*(2), 024707.

https://doi.org/10.1063/5.0013142

[83] Liu, E., Qi, L., Chen, J., Fan, J., & Hu, X. (2019). In situ fabrication of a 2D Ni2P/red phosphorus heterojunction for efficient photocatalytic H2 evolution. *Materials Research Bulletin*, *115*, 27-36.https://doi.org/10.1016/j.materresbull.2019.03.011

[84] Zhu, E., Ma, Y., Du, H., Qi, K., Ainiwa, M., & Su, Z. (2020). Three-dimensional bismuth oxide/red phosphorus heterojunction composite with enhanced photoreduction activity. *Applied Surface Science*, *528*, 146932.https://doi.org/10.1016/j.apsusc.2020.146932

[85] Yan, Y., Xia, S., Sun, H., Pang, Y., Yang, J., & Zheng, S. (2020). A promising 3D crystalline red P/reduced graphene oxide aerogel architecture anode for sodium-ion batteries. *Chemical Engineering Journal*, *393*, 124788.https://doi.org/10.1016/j.cej.2020.124788

[86] Yuan, Y.-P., Cao, S.-W., Liao, Y.-S., Yin, L.-S., & Xue, C. (2013). Red phosphor/g-C3N4 heterojunction with enhanced photocatalytic activities for solar fuels production. *Applied Catalysis B: Environmental*, *140-141*, 164-168.https://doi.org/10.1016/j.apcatb.2013.04.006

[87] Huang, G., Ye, W., Lv, C., Butenko, D. S., Yang, C., Zhang, G., Lu, P., Xu, Y., Zhang, S., Wang, H., Zhu, Y., & Yang, D. (2022). Hierarchical red phosphorus incorporated TiO2 hollow sphere heterojunctions toward superior photocatalytic hydrogen production. *Journal of Materials Science & Technology*, *108*, 18-25.https://doi.org/10.1016/j.jmst.2021.09.026

[88] Dou, R., Lin, H., Guo, M., Cao, J., Liu, C., & Chen, S. (2020). Fabrication of Ag/RP composite with excellent photocatalytic activity for degrading high concentration of methyl orange solution. *Materials Letters*, *268*, 127612.https://doi.org/10.1016/j.matlet.2020.127612

[89] Qi, L., Dong, K., Zeng, T., Liu, J., Fan, J., Hu, X., Jia, W., & Liu, E. (2018). Three-dimensional red phosphorus: A promising photocatalyst with excellent adsorption and reduction performance. *Catalysis Today*, *314*, 42-

51.https://doi.org/10.1016/j.cattod.2018.01.002

[90] Alemdar, S., Basak, A., & Metin, O. (2023). Exploring the Enhanced Catalytic Activity of Pt Nanoparticles Generated on the Red Phosphorus/Graphitic Carbon Nitride Binary Heterojunctions in the Photo-assisted Hydrolysis of Ammonia Borane. *ACS Applied Materials & Interfaces*, *15*(41), 48096-48109. https://doi.org/10.1021/acsami.3c08787

[91] Kalay, E., Küçükkeçeci, H., Kilic, H., & Metin, Ö. (2020). Black phosphorus as a metal-free, visible-light-active heterogeneous photoredox catalyst for the direct C–H arylation of heteroarenes. *Chemical Communications*, *56*(44), 5901-5904. https://doi.org/10.1039/D0CC01874K

[92] Wang, D., Yi, P., Wang, L., Zhang, L., Li, H., Lu, M., Xie, X., Huang, L., & Huang, W. (2019). Revisiting the Growth of Black Phosphorus in Sn-I Assisted Reactions. *Frontiers in Chemistry*, *7*. https://doi.org/10.3389/fchem.2019.00021

[93] Tian, B., Tian, B., Smith, B., Scott, M. C., Lei, Q., Hua, R., Tian, Y., & Liu, Y. (2018). Facile bottom-up synthesis of partially oxidized black phosphorus nanosheets as metal-free photocatalyst for hydrogen evolution. *Proceedings of the National Academy of Sciences*, *115*(17), 4345-4350. https://doi.org/10.1073/pnas.1800069115

[94] Wang, Y., He, M., Ma, S., Yang, C., Yu, M., Yin, G., & Zuo, P. (2020). Low-Temperature Solution Synthesis of Black Phosphorus from Red Phosphorus: Crystallization Mechanism and Lithium Ion Battery Applications. *The Journal of Physical Chemistry Letters*, *11*(7), 2708-2716. https://doi.org/10.1021/acs.jpclett.0c00746

[95] Sun, Z., Miao, H., Khurram, M., Zhang, Z., Zhu, Y., & Yan, Q. (2021). Bottom-up approach to quasi-monolayer black phosphorus advancing photocatalytic H2 evolution. *Chemical Engineering Journal*, *421*, 127841.https://doi.org/10.1016/j.cej.2020.127841

[96] Liu, F., Shi, R., Wang, Z., Weng, Y., Che, C.-M., & Chen, Y. (2019). Direct Z-Scheme Hetero-phase Junction of Black/Red Phosphorus for Photocatalytic

Water Splitting. *Angewandte Chemie International Edition*, *58*(34), 11791-11795.https://doi.org/10.1002/anie.201906416

[97] Zhu, S., Liang, Q., Xu, Y., Fu, H., & Xiao, X. (2020). Facile Solvothermal Synthesis of Black Phosphorus Nanosheets from Red Phosphorus for Efficient Photocatalytic Hydrogen Evolution. *European Journal of Inorganic Chemistry*, *2020*(9), 773-779.https://doi.org/10.1002/ejic.202000048

[98] Ozawa, A., Yamamoto, M., Tanabe, T., Hosokawa, S., & Yoshida, T. (2020). Black phosphorus synthesized by solvothermal reaction from red phosphorus and its catalytic activity for water splitting. *Journal of Materials Chemistry A*, *8*(15), 7368-7376. https://doi.org/10.1039/C9TA13441G

[99] Wang, X., Bai, L., Lu, J., Zhang, X., Liu, D., Yang, H., Wang, J., Chu, P. K., Ramakrishna, S., & Yu, X.-F. (2019). Rapid Activation of Platinum with Black Phosphorus for Efficient Hydrogen Evolution. *Angewandte Chemie International Edition*, *58*(52), 19060-19066.https://doi.org/10.1002/anie.201911696

[100] Che, M. (2013). Nobel Prize in chemistry 1912 to Sabatier: Organic chemistry or catalysis? *Catalysis Today*, *218-219*, 162-171.https://doi.org/10.1016/j.cattod.2013.07.006

[101] Adam, D. (2001). Chemistry Nobel 2001. *Nature*. https://doi.org/10.1038/news011011-17

[102] Reddy Kannapu, H. P., Mullen, C. A., Elkasabi, Y., & Boateng, A. A. (2015). Catalytic transfer hydrogenation for stabilization of bio-oil oxygenates: Reduction of p-cresol and furfural over bimetallic Ni–Cu catalysts using isopropanol. *Fuel Processing Technology*, *137*, 220-228.https://doi.org/10.1016/j.fuproc.2015.04.023

[103] Zhang, D., Ye, F., Xue, T., Guan, Y., & Wang, Y. M. (2014). Transfer hydrogenation of phenol on supported Pd catalysts using formic acid as an alternative hydrogen source. *Catalysis Today*, *234*, 133-138.https://doi.org/10.1016/j.cattod.2014.02.039

[104] Li, S., Li, G., Meng, W., & Du, H. (2016). A Frustrated Lewis Pair Catalyzed

Asymmetric Transfer Hydrogenation of Imines Using Ammonia Borane. *Journal of the American Chemical Society*, *138*(39), 12956-12962. https://doi.org/10.1021/jacs.6b07245

[105] Petkar, D. R., Kadu, B. S., & Chikate, R. C. (2014). Highly efficient and chemoselective transfer hydrogenation of nitroarenes at room temperature over magnetically separable Fe–Ni bimetallic nanoparticles. *Rsc Advances*, *4*(16), 8004-8010. https://doi.org/10.1039/C3RA45787G

[106] Wang, D., & Astruc, D. (2015). The Golden Age of Transfer Hydrogenation. *Chemical Reviews*, *115*(13), 6621-6686. https://doi.org/10.1021/acs.chemrev.5b00203

[107] Metin, Ö., Mendoza-Garcia, A., Dalmızrak, D., Gültekin, M. S., & Sun, S. (2016). FePd alloy nanoparticles assembled on reduced graphene oxide as a catalyst for selective transfer hydrogenation of nitroarenes to anilines using ammonia borane as a hydrogen source. *Catalysis Science & Technology*, *6*(15), 6137-6143. https://doi.org/10.1039/C6CY00118A

[108] Metin, Ö., Can, H., Şendil, K., & Gültekin, M. S. (2017). Monodisperse Ag/Pd core/shell nanoparticles assembled on reduced graphene oxide as highly efficient catalysts for the transfer hydrogenation of nitroarenes. *Journal of Colloid and Interface Science*, *498*, 378-386.https://doi.org/10.1016/j.jcis.2017.03.066

[109] Göksu, H., Ho, S. F., Metin, Ö., Korkmaz, K., Mendoza Garcia, A., Gültekin, M. S., & Sun, S. (2014). Tandem Dehydrogenation of Ammonia Borane and Hydrogenation of Nitro/Nitrile Compounds Catalyzed by Graphene-Supported NiPd Alloy Nanoparticles. *ACS Catalysis*, *4*(6), 1777-1782. https://doi.org/10.1021/cs500167k

[110] Can, H., Can, S., Ebiri, R., & Metin, Ö. (2022). A facile synthesis of monodisperse cobalt–ruthenium alloy nanoparticles as catalysts for the dehydrogenation of morpholine borane and the hydrogenation of various organic compounds. *New Journal of Chemistry*, *46*(25), 12120-12131. https://doi.org/10.1039/D2NJ01761J

[111] Dağalan, Z., Can, H., Daştan, A., Nişancı, B., & Metin, Ö. (2022). Highly efficient hydrogenation and dehydrogenation of N-Heteroarenes catalyzed by mesoporous graphitic carbon nitride supported CoPd alloy nanoparticles. *Tetrahedron*, *114*, 132766.https://doi.org/10.1016/j.tet.2022.132766

[112] Ganjehyan, K., Nişancı, B., Sevim, M., Daştan, A., & Metin, Ö. (2019). Monodisperse CuPt alloy nanoparticles assembled on reduced graphene oxide as catalysts in the transfer hydrogenation of various functional organic groups. *Applied Organometallic Chemistry*, *33*(5), e4863.https://doi.org/10.1002/aoc.4863

[113] Nişancı, B., Turgut, M., Sevim, M., & Metin, Ö. (2017). Three-Component Cascade Reaction in a Tube: In Situ Synthesis of Pd Nanoparticles Supported on mpg-C3N4, Dehydrogenation of Ammonia Borane and Hydrogenation of Nitroarenes. *ChemistrySelect*, *2*(22), 6344-6349.https://doi.org/10.1002/slct.201701188

[114] Liu, Z., Huang, Y., Xiao, Q., & Zhu, H. (2016). Selective reduction of nitroaromatics to azoxy compounds on supported Ag–Cu alloy nanoparticles through visible light irradiation. *Green Chemistry*, *18*(3), 817-825. https://doi.org/10.1039/C5GC01726B

[115] Guo, M., Zhang, M., Liu, R., Zhang, X., & Li, G. (2022). State-of-the-Art Advancements in Photocatalytic Hydrogenation: Reaction Mechanism and Recent Progress in Metal-Organic Framework (MOF)-Based Catalysts. *Advanced Science*, *9*(1), 2103361.https://doi.org/10.1002/advs.202103361

[116] Tsutsumi, K., Uchikawa, F., Sakai, K., & Tabata, K. (2016). Photoinduced Reduction of Nitroarenes Using a Transition-Metal-Loaded Silicon Semiconductor under Visible Light Irradiation. *ACS Catalysis*, *6*(7), 4394-4398. https://doi.org/10.1021/acscatal.6b00886

[117] Shiraishi, Y., Takeda, Y., Sugano, Y., Ichikawa, S., Tanaka, S., & Hirai, T. (2011). Highly efficient photocatalytic dehalogenation of organic halides on TiO2 loaded with bimetallic Pd–Pt alloy nanoparticles. *Chemical Communications*, *47*(27), 7863-7865. https://doi.org/10.1039/C1CC12087E

[118] Dai, Y., Li, C., Shen, Y., Lim, T., Xu, J., Li, Y., Niemantsverdriet, H., Besenbacher, F., Lock, N., & Su, R. (2018). Light-tuned selective photosynthesis of azo- and azoxy-aromatics using graphitic C3N4. *Nature Communications*, *9*(1), 60. https://doi.org/10.1038/s41467-017-02527-8

[119] Medford, A. J., Vojvodic, A., Hummelshøj, J. S., Voss, J., Abild-Pedersen, F., Studt, F., Bligaard, T., Nilsson, A., & Nørskov, J. K. (2015). From the Sabatier principle to a predictive theory of transition-metal heterogeneous catalysis. *Journal of Catalysis*, *328*, 36-42.https://doi.org/10.1016/j.jcat.2014.12.033

[120] Hammer, B., & Nørskov, J. K. (1995). Electronic factors determining the reactivity of metal surfaces. *Surface Science*, *343*(3), 211-220.https://doi.org/10.1016/0039-6028(96)80007-0

[121] Xin, H., Vojvodic, A., Voss, J., Nørskov, J. K., & Abild-Pedersen, F. (2014). Effects of d-band shape on the surface reactivity of transition-metal alloys. *Physical Review B*, *89*(11), 115114. https://doi.org/10.1103/PhysRevB.89.115114

[122] Jiao, S., Fu, X., & Huang, H. (2022). Descriptors for the Evaluation of Electrocatalytic Reactions: d-Band Theory and Beyond. *Advanced Functional Materials*, *32*(4), 2107651.https://doi.org/10.1002/adfm.202107651

[123] Lamture, J. B. (2018). *Aniline and its Analogs*. Notion Press.

[124] Kalmode, H. P., Ravikumar, O., Paymode, D. J., Bachert, J., Burns, J. M., Stringham, R. W., Aleshire, S. L., & Nelson, R. C. (2024). A Tandem Ring Closure and Nitrobenzene Reduction with Sulfide Provides an Improved Route to an Important Intermediate for the Anti-Tuberculosis Drug Candidate Sutezolid. *Organic Process Research & Development*. https://doi.org/10.1021/acs.oprd.4c00014

[125] Augustine, R. L. (1976). Organic functional group hydrogenation. *Catalysis Reviews Science and Engineering*, *13*(1), 285-316, https://doi.org/10.1080/00087647608069940

[126] Turáková, M., Salmi, T., Eränen, K., Wärnå, J., Murzin, D. Y., & Králik, M. (2015). Liquid phase hydrogenation of nitrobenzene. *Applied Catalysis A: General*, *499*, 66-76.https://doi.org/10.1016/j.apcata.2015.04.002

[127] Song, J., Huang, Z.-F., Pan, L., Li, K., Zhang, X., Wang, L., & Zou, J.-J. (2018). Review on selective hydrogenation of nitroarene by catalytic, photocatalytic and electrocatalytic reactions. *Applied Catalysis B: Environmental*, *227*, 386-408.https://doi.org/10.1016/j.apcatb.2018.01.052

[128] Wisniak, J., & Klein, M. (1984). Reduction of nitrobenzene to aniline. *Industrial & engineering chemistry product research and development*, *23*(1), 44-50,

[129] Höller, V., Wegricht, D., Yuranov, I., Kiwi-Minsker, L., & Renken, A. (2000). Three-Phase Nitrobenzene Hydrogenation over Supported Glass Fiber Catalysts: Reaction Kinetics Study. *Chemical Engineering & Technology*, *23*(3), 251-255.https://doi.org/10.1002/(SICI)1521-4125(200003)23:3

[130] Makaryan, J. A., & Savchenko, V. I. (1993). n-Arylhydroxylamines Transformation in the Presense of Heterogeneous Catalysts. In L. Guczi, F. Solymosi, & P. TÉTÉNyi (Eds.), *Studies in Surface Science and Catalysis* (Vol. 75, pp. 2439-2442). Elsevier. https://doi.org/https://doi.org/10.1016/S0167-2991(08)64319-0

[131] Wang, B., Deng, Z., & Li, Z. (2020). Efficient chemoselective hydrogenation of nitrobenzene to aniline, azoxybenzene and azobenzene over CQDs/ZnIn2S4 nanocomposites under visible light. *Journal of Catalysis*, *389*, 241-246.https://doi.org/10.1016/j.jcat.2020.05.041

[132] Nafiu, S. A., Aziz, M. A., & Shaikh, M. N. (2020). Shape-dependent reactivity and chemoselectivity of nanogold towards nitrophenol reduction in water. *Journal of Organometallic Chemistry*, *922*, 121361.https://doi.org/10.1016/j.jorganchem.2020.121361

[133] Doherty, S., Knight, J. G., Backhouse, T., Summers, R. J., Abood, E., Simpson, W., Paget, W., Bourne, R. A., Chamberlain, T. W., Stones, R., Lovelock, K. R. J.,

Seymour, J. M., Isaacs, M. A., Hardacre, C., Daly, H., & Rees, N. H. (2019). Highly Selective and Solvent-Dependent Reduction of Nitrobenzene to N-Phenylhydroxylamine, Azoxybenzene, and Aniline Catalyzed by Phosphino-Modified Polymer Immobilized Ionic Liquid-Stabilized AuNPs. *ACS Catalysis*, *9*(6), 4777-4791. https://doi.org/10.1021/acscatal.9b00347

[134] Hu, Z.-N., Liang, J., Ding, K., Ai, Y., Liang, Q., & Sun, H.-b. (2021). Insight into the selectivity of nano-catalytic nitroarenes reduction over other active groups by exploring hydrogen sources and metal components. *Applied Catalysis A: General*, *626*, 118339.https://doi.org/10.1016/j.apcata.2021.118339

[135] Corma, A., Serna, P., Concepción, P., & Calvino, J. J. (2008). Transforming Nonselective into Chemoselective Metal Catalysts for the Hydrogenation of Substituted Nitroaromatics. *Journal of the American Chemical Society*, *130*(27), 8748-8753. https://doi.org/10.1021/ja800959g

[136] Mahdavi, F., Bruton, T. C., & Li, Y. (1993). Photoinduced reduction of nitro compounds on semiconductor particles. *The Journal of Organic Chemistry*, *58*(3), 744-746. https://doi.org/10.1021/jo00055a033

[137] Zhou, B., Song, J., Zhou, H., Wu, L., Wu, T., Liu, Z., & Han, B. (2015). Light-driven integration of the reduction of nitrobenzene to aniline and the transformation of glycerol into valuable chemicals in water. *Rsc Advances*, *5*(46), 36347-36352. https://doi.org/10.1039/C5RA06354J

[138] Xu, F., Meng, K., Cao, S., Jiang, C., Chen, T., Xu, J., & Yu, J. (2022). Step-by-Step Mechanism Insights into the TiO2/Ce2S3 S-Scheme Photocatalyst for Enhanced Aniline Production with Water as a Proton Source. *ACS Catalysis*, *12*(1), 164-172. https://doi.org/10.1021/acscatal.1c04903

[139] Xu, Y., Chen, Y., & Fu, W.-F. (2018). In Situ Preparation of CoP@CdS and Its Catalytic Activity toward Controlling Nitro Reduction under Visible-Light Irradiation. *ACS Omega*, *3*(2), 1904-1911. https://doi.org/10.1021/acsomega.7b01592

[140] Bhar, S., & Ananthakrishnan, R. (2015). Utilization of Ru(ii)-complex

immobilized ZnO hybrid in presence of Pt(ii) co-catalyst for photocatalytic reduction of 4-nitrophenol under visible light. *Rsc Advances*, *5*(27), 20704-20711. https://doi.org/10.1039/C4RA13746A

[141] Fu, X., Qi, Z., Ren, W., Xu, M., & Yang, Y. (2023). Photocatalytic reduction of nitrobenzene to aniline over CdS nanorods: the impacts of reaction conditions and the hydrogenation mechanism. *Catalysis Science & Technology*, *13*(24), 7022-7035. https://doi.org/10.1039/D3CY01252B

[142] Yin, Z., Xiao, Y., Wan, X., Jiang, Y., Chen, G., Shi, Q., & Cao, S. (2021). High photocatalytic activity of Cu2O embedded in hierarchically hollow SiO2 for efficient chemoselective hydrogenation of nitroarenes. *Journal of Materials Science*, *56*(5), 3874-3886. https://doi.org/10.1007/s10853-020-05449-x

[143] Kumar, A., Kumar, P., Joshi, C., Manchanda, M., Boukherroub, R., & Jain, S. L. (2016). Nickel Decorated on Phosphorous-Doped Carbon Nitride as an Efficient Photocatalyst for Reduction of Nitrobenzenes. *Nanomaterials*, *6*(4). https://doi.org/10.3390/nano6040059

[144] Han, C., Du, L., Konarova, M., Qi, D.-C., Phillips, D. L., & Xu, J. (2020). Beyond Hydrogen Evolution: Solar-Driven, Water-Donating Transfer Hydrogenation over Platinum/Carbon Nitride. *ACS Catalysis*, *10*(16), 9227-9235. https://doi.org/10.1021/acscatal.0c01932

[145] Zhang, D., Ren, P., Liu, W., Li, Y., Salli, S., Han, F., Qiao, W., Liu, Y., Fan, Y., Cui, Y., Shen, Y., Richards, E., Wen, X., Rummeli, M. H., Li, Y., Besenbacher, F., Niemantsverdriet, H., Lim, T., & Su, R. (2022). Photocatalytic Abstraction of Hydrogen Atoms from Water Using Hydroxylated Graphitic Carbon Nitride for Hydrogenative Coupling Reactions. *Angewandte Chemie International Edition*, *61*(24), e202204256.https://doi.org/10.1002/anie.202204256

[146] Robinson, J. W., Frame, E. M. S., Frame, G. M., Eileen, M., & Skelly, F. (2005). Undergraduate instrumental analysis.

[147] Goldstein, J. I., Newbury, D. E., Michael, J. R., Ritchie, N. W., Scott, J. H. J.,

& Joy, D. C. (2017). *Scanning electron microscopy and X-ray microanalysis*. springer.

[148] Tang, C. Y., & Yang, Z. (2017). Chapter 8 - Transmission Electron Microscopy (TEM). In N. Hilal, A. F. Ismail, T. Matsuura, & D. Oatley-Radcliffe (Eds.), *Membrane Characterization* (pp. 145-159). Elsevier. https://doi.org/10.1016/B978-0-444-63776-5.00008-5

[149] Carter, C. B., & Williams, D. B. (2016). *Transmission electron microscopy: Diffraction, imaging, and spectrometry*. Springer.

[150] Chastain, J., & King Jr, R. C. (1992). Handbook of X-ray photoelectron spectroscopy. *Perkin-Elmer Corporation*, *40*, 221,

[151] Mazzotta, E., Rella, S., Turco, A., & Malitesta, C. (2015). XPS in development of chemical sensors. *Rsc Advances*, *5*(101), 83164-83186. https://doi.org/10.1039/C5RA14139G

[152] Morozzi, P., Ballarin, B., Arcozzi, S., Brattich, E., Lucarelli, F., Nava, S., Gómez-Cascales, P. J., Orza, J. A. G., & Tositti, L. (2021). Ultraviolet–Visible Diffuse Reflectance Spectroscopy (UV–Vis DRS), a rapid and non-destructive analytical tool for the identification of Saharan dust events in particulate matter filters. *Atmospheric Environment*, *252*, 118297.https://doi.org/10.1016/j.atmosenv.2021.118297

[153] Jubu, P. R., Obaseki, O. S., Nathan-Abutu, A., Yam, F. K., Yusof, Y., & Ochang, M. B. (2022). Dispensability of the conventional Tauc's plot for accurate bandgap determination from UV–vis optical diffuse reflectance data. *Results in Optics*, *9*, 100273.https://doi.org/10.1016/j.rio.2022.100273

[154] Tebyetekerwa, M., Zhang, J., Xu, Z., Truong, T. N., Yin, Z., Lu, Y., Ramakrishna, S., Macdonald, D., & Nguyen, H. T. (2020). Mechanisms and Applications of Steady-State Photoluminescence Spectroscopy in Two-Dimensional Transition-Metal Dichalcogenides. *ACS Nano*, *14*(11), 14579-14604. https://doi.org/10.1021/acsnano.0c08668

[155] Sahil, K., Prashant, B., Akanksha, M., Premjeet, S., & Devashish, R. (2011).

Gas chromatography-mass spectrometry: applications. *International Journal of Pharmaceutical and Biological Archives*, *2*(6), 1544-1560.

[156] Emwas, A.-H. M., Al-Talla, Z. A., Yang, Y., & Kharbatia, N. M. (2015). Gas Chromatography–Mass Spectrometry of Biofluids and Extracts. In J. T. Bjerrum (Ed.), *Metabonomics: Methods and Protocols* (pp. 91-112). Springer New York. https://doi.org/10.1007/978-1-4939-2377-9_8

[157] MUTLUTÜRK, Ö. G. E., & Sevi, Ö. ALETLİ ANALİZ LABORATUVARI. ISBN: 978-625-7897-97-6

[158] Sivula, K. (2021). Mott–Schottky Analysis of Photoelectrodes: Sanity Checks Are Needed. *ACS Energy Letters*, *6*(7), 2549-2551. https://doi.org/10.1021/acsenergylett.1c01245

[159] Gelderman, K., Lee, L., & Donne, S. W. (2007). Flat-Band Potential of a Semiconductor: Using the Mott–Schottky Equation. *Journal of Chemical Education*, *84*(4), 685. https://doi.org/10.1021/ed084p685

[160] Chen, Z., Zhu, Y., Lei, J., Liu, W., Xu, Y., & Feng, P. (2017). A stage-by-stage phase-induction and nucleation of black phosphorus from red phosphorus under low-pressure mineralization. *CrystEngComm*, *19*(47), 7207-7212. https://doi.org/10.1039/C7CE01492A

[161] Wang, Y., Sun, L., Lv, H., Zheng, C., & Liu, B. (2023). Ordered Mesoporous Intermetallic PtP_2 Nanoparticles with Enhanced Electrocatalytic Activity and Stability for Hydrogen Evolution. *CCS Chemistry*, *5*(8), 1896-1907. https://doi.org/10.1039/C7CE01492A

[162] Zhu, Y., Ren, J., Zhang, X., & Yang, D. (2020). Elemental red phosphorus-based materials for photocatalytic water purification and hydrogen production . *Nanoscale*, *12*(25), 13297-13310. https://doi.org/10.1039/D0NR01748E

[163] Tian, W., Wang, Y., Fu, W., Su, J., Zhang, H., & Wang, Y. (2020). PtP2 nanoparticles on N,P doped carbon through a self-conversion process to core–shell Pt/PtP2 as an efficient and robust ORR catalyst. *Journal of Materials Chemistry A*, *8*(39), 20463-20473. https://doi.org/10.1039/D0TA06566H

[164] Cheng, L., Qiu, S., Wang, J., Chen, W., Wang, J., Du, W., Song, L., & Hu, Y. (2022). A multifunctional nanocomposite based on Pt-modified black phosphorus nanosheets loading with l-arginine for synergistic gas-sonodynamic cancer therapy. *Colloids and Surfaces A: Physicochemical and Engineering Aspects*, *638*, 128284.https://doi.org/10.1016/j.colsurfa.2022.128284

[165] Sun, Z. X., Sun, K., Gao, M. L., Metin, Ö., & Jiang, H. L. (2022). Optimizing Pt Electronic States through Formation of a Schottky Junction on Non-reducible Metal–Organic Frameworks for Enhanced Photocatalysis. *Angewandte Chemie*, *134*(32), e202206108, https://doi.org/10.1002/ange.202206108

[166] Yu, J.-H., Singh, K. P., Kim, S.-J., Kang, T.-H., Lee, K.-S., Kim, H., Ringe, S., & Yu, J.-S. (2023). Active and stable PtP2-based electrocatalysts solve the phosphate poisoning issue of high temperature fuel cells. *Journal of Materials Chemistry A*, *11*(12), 6413-6427. https://doi.org/10.1039/D2TA09110K

[167] Sun, Z., Zhang, B., Khurram, M., & Yan, Q. (2022). Amorphous black phosphorus: wet-chemical synthesis and atomic disordering-dependent electrocatalytic performance. *2D Materials*, *9*(2), 025019. https://doi.org/10.1088/2053-1583/ac5b93

[168] Aksoy, M., Eken Korkut, S., & Metin, Ö. (2022). AuPt alloy nanoparticles supported on graphitic carbon nitride: In situ synthesis and superb catalytic performance in the light-assisted hydrolytic dehydrogenation of ammonia borane. *Applied Surface Science*, *602*, 154286.https://doi.org/10.1016/j.apsusc.2022.154286

[169] Yang, X., Liu, X., Cai, W., Wang, Z., Huang, R., Rao, Z., Zhang, C., & Fu, C. (2024). Enhanced Piezo-photocatalytic Performances of AgNbO3 Materials for Dye Decomposition Via Polarization Engineering. *ChemPhotoChem*, *8*(2), e202300142.https://doi.org/10.1002/cptc.202300142

[170] Liang, Z., Sun, B., Xu, X., Cui, H., & Tian, J. (2019). Metallic 1T-phase MoS2 quantum dots/g-C3N4 heterojunctions for enhanced photocatalytic hydrogen

evolution. *Nanoscale*, *11*(25), 12266-12274. https://doi.org/10.1039/C9NR02714A

[171] Wu, J., Wang, D., Wan, S., Liu, H., Wang, C., & Wang, X. (2020). An Efficient Cobalt Phosphide Electrocatalyst Derived from Cobalt Phosphonate Complex for All-pH Hydrogen Evolution Reaction and Overall Water Splitting in Alkaline Solution. *Small*, *16*(15), 1900550.https://doi.org/10.1002/smll.201900550

[172] Yin, M., Ma, S., Wu, C., & Fan, Y. (2015). A noble-metal-free photocatalytic hydrogen production system based on cobalt(iii) complex and eosin Y-sensitized TiO2. *Rsc Advances*, *5*(3), 1852-1858. https://doi.org/10.1039/C4RA10767E

[173] Liu, J., Zou, Y., Jin, B., Zhang, K., & Park, J. H. (2019). Hydrogen Peroxide Production from Solar Water Oxidation. *ACS Energy Letters*, *4*(12), 3018-3027. https://doi.org/10.1021/acsenergylett.9b02199

[174] Cheng, H., Cheng, J., Wang, L., & Xu, H. (2022). Reaction Pathways toward Sustainable Photosynthesis of Hydrogen Peroxide by Polymer Photocatalysts. *Chemistry of Materials*, *34*(10), 4259-4273. https://doi.org/10.1021/acs.chemmater.2c00936

[175] Sultan, S., Tiwari, J. N., Singh, A. N., Zhumagali, S., Ha, M., Myung, C. W., Thangavel, P., & Kim, K. S. (2019). Single Atoms and Clusters Based Nanomaterials for Hydrogen Evolution, Oxygen Evolution Reactions, and Full Water Splitting. *Advanced Energy Materials*, *9*(22), 1900624.https://doi.org/10.1002/aenm.201900624

[176] Liu, Y., Zhang, N., Liu, X., Chen, C., Fan, L.-Z., & Jiao, L. (2017). Red phosphorus nanoparticles embedded in porous N-doped carbon nanofibers as high-performance anode for sodium-ion batteries. *Energy Storage Materials*, *9*, 170-178.https://doi.org/10.1016/j.ensm.2017.07.012

[177] Xie, F., Wang, Q., Gan, M., & Ma, L. (2024). Self-assembled 3D hydrangea-like Fe2P–CoP–NDC as an efficient carrier material of Pt nanoparticles for the methanol oxidation reaction. *New Journal of Chemistry*, *48*(2), 646-653. https://doi.org/10.1039/D3NJ04696F

[178] Zhang, J., Liu, J., Meng, Z., Jana, S., Wang, L., & Zhu, B. (2023). Electron transfer dynamics in Schottky junction photocatalyst during electron donor-assisted hydrogen production. *Journal of Materials Science & Technology*, *159*, 1-9.https://doi.org/10.1016/j.jmst.2023.02.044

[179] Yang, X., Ren, L., Jiang, D., Yin, L., Li, Z., & Yuan, Y. (2024). Strong Interfacial Chemical Bonding in Regulating Electron Transfer and Stabilizing Catalytic Sites in a Metal-Semiconductor Schottky Junction for Enhanced Photocatalysis. *Small*, *20*(16), 2308408.https://doi.org/10.1002/smll.202308408

[180] Altan, O., Altintas, E., Alemdar, S., & Metin, Ö. (2022). The rational design of a graphitic carbon nitride-based dual S-scheme heterojunction with energy storage ability as a day/night photocatalyst for formic acid dehydrogenation. *Chemical Engineering Journal*, *441*, 136047.https://doi.org/10.1016/j.cej.2022.136047

[181] Chen, Z., Song, Y., Cai, J., Zheng, X., Han, D., Wu, Y., Zang, Y., Niu, S., Liu, Y., Zhu, J., Liu, X., & Wang, G. (2018). Tailoring the d-Band Centers Enables Co4N Nanosheets To Be Highly Active for Hydrogen Evolution Catalysis. *Angewandte Chemie International Edition*, *57*(18), 5076-5080.https://doi.org/10.1002/anie.201801834

[182] Shao, M., Liu, P., Zhang, J., & Adzic, R. (2007). Origin of Enhanced Activity in Palladium Alloy Electrocatalysts for Oxygen Reduction Reaction. *The Journal of Physical Chemistry B*, *111*(24), 6772-6775. https://doi.org/10.1021/jp0689971

[183] Sakamoto, H., Imai, J., Shiraishi, Y., Tanaka, S., Ichikawa, S., & Hirai, T. (2017). Photocatalytic Dehalogenation of Aromatic Halides on Ta2O5-Supported Pt–Pd Bimetallic Alloy Nanoparticles Activated by Visible Light. *ACS Catalysis*, *7*(8), 5194-5201. https://doi.org/10.1021/acscatal.7b01735

[184] Hu, Y., Li, B., Jiao, X., Zhang, C., Dai, X., & Song, J. (2018). Stable Cycling of Phosphorus Anode for Sodium-Ion Batteries through Chemical Bonding with Sulfurized Polyacrylonitrile. *Advanced Functional Materials*, *28*(23), 1801010.https://doi.org/10.1002/adfm.201801010

[185] Panjiara, D., & Pramanik, H. (2020). Electrooxidation study of glycerol on synthesized anode electrocatalysts Pd/C and Pd-Pt/C in a Y-shaped membraneless air-breathing microfluidic fuel cell for power generation. *Ionics*, *26*(5), 2435-2452. https://doi.org/10.1007/s11581-019-03385-8

[186] Wang, Y., Liu, Z., Li, Y., Liu, Y., Liang, X., Liu, F., & Lu, G. (2024). Trace PdO and Co-MOF derivative modified SnO2 nanofibers for rapid triethylamine detection with little humidity disturbance. *Sensors and Actuators B: Chemical*, *403*, 135239.https://doi.org/10.1016/j.snb.2023.135239

[187] Lu, S., Weng, B., Chen, A., Li, X., Huang, H., Sun, X., Feng, W., Lei, Y., Qian, Q., & Yang, M.-Q. (2021). Facet Engineering of Pd Nanocrystals for Enhancing Photocatalytic Hydrogenation: Modulation of the Schottky Barrier Height and Enrichment of Surface Reactants. *ACS Applied Materials & Interfaces*, *13*(11), 13044-13054. https://doi.org/10.1021/acsami.0c19260

[188] Xu, Y.-F., Yang, M.-Z., Chen, H.-Y., Liao, J.-F., Wang, X.-D., & Kuang, D.-B. (2018). Enhanced Solar-Driven Gaseous CO2 Conversion by CsPbBr3 Nanocrystal/Pd Nanosheet Schottky-Junction Photocatalyst. *ACS Applied Energy Materials*, *1*(9), 5083-5089. https://doi.org/10.1021/acsaem.8b01133

[189] Pietrowski, M. (2012). Recent developments in heterogeneous selective hydrogenation of halogenated nitroaromatic compounds to halogenated anilines. *Current Organic Synthesis*, *9*(4), 470-487, https://doi.org/10.2174/157017912802651456

[190] Sohn, C. H., Yin, S., Peng, I., Loo, J. A., & Beauchamp, J. L. (2015). Investigation of the mechanism of electron capture and electron transfer dissociation of peptides with a covalently attached free radical hydrogen atom scavenger. *International Journal of Mass Spectrometry*, *390*, 49-55.https://doi.org/10.1016/j.ijms.2015.07.007

[191] Urban, P. L., Goodall, D. M., Bergström, E. T., & Bruce, N. C. (2006). 1,4-Benzoquinone-based electrophoretic assay for glucose oxidase. *Analytical Biochemistry*, *359*(1), 35-39.https://doi.org/10.1016/j.ab.2006.08.004

[192] Zhao, W., Ding, T., Wang, Y., Wu, M., Jin, W., Tian, Y., & Li, X. (2019). Decorating Ag/AgCl on UiO-66-NH2: Synergy between Ag plasmons and heterostructure for the realization of efficient visible light photocatalysis. *Chinese Journal of Catalysis*, *40*(8), 1187-1197.https://doi.org/10.1016/S1872-2067(19)63377-2

[193] Zhang, S., Wang, Z., Yao, L., & Shi, L. (2022). Preparation of perylene diimide modified AgCl photocatalyst and its photocatalytic performance for degrading various organic pollutants under visible light. *Colloids and Surfaces A: Physicochemical and Engineering Aspects*, *652*, 129902.https://doi.org/10.1016/j.colsurfa.2022.129902

[194] Shimura, K., & Yoshida, H. (2011). Heterogeneous photocatalytic hydrogen production from water and biomass derivatives. *Energy & Environmental Science*, *4*(7), 2467-2481. https://doi.org/10.1039/C1EE01120K

[195] Zhu, Y., Ren, J., Huang, G., Dong, C.-L., Huang, Y.-C., Lu, P., Tang, H., Liu, Y., Shen, S., & Yang, D. (2024). Red Phosphorus Grafted High-Index (116) Faceted Anatase TiO2 for Z-Scheme Photocatalytic Pure Water Splitting. *Advanced Functional Materials*, *34*(9), 2311623.https://doi.org/10.1002/adfm.202311623

Appendix A

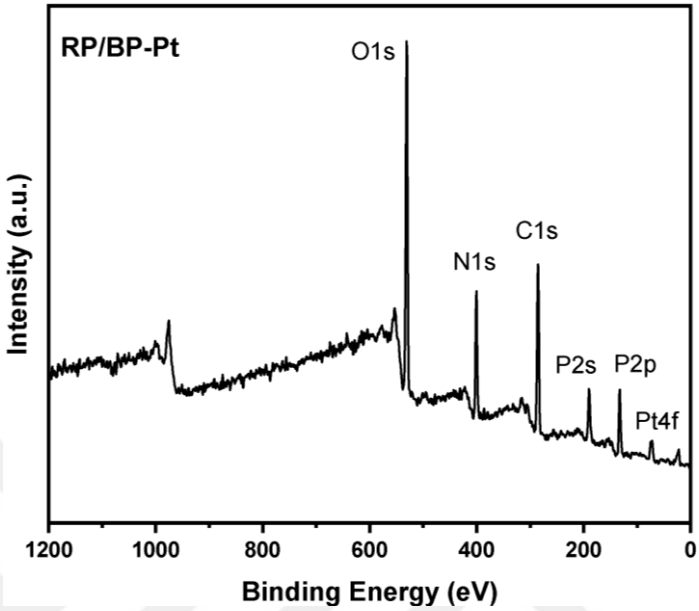

Figure A.1. XPS survey spectra of RP/BP-Pt

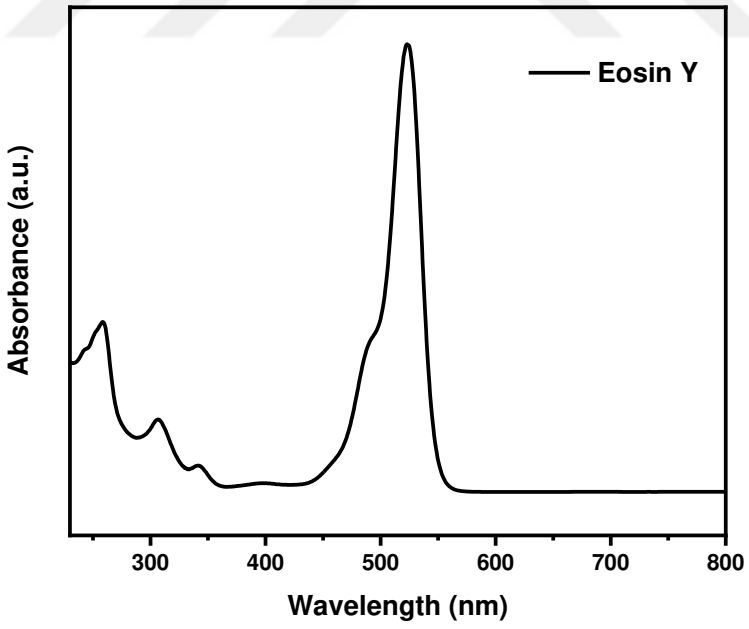

Figure A.2. Absorbance spectra of Eosin Y

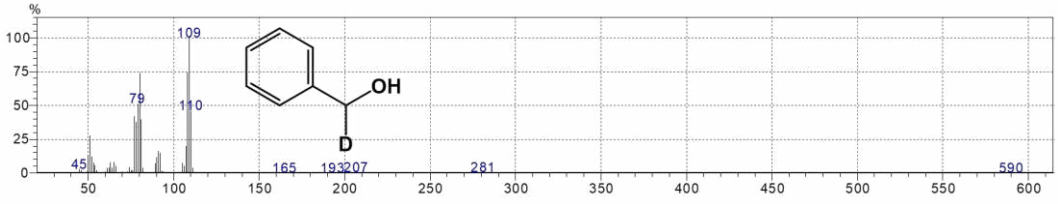

Figure A.3. GC-MS spectra of RP/BP-Pt catalyzed H_2-D_2 exchange experiment

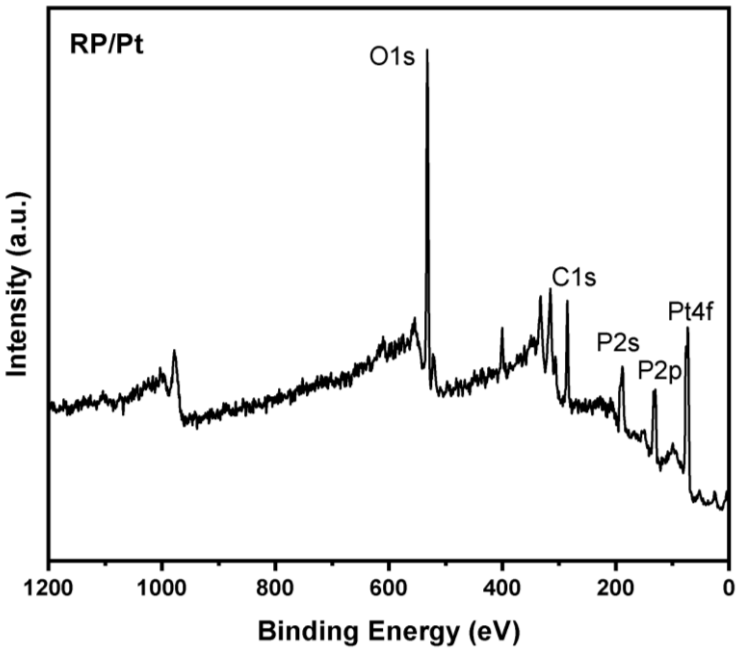

Figure A.4. HR-XPS survey spectra of RP/Pt

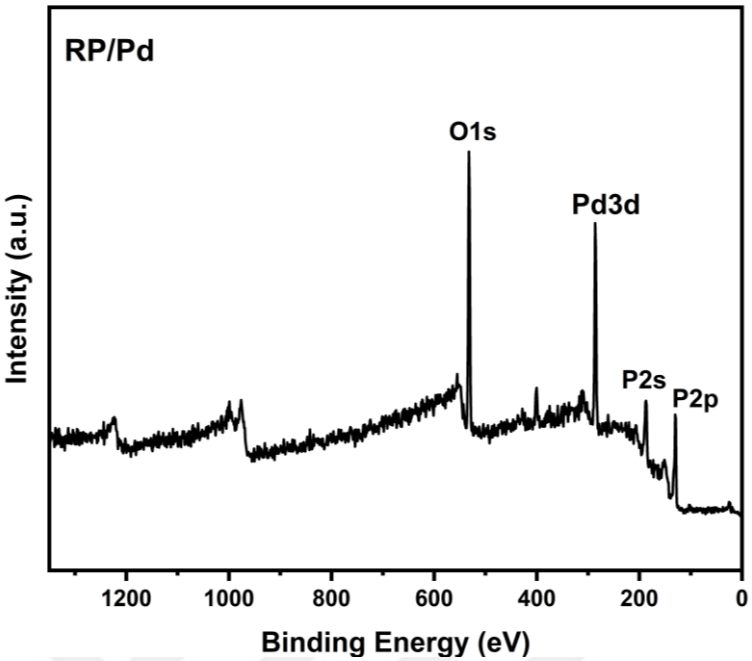

Figure A.5.HR-XPS survey spectra of RP/Pd

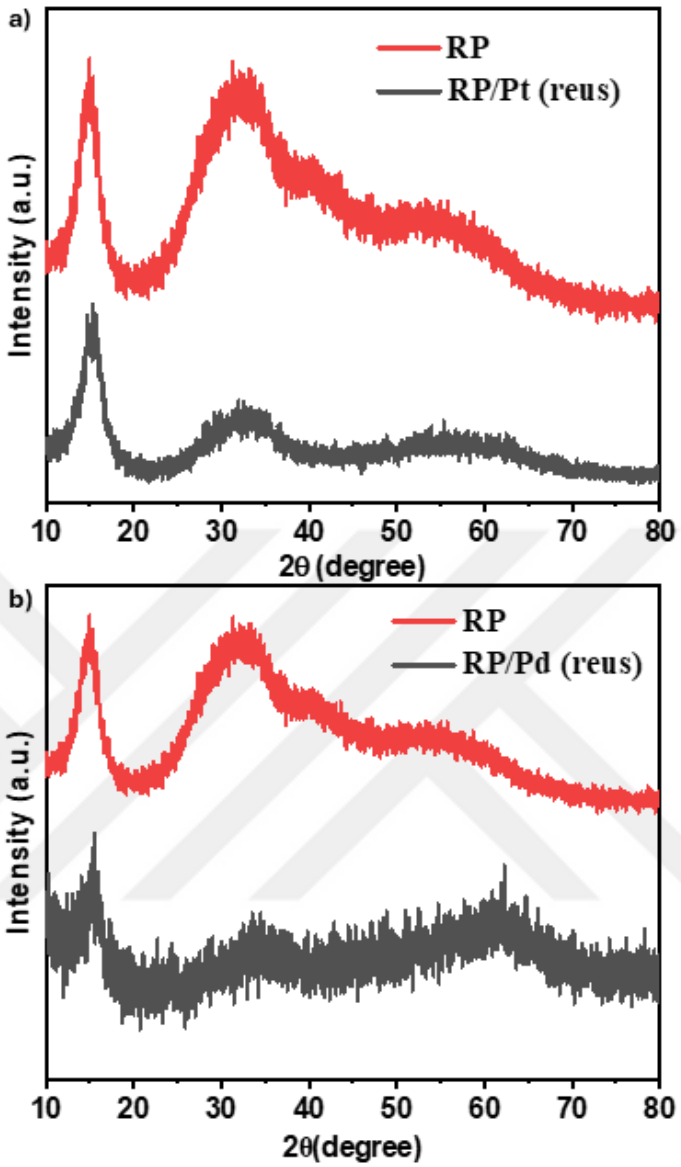

Figure A.6. XRD pattern of a)RP/Pt and b)RP/Pd after reusability test

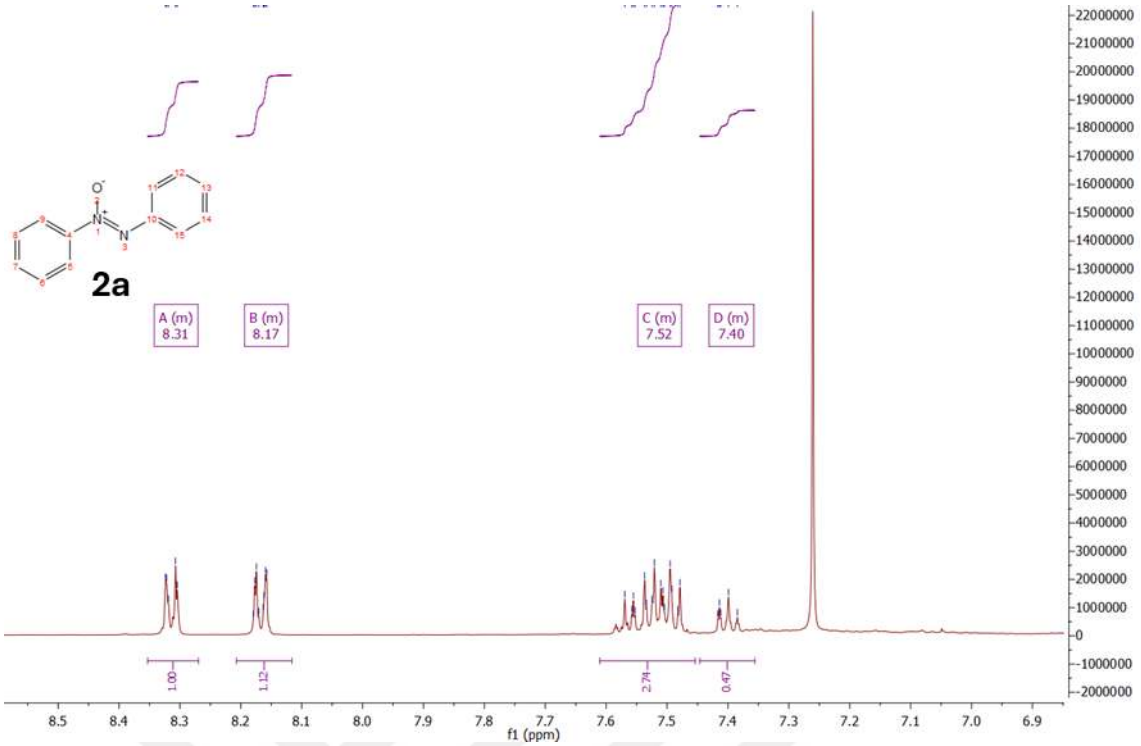

Figure A.7. ^{1}H- NMR spectra of 2a in $CDCl_3$

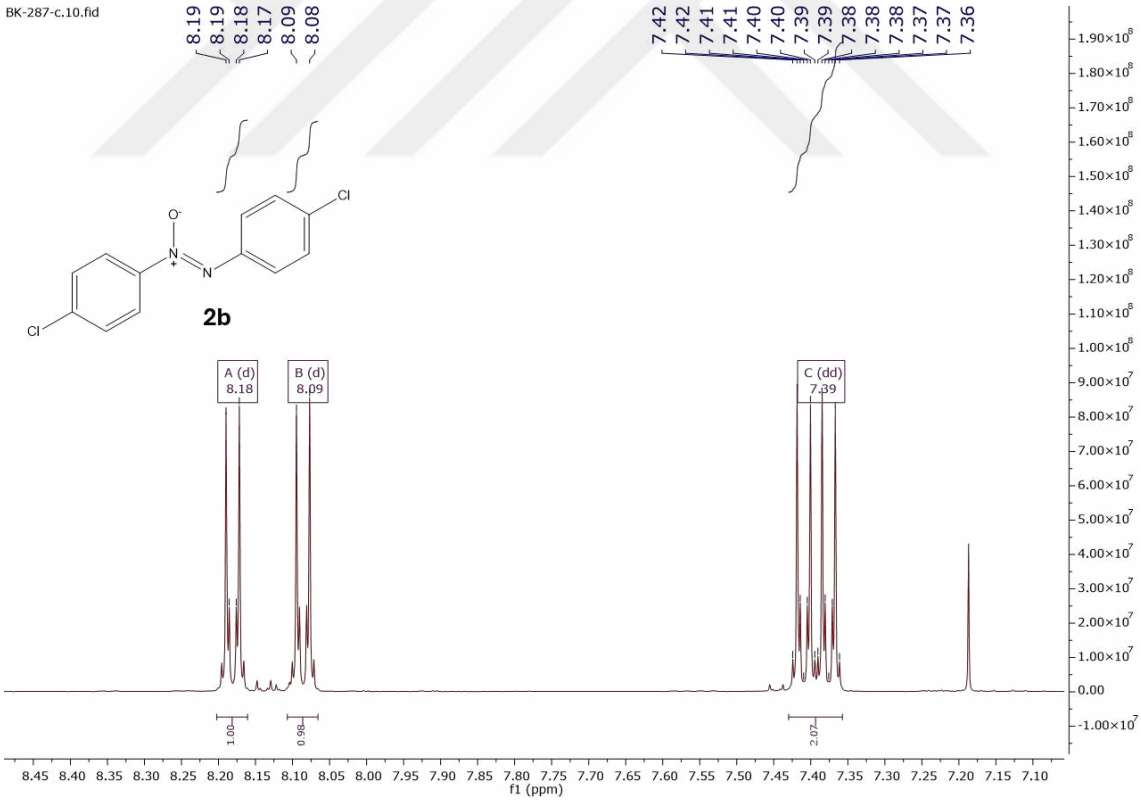

Figure A.8. ^{1}H- NMR spectra of 2b in $CDCl_3$

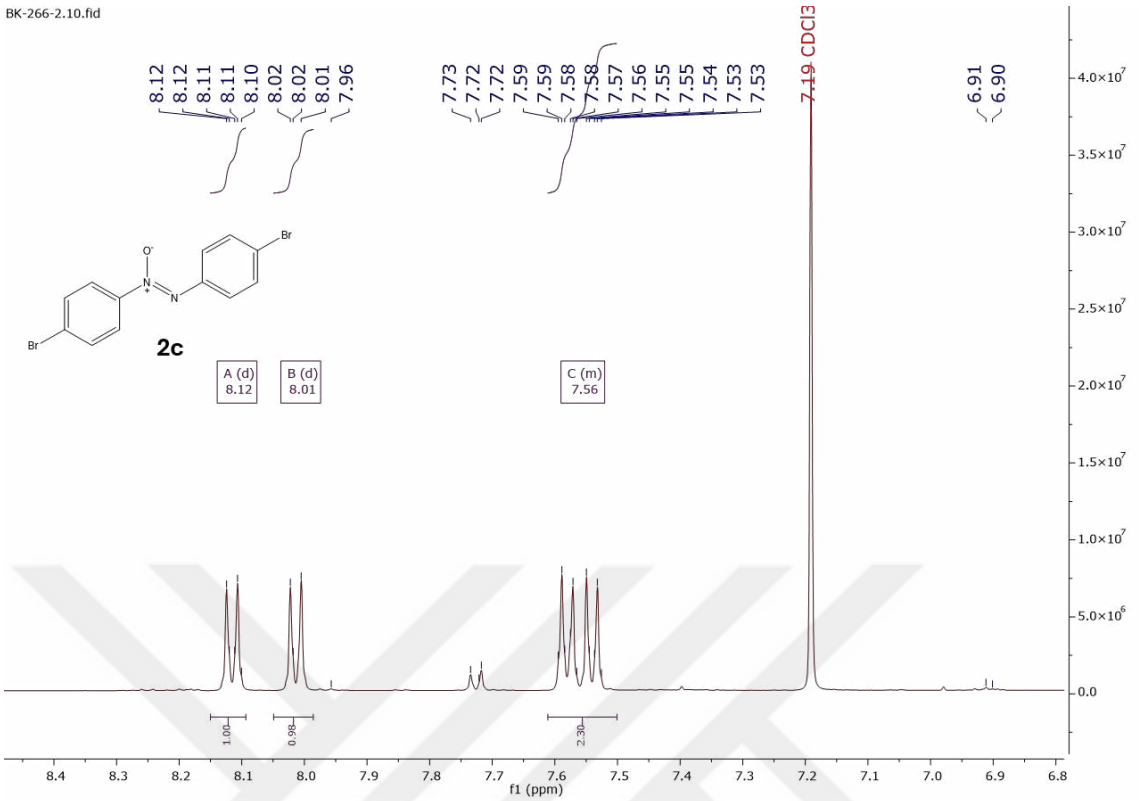

Figure A.9. ^{1}H- NMR spectra of 2c in $CDCl_3$

Figure A.10. ^{1}H- NMR spectra of 2d in $CDCl_3$

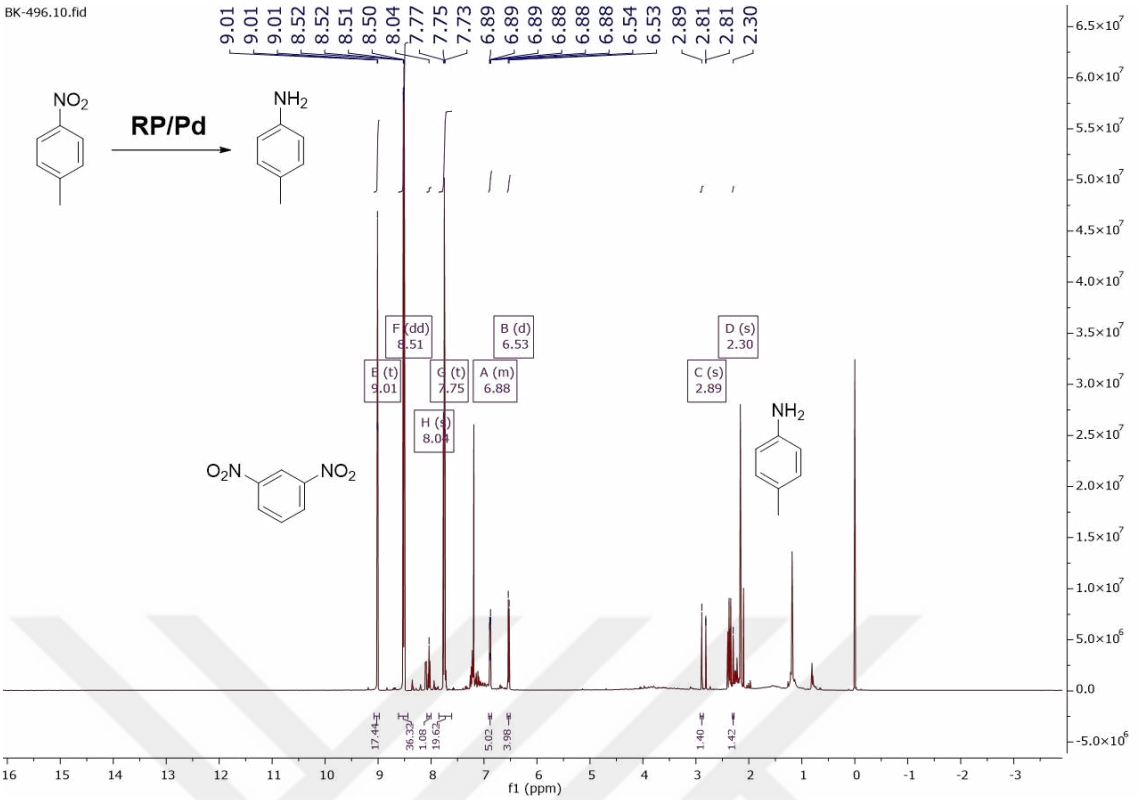

Figure A.11. A typical example of ^{1}H- NMR spectra of the mixture containing corresponding nitrobenzene, internal standard and aniline derivative

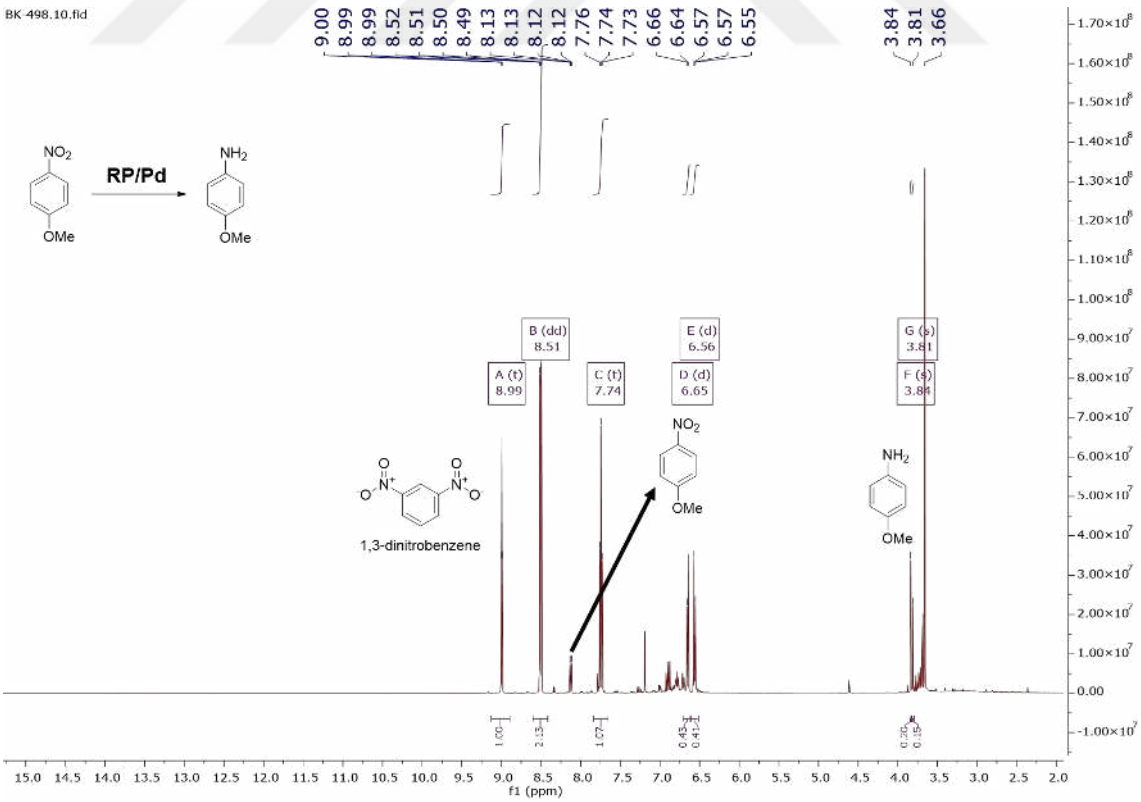

Figure A.12. A typical example of ^{1}H- NMR spectra of the mixture containing corresponding nitrobenzene, internal standard and aniline derivative

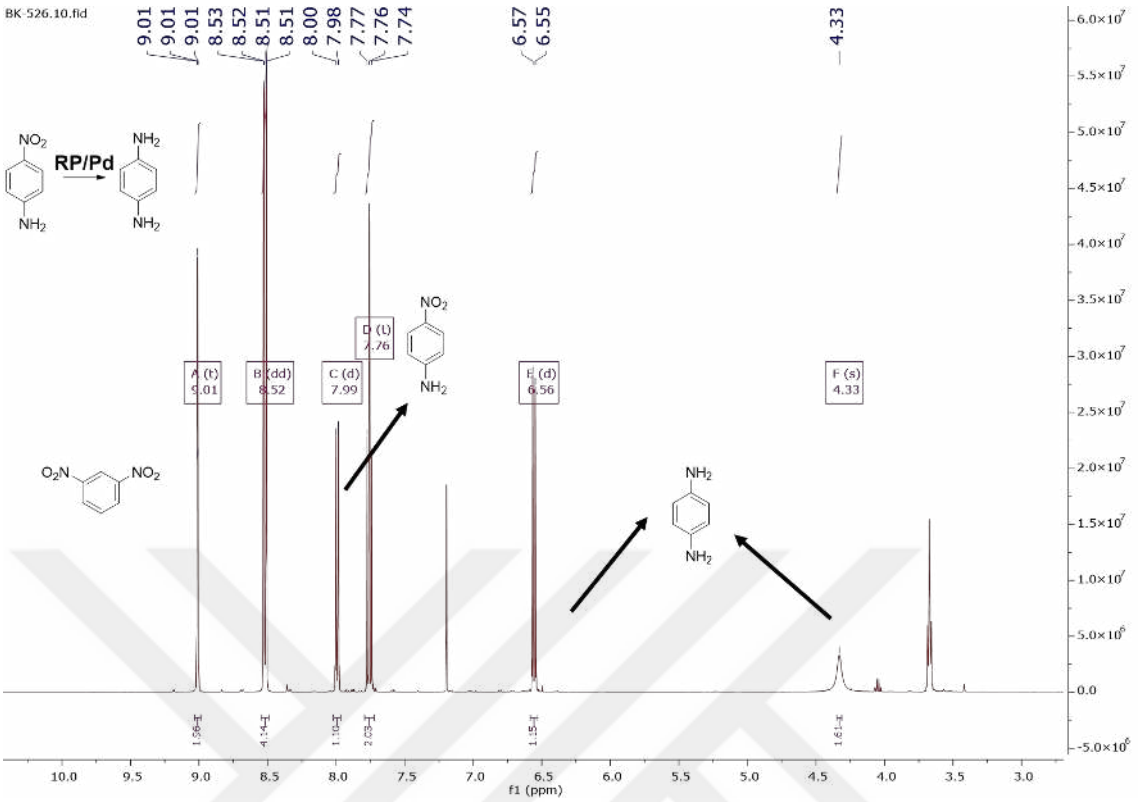

Figure A.13. A typical example of ^{1}H- NMR spectra of the mixture containing corresponding nitrobenzene, internal standard and aniline derivative